Selected applications of resonant phenomena in fourth-generation light sources

Dissertation zur Erlangung des Doktorgrades
an der Fakultät für Mathematik, Informatik und Naturwissenschaften
Fachbereich Physik
der Universität Hamburg

vorgelegt von
Edgar Cristopher Cortés García
geboren in Mexiko-Stadt, Mexiko

Hamburg
2025

Gutachter/innen der Dissertation:	Prof. Dr. Wolfgang Hillert Dr. Ilya Agapov
Zusammensetzung der Prüfungskommission:	Prof. Dr. Wolfgang Hillert Dr. Ilya Agapov Prof. Dr. Daniela Pfannkuche Dr. Felix Sefkow Prof. Dr. Markus Drescher
Vorsitzende/r der Prüfungskommission:	Prof. Dr. Daniela Pfannkuche
Datum der Disputation:	01.07.2025
Vorsitzender des Fach-Promotionsausschusses Physik:	Prof. Dr. Markus Drescher
Leiter des Fachbereichs Physik:	Prof. Dr. Wolfgang J. Parak
Dekan der Fakultät MIN:	Prof. Dr.-Ing. Norbert Ritter

Abstract

This thesis is focused on the design of the future fourth-generation light source PETRA IV and its booster ring. It investigates the utilization of linear and non-linear resonant phenomena to shape and control the electron beam—a subject that has traditionally played a secondary role in beam dynamics studies of electron storage rings, but becomes more important in the last generation of synchrotron light sources. The main research topic is to develop techniques to mitigate detrimental side effects of the unprecedented ultra-low emittances for storage rings expected at PETRA IV. At extremely low emittances, the electron beam exhibits significantly reduced transverse dimensions, leading to increased charge density, which translates into increased probability of Coulomb interactions between electrons inside the bunch. These ultimately lead to beam quality and lifetime degradation. A promising approach to mitigating these adverse effects is to shape the beam such that the transverse emittances are equalized. This thesis evaluates three mechanisms for the generation of transverse emittance control: vertical dispersion waves, AC dipole excitation and emittance sharing— thereby leveraging resonant phenomena to reshape the beam properties in the last two cases. Among these, the exploitation of the difference resonance ($q_x - q_y = 0$) to induce emittance sharing is identified as the most favorable approach, owing to its straightforward operational implementation and well-established theoretical foundation. The impact on beam dynamics performance with a beam with equal emittances is evaluated with numerical simulations. The key findings are: first, the Touschek limited beam lifetime increases by a factor of two. Second, intra-beam scattering-induced emittance deterioration is reduced, allowing the emittance to remain below 20 pm rad even for high single-bunch currents up to $I = 2.5$ mA.

Furthermore, PETRA IV features a sufficiently large dynamic aperture to support off-axis injection for both charge top-up and initial filling. Consequently, the injection efficiency under machine operation at the coupling resonance is assessed. Simulation results indicate that the strong amplitude dependence introduced by nonlinear effects in the electron dynamics enables an injection efficiency exceeding 99%. Experimental studies are conducted at the PETRA III electron storage ring at DESY and the Extremely Brilliant Source (EBS) at the European Synchrotron Radiation Facility (ESRF) in Grenoble, France. The experimental results reveal for both machines an injection efficiency below 20%, which deviates significantly from both simulation predictions (>99%) and a previously reported value in the literature (≈70%) at the Standford Positron Electron Accelerating Ring (SPEAR) in California, USA. This discrepancy underscores the necessity for dedicated optimization campaigns targeting nonlinear beam dynamics to achieve acceptable off-axis injection efficiency. Furthermore, it highlights the need for continuous refinement of existing models to accurately describe high-amplitude electron dynamics, particularly in the presence of strong nonlinear elements.

Additionally, an unexpected resonant phenomenon is encountered during the course of this thesis. Namely, the generation of quasi-stable transverse resonance islands is observed during PETRA IV simulation campaigns. Although these islands emerge when the machine is operated near the coupling resonance, no direct correlation with the vertical tune setting is found. Instead, dedicated simulations reveal that their formation is attributed to strong

amplitude detuning induced by nonlinear elements, which are introduced to mitigate the impact of nonlinear aberrations in the electron beam optics. More specifically, the amplitude detuning drives the horizontal tune to cross the third-order resonance for off-axis injected particles, making this resonance crossing the primary mechanism responsible for the formation of the islands. To validate and further characterize these quasi-stable resonance islands, dedicated experimental campaigns are conducted at the ESRF-EBS electron storage ring. The experimental results reveal a lifetime λ =6.74 s $\pm(0.23_{\text{stat.}} + 0.03_{\text{sys.}})$ s of trapped particles in the resonance islands. This study represents the first observed instance of a nonlinear resonant phenomenon being triggered while the machine's working point is found far from the nominally excited resonance. The full potential of these resonance islands remains an open question for future research, which will focus on further characterization and strategies to enhance electron capture lifetime.

Finally, a resonant slow extraction scheme that makes use of the generation of third order resonance islands is proposed. This novel variation of the resonant extraction can deliver extraction efficiencies in excess of 90% with electrostatic septa already available at other research facilities. The concept has been evaluated in the context of the future booster ring DESY IV and can potentially serve the high energy physics community that primarly exploits the beams offered at DESY in the test beam facility.

Zusammenfassung

In der vorliegenden Dissertation werden Untersuchungen zur zukünftigen vierten Generation der Synchrotron-Lichtquelle PETRA IV durchgeführt. Dabei werden lineare und nichtlineare Resonanzphänomene gezielt eingesetzt, um die Elektronenstrahlen zu formen. Dieser Ansatz spielt in den meisten Strahldynamikstudien zum Design von Elektronenspeicherringen bisher nur eine untergeordnete Rolle.

In PETRA IV werden extrem geringe Strahlemittanzen erzielt, wodurch die transversalen Strahlgrößen entsprechend klein ausfallen. Dadurch nimmt die Anzahl der Coulomb-Streuereignisse zu, was zu einer Verringerung der Strahllebensdauer und -qualität führt. Das Hauptthema dieser Dissertation konzentriert sich auf Mechanismen zur Minderung dieser Nebenwirkungen extrem geringer Strahlemittanzen.

Eine mögliche Strategie zur Reduzierung dieser Nebenwirkungen besteht im Ausgleich der transversalen Emittanzen. Dafür werden drei Methoden in Betracht gezogen, um die Emittanzen anzugleichen: der Einsatz vertikaler Dispersionswellen, die resonante Anregung vertikaler Betatron-Oszillationen und die Nutzung der Kopplungs- oder Differenzresonanz. Als bevorzugte Methode zur Erzeugung runder Strahlen (gleiche Emittanzen) gilt der Betrieb des Speicherrings bei der Kopplungsresonanz. Dabei werden die fraktionalen Arbeitspunkte des Speicherrings auf denselben Wert eingestellt.

Anhand von Simulationen werden zwei wesentliche Ergebnisse zur Strahldynamik festgestellt: erstens erhöht sich die durch Touschek-Streuung begrenzte Strahllebensdauer um einen Faktor zwei, wenn die Maschine mit runden Strahlen betrieben wird. Zweitens wird das durch Streuung zwischen den Strahlteilchen (Intra-Beam Scattering) verursachte Emittanz-Wachstum deutlich reduziert, sodass selbst bei hohen Einzelpaket-Elektronenströmen von $I = 2.5\,\mathrm{mA}$ die Emittanz weniger als 20 pm rad beträgt.

Ferner werden in PETRA IV die Anfangsladungsfüllung und die Nachfüllung durch Injektionen abseits der zentralen Achse realisiert. Daher stellt sich die Frage, ob der Betrieb der Maschine bei der Kopplungsresonanz die Injektionseffizienz negativ beeinflusst. Simulationen zeigen, dass die durch nichtlineare Komponenten hervorgerufene Amplitudenabhängigkeit der Strahldynamik eine hohe Injektionseffizienz (>99%) ermöglicht.

Experimente am PETRA-III-Speicherring bei DESY sowie an der extrem brillanten Quelle (EBS) an der Europäischen Synchrotronstrahlungs-Einrichtung (ESRF) in Grenoble, Frankreich wurden durchgeführt, um Injektionen abseits der zentralen Achse bei der Kopplungsresonanz zu untersuchen. Die gemessene Injektionseffizienz beträgt jedoch weniger als 20%. Dieses Ergebnis ist weder mit den Simulationen (>99%) noch mit in der Literatur angegebenen Werten (≈70%) vergleichbar. Die geringe Injektionseffizienz deutet darauf hin, dass die Implementierung der Methode mehr Zeit in Anspruch nehmen wird, um optimale Werte zu erzielen. Die Modelle zur Beschreibung der hochamplitudigen Strahldynamik müssen verfeinert und weiterentwickelt werden, insbesondere aufgrund dessen, dass stark nichtlineare Komponenten eine führende Rolle bei dieser Injektionsmethode spielen.

Ein weiteres, damit zusammenhängendes Thema dieser Dissertation ist die Untersuchung quasi-stabiler Resonanzinseln, welche durch Simulationen identifiziert wurden. Obwohl diese

Inseln beim Betrieb des Speicherrings auf der Kopplungsresonanz beobachtet werden, zeigt sich, dass ihre Erzeugung unabhängig vom vertikalen Arbeitspunkt ist. Stattdessen entstehen die Inseln durch nichtlineare Elemente der Strahloptik, die eine starke amplitudenabhängige Arbeitspunktverschiebung hervorrufen. Diese Verschiebung führt dazu, dass injizierte Elektronen, die sich abseits der zentralen Achse befinden, den horizontalen Arbeitspunkt in die Nähe der Resonanz dritter Ordnung bringen.

Experimente am ESRF-EBS-Elektronenspeicherring werden durchgeführt, um die Existenz der Inseln und deren Eigenschaften zu bestimmen. Die gemessene Lebensdauer gefangener Teilchen in den Inseln beträgt λ =6.74 s $\pm(0.23_{\text{stat.}} + 0.03_{\text{sys.}})$ s. Diese Ergebnisse stellen das erste Beispiel für ein Resonanzphänomen dar, das nicht durch das Annähern der nominalen Arbeitspunkte an die Resonanz hervorgerufen wird. Zukünftige Untersuchungen werden sich auf die weitere Charakterisierung und potenzielle Anwendungen dieser Resonanzinseln konzentrieren, insbesondere sollen Strategien zur Erweiterung der Lebensdauer erforscht werden.

Schließlich wurde eine Methode zur langsamen Resonanzextraktion für den Booster-Synchrotron DESY IV entwickelt, welche die Erzeugung von Resonanzinseln ausnutzt. Diese neuartige Methode kann eine Extraktionseffizienz von mindestens 90% mit bestehenden elektrostatischen Septa erreichen. Die Extraktionsmethode wurde als Konzept entwickelt und soll dazu dienen, Teststrahl-Nutzenden hochenergetische Elektronenstrahlen im Multi-GeV-Bereich bereitzustellen. Der potenzielle Einsatz von DESY IV zusätzlich zur Injektion eröffnet das Potenzial für zahlreiche Anwendungen in verschiedenen Bereichen, wodurch neue Möglichkeiten für wissenschaftliche Entdeckungen geschaffen werden können.

Contents

1

Introduction

Particle accelerators play a key role in generating a wide variety of particle beams, contributing immensely to scientific advancements across numerous disciplines. Among them, particle colliders have gathered particular attention, not only for their groundbreaking contributions to fundamental particle physics but also for their immense scale, high complexity and futuristic charm. Throughout the history of scientific exploration, some collider-based experiments have been repurposed once their primary objectives were achieved, ensuring the continued use of valuable infrastructure.

A notable example is the Hadron-Elektron-Ring-Anlage (HERA) electron-proton collider and its injector chain, which completed its operational goals in 2007. Rather than decommissioning the facility, efforts were made to maximize its potential. As a result, the Positron-Elektron-Tandem-Ring-Anlage (PETRA) booster ring at DESY's Bahrenfeld campus in Hamburg was transformed into PETRA III [1]—a state-of-the-art synchrotron light source dedicated to specialized applications.

The use of synchrotron light sources has fueled the discovery and investigation of numerous phenomena in a variety of scientific fields for many decades. The collective scientific output has been estimated at 183,000 unique articles published by 34 institutions over a period of 11 years [2]. One of many impactful examples is the work of Ada Yonath, who was awarded the 2009 Nobel Prize in Chemistry, along with V. Ramakrishnan and T. Steitz [3], for "studies of the structure and function of the ribosome." Yonath and her collaborators made essential contributions to the crystallization of the ribosome, a fundamental component in molecular biology. Advancements in increasingly sophisticated crystallization methods allowed ribosomal subunits to be resolved by X-ray imaging down to the 3 Å level at synchrotron radiation facilities.

Parallel to these discoveries, the technology of these machines has undergone certain transformations that were classified into four generations. After the emitted light by electron bunches in synchrotrons was observed in 1947 [4], it took circa 30 years until a dedicated machine was proposed to make optimal use of synchrotron light [5] and further 20 years until such a facility was conceived [6]. The first generation of synchrotron light sources offered photons to users from parasitic operations, usually getting the light beams produced at magnet dipoles from particle colliders. The second generation of light sources included dedicated insertion devices and offered supperior photon brightness and flux [7]. Dedicated machines built exclusively for the generation of light designed according to the principles outlined in [5] are classified as third-generation synchrotron light sources, many of which,

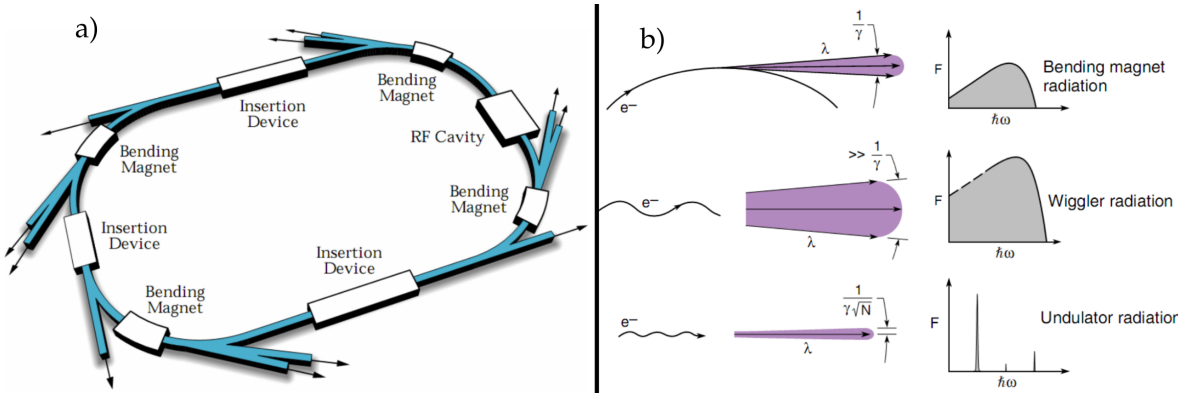

Figure 1.1: (a) The left panel displays a typical layout of an electron storage ring dedicated to the generation of synchrotron light. (b) The right panel illustrates the emission profile of different insertion devices, from top to bottom: bending magnets, wigglers, and undulators. Here F stands for the photon flux, γ for the relativistic gamma factor, λ for the wavelength of the radiation and N for the number of periods of the undulator. Both figures have been taken from [7].

including PETRA III, remain operational today. Unsurprisingly by the conception of the very first third-generation light source, crucial work had been laid out to drive the next generation leap [8]. At DESY, this means converting from PETRA III to PETRA IV as the fourth-generation transition approaches.

The work performed during this thesis pertains to the design of the electron storage ring and the booster synchrotron for the upgrade project PETRA IV. This thesis describes two main contributions to the design project: (1) the study of the implications and considerations of a round beam operation in the main storage ring and (2) the evaluation of a resonant slow extraction scheme from the booster ring. Before extending on the details, some concepts of the generation of light from synchrotrons is briefly introduced to provide motivation of the work.

1.1. Synchrotron light sources, photon brightness and diffraction limit

There are currently more than 50 light sources around the world, either operational or under construction [2]. Modern synchrotron light sources are composed of an injector complex and a main storage ring. The injector chain generates and accelerates bunches of electrons to relativistic energies, typically from 1 to 6 GeV. These are injected into the storage ring, where light is generated for multiple users. The electromagnetic radiation (i.e. light) is generated by introducing insertion devices in dedicated sections of the storage ring, which are known as undulators and wigglers. A typical storage ring layout for the dedicated generation and use of synchrotron light is shown in figure 1.1 on the left. Different emission profiles of commonly used insertion devices are depicted on the right.

Moreover, the development of fourth-generation light sources has been driven by the goal of enhancing synchrotron performance to enable the production of diffraction-limited radiation [9]. In order to explain the meaning of diffraction-limited radiation, a short detour into the concept of brightness is necessary. The peak brigthness $\mathcal{B}_o$ [10] is a broadly used figure of merit to quantify the amount of light that will be available for a certain experiment.

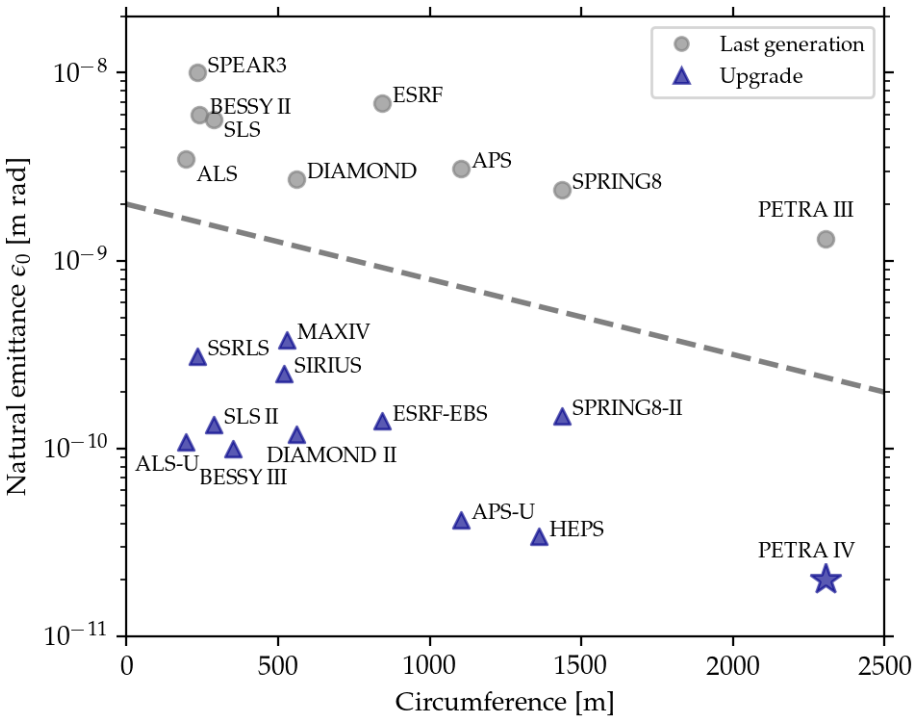

Figure 1.2: Natural emittance of various planned and running machines as a function of their ring circumference. PETRA IV is marked with a blue star on the bottom right corner. The grey dashed line highlights the difference between the upgraded and last generation machines.

Depending on the application, photon users are interested in a particular wavelength λ of the light produced. For example, the peak brightness $\mathcal{B}_o$ of the radiation emitted by an undulator is commonly estimated by [11]

$$\mathcal{B}_o = \frac{F}{4\pi^2 \Sigma_x \Sigma_{x'} \Sigma_y \Sigma_{y'}}, \tag{1.1}$$

where F is the spectral photon flux (photons per second per 0.1% bandwidth) and $\Sigma_{x,y}$, $\Sigma_{x',y'}$ represent the root-mean-squared (rms) beam sizes and divergences of the photon beam in the horizontal and vertical planes, respectively. The rms beam sizes and divergences are given by

$$\Sigma_{x,y} = \sqrt{(\sigma_{x,y}^2 + \sigma_R^2)} \tag{1.2}$$

$$\Sigma_{x',y'} = \sqrt{(\sigma_{x',y'}^2 + \sigma_{R'}^2)}. \tag{1.3}$$

In equations 1.2 and 1.3 $\sigma_{x,y}$, $\sigma_{x',y'}$ represent the rms beams sizes and divergences of the electron beam, respectively. Further, the intrinsic rms photon beam size and divergence are denoted by $\sigma_{R,R'}$. An essential parameter in this context is the beam emittance, which defines the phase-space area occupied by photons or stored electrons and is quantified in meters×radian. Under the Gaussian mode approximation the intrinsic emittance of the photon beam reads

$$\epsilon_R = \sigma_R \sigma_{R'} = \frac{\lambda}{4\pi}. \tag{1.4}$$

A similar relation exists between the electron beam emittance ϵ_0 and its rms size and divergence $\sigma_{x,x'}$. This will be introduced later in Chapter 2. In the meanwhile it is worth noting, that the result described by equation 1.4 commonly establishes the notion of the diffraction limit. Namely, the diffraction limit is reached, when the size and divergence of the light source, i.e. the electron bunch emittance, is much smaller than the wavelength of interest λ. Formally one speaks of a diffraction-limited source, if the electron beam emittance ϵ_0 fulfills [12]

$$\sigma_x \sigma_{x'} \propto \epsilon_0 \ll \frac{\lambda}{4\pi}. \tag{1.5}$$

To illustrate the situation of the current technology without diving into the technical details, the natural emittances of selected facilities are shown in figure 1.2. The natural emittance refers to the equilibrium electron beam emittance, thus is the relevant quantity to consider in equation 1.5. The grey dots above the dashed line illustrate the emittances achieved at third-generation light sources. The emittances achievable for fourth-generation light sources are depicted as blue triangles and are at least one order of magnitude lower. Around the world only five facilities have upgraded their storage ring to produce emittances below 1 nm rad: MAX-IV in Lund, Sweden [13], the European Synchrotron Radiation Facility (ESRF) in Grenoble, France [14], the Advanced Photon Source (APS-U) in Lemont, USA [15], Sirius in Campinas, Brazil [16] and the High Energy Photon Source (HEPS) in Beijing, China [17]. The Swiss Light Source (SLS II) in Villigen, Switzerland [18] has entered its commissioning phase in late 2024 and stored beam has been achieved by the end of January 2025.

1.2. Motivation

As discussed in the previous section, the advancement in storage ring technology has pushed the achievable brightness of the light available for experiments and consequently increased the range of wavelengths λ that can be produced at the diffraction limit. With ultra-low emittances, especially for the planned PETRA IV storage ring, the size of the electron beams will be in the range of a few tens of µm (in average). These hair-thin beams will posses unprecendented high charge density in storage rings and will consequently increase the probability of electrons interacting within the bunch. These unavoidable interactions will lead to an overall decrement in beam lifetime and for high bunch intensities to deterioration of the emittance. Therefore the motivation of this thesis has been centered around an effective way to mitigate these undesired consequences of ultra-low emittance electron beams.

Primarly, the focus of previous generation synchrotron light sources was directed towards the development of insertion devices. The advancement of linear electron beam optics also took place, since it determines the electron beam quality, which ultimately impacts the radiation quality. The fourth-generation relies on even more sophisticated linear optics designs to reduce the emittance ϵ_0, which in return amplify non-linear aberrations in the electron beam optics. Hence, not only linear but also nonlinear dynamics require significant efforts to be optimized during design. On the other hand, linear and non-linear resonant phenomena have taken a secondary role in synchrotron light sources. These phenomena regarded as "second order effects" have however harmful effects to the performance of the accelerator, e.g. they reduce the available region where stable motion takes place or can be responsible for the generation of undesired halo distributions.

In other particle accelerators though, these effects are actively exploited for advanced beam manipulations, e.g. transversal beam size control and sophisticated extraction schemes. Therefore in this thesis potential applications of linear and non-linear resonant phenomena are explored. In first instance, the mitigation of detrimental side effects due to ultra-low emittance electron beams in PETRA IV is evaluated. A first application of resonant phenomena is found to be the shaping of the beam by exploiting the emittance sharing mechanism. This is triggered by making use of the coupling or difference resonance.

Moreover, an emergent non-linear resonant effect is discovered during this endeveour. Namely, the formation of quasi-stable resonant islands. These studies showcase the first example of resonant dynamics in fourth-generation light sources, where these resonant islands are mainly triggered by amplitude dependent effects in the dynamics.

Finally, thanks to the mitigation techniques applied, an enhancement of the beam lifetime is predicted by simulation. This translates into potential operation modes of PETRA IV, that would only require the booster synchrotron for a few minutes each hour. This idle time presents an opportunity to explore whether the booster could be simultaneausly deployed to deliver high-quality electron beams to DESY's existing high-energy physics users. Consequently, studies have been conducted on this topic, leading to the proposal of a novel method for resonantly extracting electrons from the booster. It appears that unlocking the full potential of fourth-generation light sources requires a deep understanding and effective utilization of both linear and nonlinear resonances.

In the following section the PETRA IV project is introduced and general details are included.

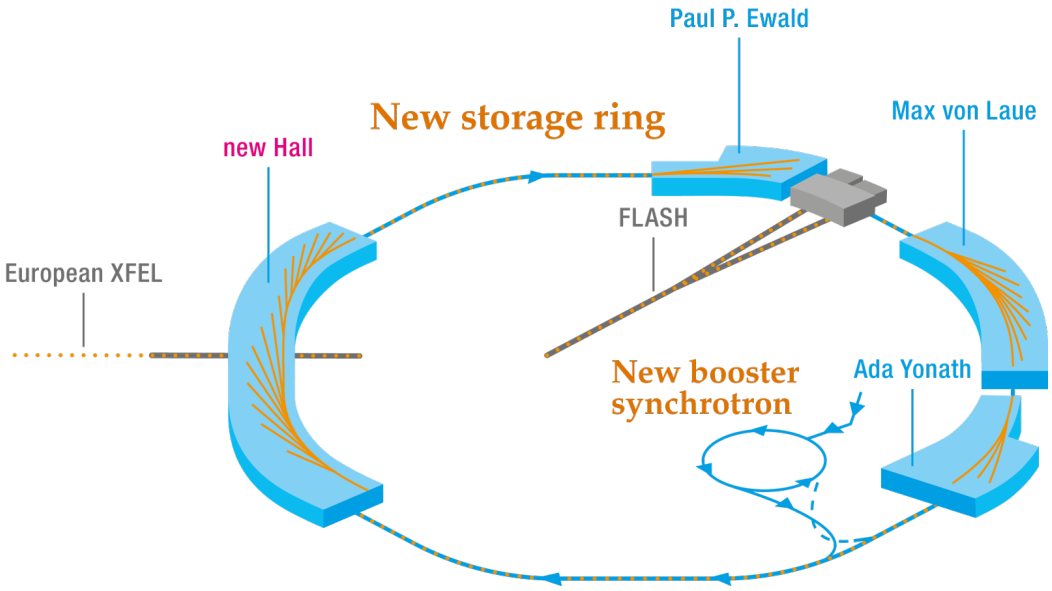

Figure 1.3: Schematic of the planned upgrade at DESY, Campus Bahrenfeld in Hamburg, Germany. The two linear particle accelerators —the European X-ray Free Electron Laser (XFEL) and the Free electron LASer at Hamburg (FLASH)— are shown. The expected upgrade will encompass the construction of a new experimental hall, the upgrade of the storage ring and the synchrotron booster. Picture taken from the CDR [19] and adapted to highlight the new storage ring and booster synchrotron.

1.3. PETRA IV project

PETRA III at its conception required a modest amount of hardware upgrades for its conversion from a booster ring into a synchrotron light source. Its circumference of 2.3 km allowed the machine to easily achieve one of the lowest natural emittances amongst the landscape of third-generation light sources. This is illustrated in figure 1.2. However, this also meant that the loss of competitiveness due to the emergence of upgraded facilities would only become apparent after several years of operation [20]. Consequently, the idea of an upgrade dates back to 2015 [21], six years after its commissioning [22]. The upgrade project has gone through different stages of sophistication; already a concept design report (CDR) has been completed [19]. By the time of writing of this thesis, the technical design has been finished.

The PETRA IV project encompasses the upgrade of the main storage and booster ring to operate as a fourth-generation synchrotron light source at DESY's Campus Bahrenfeld in Hamburg. Additionally, a new experimental hall will be constructed to accommodate approximately half of the future available beamlines. A schematic of the planned upgrade of the infrastructure is depicted in figure 1.3. Until now 31 beamlines are planned but ultimately this number can vary as the project solidifies.

A huge effort is pursued to coordinate and plan all critical systems. In Chapter 3 the details of the storage and booster ring designs from the beam dynamics perspective will be summarized. Many of the details exposed in Chapter 3 are based on the information found in [23] and the CDR [19]. These results will be discussed in detail in Chapter 4, since they will serve as a comparison for the machine's performance with round beams. Many engineering and technical design aspects that are essential for the realization of the project

are not discussed in this thesis, but are well documented in the concept and technical design reports.

1.4. Detailed overview of this thesis

The present Chapter 1 introduces the reader into the topic, motivates the investigations and gives an overview of the outline of this thesis. Relevant contributions made to scientific literature are listed in Section 1.5.

In Chapter 2 the theory relevant for the investigations performed is summarized. More specifically

- Section 2.1-3: Linear dynamics, radiation damping and diffusion, non-linear dynamics

  These sections are primarly introduced as reference for nomenclature. They are meant to be an *accelerator physics primer*. In these sections the main building block of the storage ring is introduced: the hybrid six-bend achromat cell, a novel design developed for PETRA IV by P. Raimondi. It is taken to illustrate and exemplify some of the concepts layed out.

- Section 2.4: Round beam dynamics

  Here the round beam dynamics are discussed in detail. Three subsections lay out important, although not novel techniques to produce round beams —vertical dispersion waves, AC dipole excitation and emittance sharing. Simple theoretical predictions will be presented and later compared to simulations performed for the PETRA IV storage ring.

- Section 2.5 Collective phenomena

  In this section relevant concepts of collective dynamics are reviewed. Although these topics have been intensively studied and are easily available in the technical literature, some phenomena emerging through the round beam generation are non-trivial. Subsection 2.5.1 Touschek scattering reviews the Piwinski formulae for coupled beam dynamics and related phenomena. Subsection 2.5.2 Intra-beam scattering elaborates on the work of Piwinski, Mtingwa and Björken making emphasis on comparing the round and flat beam cases. A review of the completely integrated modified Piwinski formulae is presented and calculations are shown for the building block of PETRA IV. Due to the limited nature of the doctoral project, only the intra-beam and Touschek scattering effects are discussed thoroughly. Some remarks on the importance of the round beam operation to wakefields and space-charge are included in this chapter.

Then in Chapter 3 the general layout of the PETRA IV storage ring and its booster synchrotron is discussed. The beam dynamics performance is summarized and certain aspects involving the machine protection and collimation strategy are documented. Information about the booster design, off-axis injection, filling patterns and important figures of merit is given. It is worth noting that the work presented here is mainly the results of collaborative

efforts of the PETRA IV beam physics group. Whenever relevant contributions are done by other researchers, this will be emphasized.

In Chapter 4 the round beam operation for the PETRA IV storage ring is discussed in detail. Numerous simulation results are presented and compared to the concepts presented in Chapter 2, Subsections 2.4 and 2.5. Some simulations were performed in close collaboration with C. Li. When these are presented, they will be clearly indicated.

The main impact to the beam dynamics performance can be summarized as follows

- The Touschek scattering rate is decreased and the local momentum acceptance and dynamic aperture are not considerably perturbed by operating with a round beam. This leads to an increase of the beam lifetime by a factor of two with any total beam current.
- The intra-beam scattering rate is decreased with a round beam operation, this allows for the transverse equilibrium emittances to always be kept under 20 pm rad even for high single bunch charge operation (<2.5 mA).
- Simulations show that the injection efficiency is kept in excess of 99%, if the injected beam manipulations are considered, namely the emittance exchange scheme.

The consequences of the advantages of the round beam operation are discussed and weighted with the operational challenges that have been identified. Followed by this, a soft transition is made by introducing the considerations of an off-axis injection at PETRA IV in Section 4.3. Experimental campaigns pursued at PETRA III and ESRF are then reported. Simulations and experiments on the off-axis injection scheme were conducted throughout this thesis. Additionally, simulation results for PETRA IV revealed the formation of transverse quasi-stable resonant islands.

In Chapter 5 a continuation of the study of this phenomenon is discussed. Experimental campaigns have been pursued at ESRF to confirm the existence of the islands and characterize them. The effective Hamiltonian commonly used to describe the dynamics near the third order resonance is discussed. Simulation and experimental results from the investigations are documented in this chapter. These results illustrate the first example of resonant electron dynamics observed in a fourth-generation synchrotron light source with working points far from low order resonances.

In Chapter 6 a brief motivation of a concept study for a resonant slow extraction of electrons from the planned booster ring, DESY IV is incorporated. The proposed scheme to perform a resonant slow extraction from a low-emittance booster ring involves the generation of transverse resonance island buckets (TRIBs), a novel variant of the slow extraction method. To conclude, in Chapter 7 a summary and discussion of all the results presented along this thesis are included. A list of conclusions finalizes the work.

1.5. List of publications

During the course of this thesis following articles were published or submitted to academic journals:

- [24] E. C. Cortés García, I. V. Agapov, and W. Hillert, "Design of a resonant slow extraction from low-emittance electron booster rings using transverse resonance island buckets," *Phys. Rev. Accelerators and Beams*, vol. 28, p. 011601, Jan 2025. https://doi.org/10.1103/PhysRevAccelBeams.28.011601.
- [25] E. C. Cortés García and I. Agapov, "Dynamics of off-axis injection near the coupling resonance at PETRA IV," *Journal of Physics: Conference Series*, vol. 2687, p. 032039, January 2024. https://dx.doi.org/10.1088/1742-6596/2687/3/032039.
- [26] E. C. Cortés García, P. Niedermayer, R. Singh, R. Taylor, E. Feldmeier, M. Hun, E. Benedetto and T. Haberer, "Interpretation of the horizontal beam response near the third integer resonance". *Physical review accelerators and beams*, vol. 27, no. 12, p. 124001, Dec 2024. https://doi.org/10.1103/PhysRevAccelBeams.27.124001.
- [27] S. A. Antipov, V. Gubaidulin, I. Agapov, E. C. Cortés García and A. Gamelin, "Space charge effects in fourth-generation light sources: The PETRA IV and SOLEIL II cases", *Phys. Rev. Accelerators and Beams*, vol. 28, p. 024401, Feb 2025. https://doi.org/10.1103/PhysRevAccelBeams.28.024401.

The contribution reported in [24] was supervised closely by I. Agapov and W. Hillert with the majority of the conceptual work and investigations performed by myself. The work reported in [25] was conducted under supervision of I. Agapov and presented in 2023 in the International Particle Accelerator Conference in Venice, Italy. The contribution [27] was lead by S. Antipov in close collaboration with V. Gubaidulin and myself, under the supervision of I. Agapov and A. Gamelin. Further, the contribution found in [26] was a collaborative effort between GSI, CERN and Heidelberg Ion-Therapy Center colleagues proposed and led by myself under supervision of E. Feldmeier, E. Benedetto and T. Haberer. Only the work documented in [24, 25] is presented in this thesis.

The following contributions were made throughout the course of this thesis, albeit the involvement was indirect:

- [23] I. Agapov, S. Antipov, R. Bartolini, R. Brinkmann, Y.-C. Chae, E. C. Cortés García, D. Einfeld, T. Hellert, M. Huening, M. A. Jebramcik, J. Keil, C. Li, L. Malina, and R. Wanzenberg, "Beam dynamics performance of the proposed PETRA IV storage ring", 2024. Pre-print available at: https://arxiv.org/abs/2408.07995
- [28] P. J. Niedermayer, R. Singh, G. Franchetti, E. C. Cortés García, E. Feldmeier, and T. Haberer, "Investigation of micro spill in RF KO extraction using tailored excitation signals," *Journal of Physics: Conference Series*, vol. 2687, p. 052029, Jan 2024.

In [23] results presented in this thesis are shown. The simulations were produced in close collaboration with C. Li. The work reported in [28] was lead by P. Niedermayer under supervision of R. Singh and G. Franchetti. I conducted the experiments and contributed to the preliminary analysis of experimental data.

Finally, the following contributions will be presented in the International Particle Accelerator Conference 2025 in Taiwan:

- E. C. Cortés García, I. Agapov, S. Antipov and C. Li, “Considerations of a round beam operation at PETRA IV”, IPAC25, June 2025.
- E. C. Cortés García and I. Agapov, “Vertical emittance control with a beam shaker for PETRA IV,” IPAC25, June 2025.
- S. Antipov, I. Agapov and E. C. Cortés García, “Space charge limit for light sources,” IPAC25, June 2025.
- S. Antipov, I. Agapov, N. Carmignani, L. Carver, E. C. Cortés García and S. White. “Increasing single-bunch intensity limit at ESRF-EBS with high coupling,” IPAC25, June 2025.
- N. Carmignani, I. Agapov and E. C. Cortés García. "Observation of transverse resonance island buckets at the ESRF EBS". IPAC25, June 2025.
- E. C. Cortés García, I. Agapov and G. Kube. "Design of a resonant slow extraction from the planned DESY 4 booster synchrotron". IPAC25, June 2025.

This list may have to be revisited in the final version, but all the work that will be presented in the conference is related to work performed during this thesis.

2

Theoretical background

This chapter recompiles some of the basic, accepted, established and developing concepts from the theoretical background surrounding the description of the dynamics of charged particles in particle accelerators. The discussion is limited to the results known for circular machines, especially for electron storage rings. Where evident, the benefits of a round beam operation are highlighted. The hybrid six-bend achromat cell is introduced as well to exemplify some of the theoretical concepts. This cell is the building block of the future PETRA IV main storage ring. Although this compilation is not intended to be extensive nor complete, it should aid as a practical reference for notation along this thesis. Better material of general and selected topics of particle accelerators can be found in standard textbooks [29, 30, 31, 32].

2.1. Linear dynamics

The dynamics of charged particles in accelerators and their corresponding subsystems are generally described with respect to a co-moving reference particle, which defines the coordinate system. The particle dynamics encompasses the description of motion in a 3D space under the influence of external or self-induced electromagnetic fields as it evolves along the particle accelerator or machine. The information is fully encoded in the particle's 6D state vector $\vec{Z}$, where the space coordinates and their conjugate coordinates are stored. These pairs are not necessarily canonical as in analytical mechanics derived from the Hamilton-Jacobi formalism. The search for equations of motion (EQoM) has been initially derived from Newtonian principles involving the Lorentz force. Linearization of these and their corresponding solutions have lead to stable foundations of the description of particle dynamics in particle accelerators. These results are described in the next section. The extension of linear dynamics to treat more complex non-linear phenomena involve the linear dynamics as a starting point.

2.1.1. Transversal dynamics

Contemporary circular particle accelerators commonly rely on the magnetic force to restrict the motion of charged particles to follow a curved path[1]. In this thesis only the linear dynamics

[1] A rather unique exception is the Cryogenic Storage Ring at the Max Planck Institute for Nuclear Research [33]. This compact storage ring contains only electrostatic optical elements.

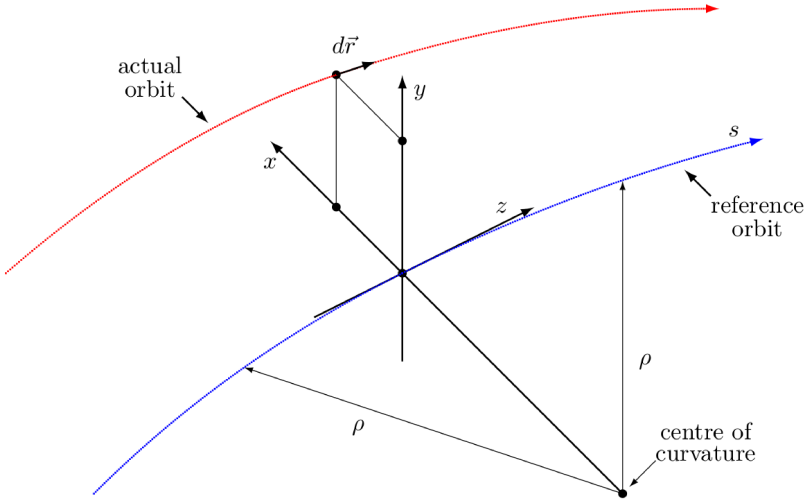

Figure 2.1: Illustration of the reference coordinate system in a circular particle accelerator. Figure taken from the MADX documentation [34].

of circular accelerators known as synchrotrons and storage rings is discussed. The main components of such machines include bending magnets to keep particles in orbit, quadrupole magnets for strong focusing and radio-frequency (RF) cavities to accelerate or bunch particles. With these one can build a circular lattice that can be referred to as a linear machine, in the sense of its transversal particle dynamics. The transversal EQoM can be reduced to a set of Hill's differential equations

$$\begin{aligned} x'' + K_x(s)x &= \delta/\rho(s), \\ y'' + K_y(s)y &= 0. \end{aligned} \tag{2.1}$$

The x coordinate is found in the horizontal plane with regard to the ideal reference particle and in the laboratory reference system, x is positive if a particle deviates radially outwards and negative otherwise. The vertical plane is described with the y coordinate and coincides with the usual Cartesian perception. The longitudinal coordinate is defined along a reference orbit and replaces the time coordinate. An illustration of this local reference coordinate system is presented in figure 2.1.

In equation 2.1 the coordinate $\delta = (p - p_0)/p_0$ is the relative momentum deviation and is to be treated as the conjugate of the longitudinal position along the reference orbit s. The bending radius along the reference orbit is represented with $\rho(s)$. Together with ρ, the functions $K_{x,y}(s)$ are periodic such that $K_{x,y}(s + C) = K_{x,y}(s)$ with C representing the circumference of the circular machine. The functions $K_{x,y}(s)$ contain the information of where the quadrupoles, bending magnets or nothing is found along the reference orbit s. The places in the lattice without magnets represent also optical elements that are referred to as drifts. The existence of a solution of equation 2.1 is guaranteed by Floquett's theorem. The preferred explicit solution of equation. 2.1 in the particle accelerator community is given by the Courant-Snyder parametrization [35] and is to be computed numerically, but for a few exceptions of very simple lattices. The Courant-Snyder parametrization introduces one very important function,

known and referred to exclusively in this thesis as the optical β-function. The transversal motion of a particle along the accelerator is thus given by

$$x(s) = \sqrt{\epsilon_x^{(\mathrm{sp})}\beta_x(s)}\cos\left(\psi_x(s) + \psi_{x,0}\right) + \delta D_x(s),$$
$$y(s) = \sqrt{\epsilon_y^{(\mathrm{sp})}\beta_y(s)}\cos\left(\psi_y(s) + \psi_{y,0}\right), \tag{2.2}$$

with the phase-advance relative to an arbitrary point s_0 in the lattice

$$\psi_{x,y}(s) = \int_{s_0}^{s} \frac{\mathrm{d}\bar{s}}{\beta_{x,y}(\bar{s})}.$$

The Courant-Snyder invariant $\epsilon_{x,y}^{(\mathrm{sp})}$ together with $\psi_{0,x,y}$ are determined by initial conditions. The upper index 'sp' makes reference to the **s**ingle **p**article nature of this invariant of motion. The dispersion function $D_x(s)$ reads [29, 30]

$$D_x(s) = \frac{\sqrt{\beta_x(s)}}{2\sin\pi Q_x}\int_{s_0}^{s}\frac{\sqrt{\beta_x(\bar{s})}}{\rho(\bar{s})}\cos\left(\psi_x(\bar{s}) - \psi_x(s) - \pi Q_x\right)\mathrm{d}\bar{s}, \tag{2.3}$$

where the machine's working point or tune $Q_{x,y}$ and the betatron phase-advance $\psi_{x,y}$ are given by

$$Q_{x,y} = \frac{1}{2\pi}\int_{s_0}^{s_0+C}\frac{\mathrm{d}s}{\beta_{x,y}(s)}, \tag{2.4}$$

$$\psi_{x,y} = \int_{s_0}^{s}\frac{\mathrm{d}\bar{s}}{\beta_{x,y}(\bar{s})}. \tag{2.5}$$

The bending radius ρ is illustrated in figure 2.1. The accelerator is ring alike and there is no vertical center of curvature, thus there is usually no vertical dispersion ($D_y(s) = 0$ for $s \in [0, C]$) in an ideal machine.

To summarize, the linear transversal dynamics is reduced to the determination of the optical function $\beta_{x,y}$, which has been already implemented in multiple codes and the motion is an-harmonic along the reference orbit. It is common to assume that the lattice of the accelerator is fixed and given, i.e. that the β-function is given. An exemplary set of β-functions together with their horizontal dispersion are shown in figure 2.2. The set of functions related to the β-function are commonly referred to as optical functions.

As it will be discussed later, the non-linear dynamics treatment can be eased by the introduction of normalized coordinates (X, P_x) or (Y, P_y) and their corresponding action-angle variables (J, ϕ). They are given by

$$X = x/\sqrt{\beta_x}, \qquad Y = y/\sqrt{\beta_y}, \tag{2.6}$$
$$P_x = \alpha_x X + \sqrt{\beta_x}x', \qquad P_y = \alpha_y Y + \sqrt{\beta_y}y' \tag{2.7}$$

and e.g. for the horizontal plane

$$J_x = \frac{X^2 + P_x^2}{2}, \qquad \phi_x = \arctan\left(\frac{P_x}{X}\right). \tag{2.8}$$

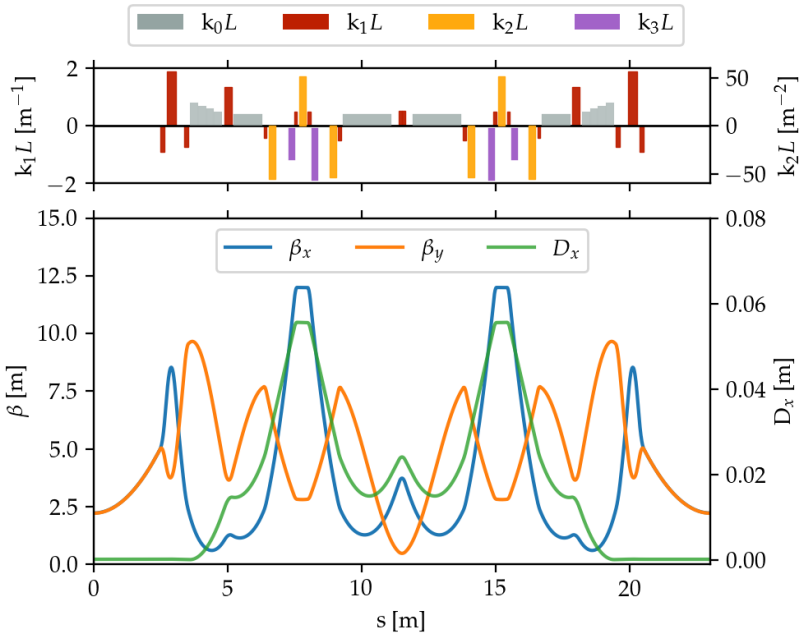

Figure 2.2: Lower panel: Optical functions of a hybrid six-bend achromat cell. Top panel: Quadrupole strength values are depicted in red. The other colored bars indicate the position of dipole bending magnets (grey), sextupole magnets (yellow) for chromatic correction and octupole magnets (lila) for enhancement of stable nonlinear dynamics. Integrated gradient fields are shown also for the sextupoles. The PETRA IV storage ring will be composed of 72 of these cells distributed equally amongst eight octants.

In equation 2.7 the α-function is related to the derivative of the β-function by $\alpha = -\beta'/2$. The action is related to the Courant-Snyder invariant through $2J = \epsilon^{(\mathrm{sp})}$.

As a last remark, to quantify the motion of many particles the rms emittance of the beam is used and defined by

$$\epsilon = \langle J \rangle = \frac{\langle \epsilon^{(\mathrm{sp})} \rangle}{2}. \tag{2.9}$$

The $\langle \cdot \rangle$ indicate an average over all the particles in the bunch in this case, but generally along this thesis it might just mean averaging over a quantity. The rms beam size is thus given by

$$\sigma = \sqrt{\beta\epsilon + (D\sigma_\delta)^2}. \tag{2.10}$$

The symbol σ_δ refers to the rms of the momentum deviation of the particle ensemble.

2.1.2. Longitudinal dynamics

To continue with a soft transition to the longitudinal dynamics, the momentum compaction factor is introduced [31]

$$\alpha_c = \frac{1}{C} \int_{s_0}^{s_0+C} \frac{D(s)}{\rho(s)} \mathrm{d}s, \tag{2.11}$$

which relates the change in circumference due to a change in momentum $\Delta C/C = \alpha_c \delta$. The change in revolution frequency due to a change in momentum is given by [31]

$$\frac{\Delta f}{f} = \eta\delta = \left(\alpha_c - \frac{1}{\gamma_r^2}\right)\delta. \tag{2.12}$$

The longitudinal dynamics can be described by the pair of coordinates $(\zeta = s - s_0 = c\Delta t, \delta)$ and their EQoM reads [30]

$$-2\pi h\eta \frac{\mathrm{d}^2\delta}{\mathrm{d}t^2} + (2\pi Q_s f_{\mathrm{RF}})^2 \sin(-2\pi h\eta\delta) = 0$$

with the synchrotron tune given by

$$Q_s = \frac{1}{\beta_r}\sqrt{\frac{h|\eta|}{2\pi}\frac{qU_{\mathrm{RF}}}{\gamma_r m_0 c^2}}. \tag{2.13}$$

Here the RF cavity provides longitudinal acceleration with a sinusoidal wave $\Delta E = qU_{\mathrm{RF}} \sin(2\pi f_{\mathrm{RF}} t)$. The sub-index in $\gamma_r = 1/\sqrt{1-\beta_r^2}$ and $v = \beta_r c$ makes the distinction between relativistic factors and machine optical functions. In equation 2.13 c stands for the speed of light, m_0 for the rest mass of the charged particle accelerated and finally the harmonic number h has to fulfill the relation $f_{\mathrm{RF}} = h f_{\mathrm{rev}} = h\beta_r c/C$.

Chromatic correction

The transversal dynamics are coupled to the longitudinal as can be seen from equation 2.2. In addition, the focusing gradient $K(s)$ is effectively changed, when there is a relative momentum deviation δ. Hence the β-functions are perturbed such that the tunes deviate by $(Q_x + \Delta Q_x, Q_y + \Delta Q_y)$ with

$$\Delta Q_{x,y} = \xi_{x,y}\delta, \tag{2.14}$$

where $\xi_{x,y}$ is called the (linear) chromaticity. The chromaticity is composed of two contributions, the natural chromaticity $\xi^{(\mathrm{nat.})}$ and the chromaticity correction $\xi^{(\mathrm{corr.})}$ such that

$$\xi_{x,y} = \xi^{(\mathrm{nat.})} + \xi^{(\mathrm{corr.})}. \tag{2.15}$$

The natural chromaticities are given by [31, 30]

$$\xi_{x,y}^{(\mathrm{nat.})} = \frac{\partial Q}{\partial \delta} = -\frac{1}{4\pi}\int_{s_0}^{s_0+C} \mathrm{d}s\,\beta_{x,y} K_{x,y} \tag{2.16}$$

and are characteristic of the machine and its optical functions. Control and correction of the chromaticity is performed with dedicated sextupoles. The chromatic correction due to sextupoles reads

$$\xi_{x,y}^{(\mathrm{corr.})} = \pm\frac{1}{4\pi}\int_{s_0}^{s_0+C} \mathrm{d}s\,\beta_{x,y} D_x k_2, \tag{2.17}$$

here $k_2 = \frac{1}{B\rho}\frac{\partial^2 B}{\partial x^2}$ represents the sextupole gradient in $[\mathrm{m}^{-3}]$. The integrated sextupole gradient will be referred as the sextupole strength $k_2 L$. The vertical plane experiences a correction with opposite sign, hence chromaticity correction usually involves pairs of focusing and defocusing sextupoles. In figure 2.2 the values to correct and control the chromaticity are shown in the upper panel as yellow bars.

2.2. Radiation damping and diffusion

In electron storage rings one important component in the dynamics is the emission of electromagnetic radiation, also known as synchrotron radiation. It results from the acceleration of charge particles and was described by Schwinger in 1945 [36]. This phenomenon has an important consequence in the dynamics, since the motion is damped and stochastically diffused. Including these effects, the horizontal EQoM of the emittance is given by [32]

$$\frac{\mathrm{d}\epsilon_x}{\mathrm{d}t} = -\frac{2}{\tau_x}\left(\epsilon_x - \epsilon_{0,x}\right), \tag{2.18}$$

$$\tau_x = \frac{2}{j_x}\frac{E}{U_0}T_{\mathrm{rev}}, \tag{2.19}$$

where τ_x is the damping time, given by the partition number j_x, the total energy of the particle $E = \gamma_r m_0 c^2$ and U_0 the radiated energy loss over one turn. The horizontal equilibrium emittance ϵ_0 can be derived with help of five so called "radiation integrals" introduced by M. Sands [37, 38]. The first integral is related to equation 2.11 by $I_1 = C\alpha_c$. The second and third are integrals over inverse powers of the local bending radius

$$I_2 = \int_{s_0}^{s_0+C} \frac{\mathrm{d}s}{\rho^2}, \tag{2.20}$$

$$I_3 = \int_{s_0}^{s_0+C} \frac{\mathrm{d}s}{|\rho|^3}, \tag{2.21}$$

and the last two are defined by

$$I_4 = \int_{s_0}^{s_0+C} \frac{D}{\rho}\left(\frac{1}{\rho^2} + 2K\right)\mathrm{d}s, \tag{2.22}$$

$$I_5 = \int_{s_0}^{s_0+C} \frac{\mathcal{H}}{|\rho|^3}\mathrm{d}s. \tag{2.23}$$

The $\mathcal{H}$-function (curly-H) is defined as

$$\mathcal{H} = \gamma D^2 + 2\alpha D D_p + \beta D_p^2, \tag{2.24}$$

where the optical functions of the storage ring (β, α, γ) are assumed to be given. The dispersion function D is described by equation 2.3 and D_p refers to its derivative with respect to s. With this set of integrals that characterize the machine, the equilibrium emittance reads

$$\epsilon_{0,x} = \frac{C_q \gamma_r^2}{j_x}\frac{I_5}{I_2}, \tag{2.25}$$

where γ_r represents the relativistic gamma factor and $C_q = 55\hbar/(32\sqrt{3}m_0 c)$.

The damping partition numbers (j_x, j_y, j_z) are given by the radiation integrals and follow the Robinson theorem [39]

$$j_x = 1 - \frac{I_4}{I_2}, \qquad j_z = 2 + \frac{I_4}{I_2}, \qquad j_x + j_y + j_z = 4. \tag{2.26}$$

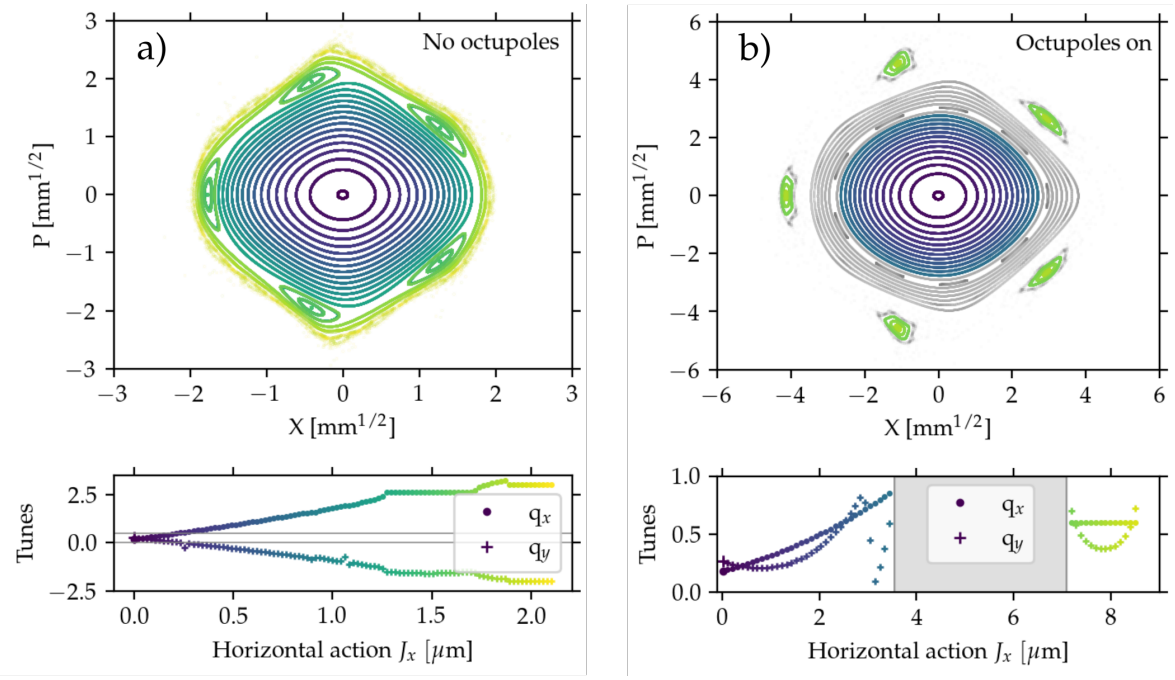

Figure 2.3: Horizontal phase-space portrait of a 72 hybrid six-bend achromat (H6BA) cell lattice with corrected chromaticity ($\xi_{x,y} = 0$). (a) On the left upper panel the phase-space portrait is shown without the introduction of octupoles, color coding represents the equipotential line and their corresponding horizontal action value. The left lower panel also shows the fractional tune as a function of action. (b) The panels on the right display the same information as in (a) but with the introduction of octupoles. The grey zones indicate unstable motion, when motion happens in both transversal planes. Note that the horizontal and color scales are different in both panels hinting at the increased stability due to octupole correction. The values of the optical functions at the observation point are $\beta_{x,y} = 2.4\,\mathrm{m}$ with vanishing $\alpha_{x,y} = 0$.

The damping times of every plain, where motion takes place is analogous to equation 2.19 but with their corresponding damping partition numbers. Thorough derivations of equations 2.18 to 2.26 can be found in [30, 31, 32] and are essential for the design and study of the beam dynamics in electron storage rings. The lower limit of the vertical equilibrium emittance is given by [40]

$$\epsilon_{0,y}^{(\mathrm{min})} = \frac{13}{55}\frac{C_q}{I_2}\int_{s_0}^{s_0+C}\frac{\beta_y}{|\rho^3|}\mathrm{d}s. \tag{2.27}$$

2.3. Non-linear dynamics

The study and natural extension of the linear into the realm of non-linear dynamics has been a subject of interest for many fields. When a system becomes non-linear suddenly the discussion shifts towards the study of resonances. This is not only because the explicit solution of EQoM might not be analytically available, but a set of phenomena arises, that can make the evolution of the system unpredictable i.e. chaotic [41, 42]. Loosely speaking, linear systems involve the study of the solution of EQoM. Intuition suggests that all known linear systems have known solutions. Additionally the study of non-linear dynamics has led to the conclusion, that there

are certain emergent phenomena characteristic of certain system states. These phenomena are accentuated in the study of parametric resonances in particles accelerators.

In the particle accelerator community, the tools have shifted to the Lie-algebraic formulation of transfer maps induced by Hamiltonians of different elements [43, 44]. The Lie-algebra will not be reviewed, but some important conclusions and corollaries for the non-linear dynamics will be discussed. In the majority of the cases, a more straightforward approach can be found, while the complicated and heavy machinery of the Lie-algebraic approach can be avoided. The main focus centers around the Hamiltonian formulation of the non-linear dynamics and from there derive the characteristics that will be taken advantage of.

As discussed briefly in Subsection 2.1.2 sextupoles are introduced for chromatic correction. These elements in the lattice introduce a non-linear component in the EQoM. Moreover non-linear components such as octupoles are commonly introduced to control the change of tune with motion amplitude. Figure 2.3 illustrates clearly the expected behaviour of parametric resonances driven by non-linear elements in the lattice. Notice that first, the tunes (Q_x, Q_y) will not only depend on the optics of the machine as described in equation 2.4 but also on the initial amplitude of motion, essentially $\epsilon^{(\mathrm{sp})}$ or equivalently on their actions (J_x, J_y). In figure 2.3 only the horizontal action is varied and this is shown in the lower panels. The fractional part of the tunes are plotted, where $(Q_x, Q_y) = (n + q_x, m + q_y)$ with $n, m \in \mathbb{N}_0$. The tune dependence on both transversal actions is depicted in figure 2.4.

Secondly, the generation of resonance islands can be observed in figure 2.3. At low amplitudes ($J_x \approx 0$) the motion is regular and follows clearly a torus in phase-space, characteristic of harmonic oscillations. When the amplitude increases and therefore the tunes change their values, the motion crosses parametric resonances. In this case they lead to the generation of five transverse resonance islands. Features like these have been long topic of discussion in the particle accelerator field and they have found useful applications (e.g. [45, 46, 47, 48, 49, 50, 51, 52, 53]). Many archetypes of non-linear oscillator systems have been studied and their characterization is still an active field of research. In this section some light definitions of resonances are layed out and leave the introduction of the necessary theory to dedicated sections. Sections where the theory of parametric resonances will be discussed are Section 2.4 and 6.1.

2.3.1. Resonances

Before laying out the results available in the literature the definition of what resonances are, is formalized. Along this thesis two general types of resonant phenomena are distinguished:

- Systematic resonance: Motion is driven externally by some excitation. If the excitation is periodic and matches the eigenfrequency of the system, then we have a resonance driven systematically.
- Parametric resonance: Motion of the system is "driven" by itself by some perturbation or modulation of its frequency. A parameter of the system is varied, that is the implication.

Both type of resonances are studied to shape and control the motion of particles. Systematic resonances are useful for increasing the amplitude of motion of stored electrons, whereas parametric resonances are used to achieve a desired characteristic in the motion determined by the resonance — especial shape in phase-space such as islands or energy exchange between motion planes.

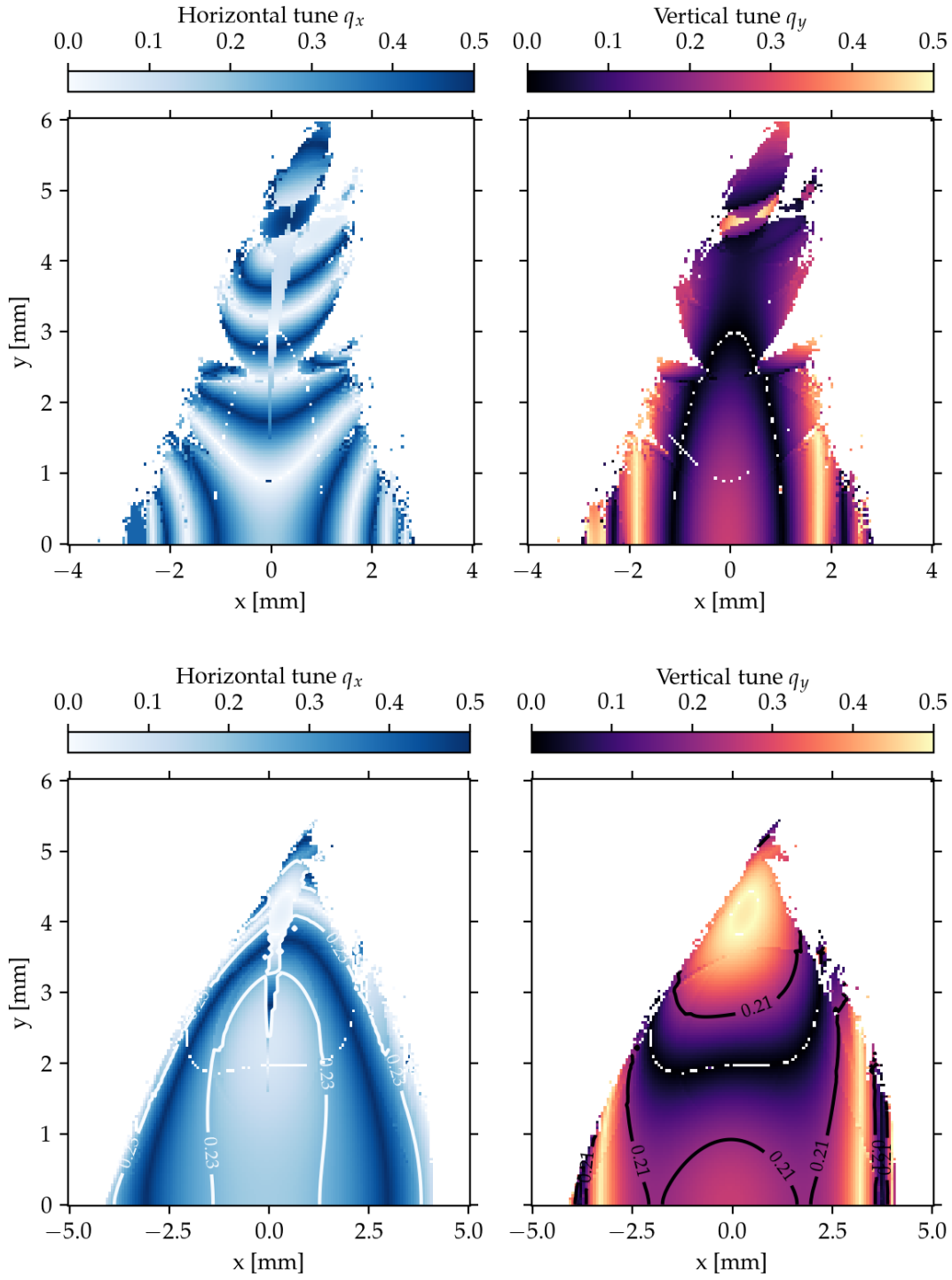

Figure 2.4: Frequency map of a 72 H6BA cell ring. The upper panels illustrate the results of a ring with ocutpoles off, while in the lower panels the octupoles were turned on. Notice as well the different horizontal scale. The values of the optical functions at the observation point are $\beta_{x,y} = 2.4\,\mathrm{m}$ with vanishing $\alpha_{x,y} = 0$.

Systematic resonance
In particle accelerators, the way to excite the transversal motion of particles through external excitations is by introducing an element in the lattice that effectively gives kicks (changes in momentum) to the particle. This is done by making use of AC dipoles and/or stripline kickers. If the frequency of the external excitation Ω matches the one of the system ω, then the motion will be driven resonantly. Concretly, one can drive the betatron motion by setting an external electromagnetic wave with the frequency $2\pi|n \pm Q|f_{\text{rev}}$, where Q is the tune described by equation 2.4 and $n \in \mathbb{N}_0$. This will turn the motion of the stored electrons into quasi (damped) driven harmonic oscillations.

Parametric resonance
More interesting is the excitation of parametric resonances in particle accelerators. To excite parametric resonances, first the resonance condition [41, 42]

$$nq_x + mq_y = l, \qquad n, m, l \in \mathbb{Z}_0, \tag{2.28}$$

has to be met. Here (q_x, q_y) refer to the fractional part of the tunes, such that $(Q_x, Q_y) = (N + q_x, M + q_y)$ with $N, M \in \mathbb{N}_0$. Moreover there must exist a resonance driving term (RDT) sufficiently strong to drive the motion of the particle. The second condition appears to be not always necessary, depending on the system, e.g. Chirikov's standard map or high dimensional coupled oscillator systems. In particle accelerators parametric resonances have to be explicitly driven by some set of optical elements, e.g. skew quadrupoles, sextupoles or octupoles.

Integer and half integer resonances are driven by dipole and quadrupole fields, respectively and approaching them usually lead to beam loss. This means that $q_{x,y} = n/2$ or $q_{x,y} = n$ with $n \in \mathbb{N}_0$ should be actively avoided. The manipulation of phase-space by setting the working point of the machine (q_x, q_y) close to a resonance has been studied intensively [54]. Along this thesis the generation of round beams by driving the coupling resonance is discussed, namely when $q_x = q_y$ and the setup of a resonant slow extraction from the booster ring by driving the horizontal third order resonance $3q_x = 1$. Additionally the generation of stable resonance islands is observed in hybrid multi-bend achromats. This emerging phenomenon happens also by exciting the third order resonance, unintentionally. A discussion of this observation is postponed to Chapter 5.

2.4. Round beam dynamics

Along this thesis a round beam is defined with regard to its transversal emittances ϵ (see equation 2.9). Namely, a beam is called round, if its transversal emittances are equal

$$\epsilon_x = \epsilon_y. \tag{2.29}$$

From the dynamics discussed in previous sections, the transversal emittances follow equation 2.18 and obtain the equilibrium values of $\epsilon_{0,x}$ and $\epsilon_{0,y}^{(\text{min})}$ given by equations 2.25 and 2.27 respectively in an ideal machine.

Generally speaking, the minimum vertical emittance of an ideal lattice is at least a couple of orders of magnitude lower than the equilibrium horizontal emittance. To illustrate this

situation only with a hand-waving argument, one can observe that

$$\frac{\epsilon_{0,x}}{\epsilon_{0,y}^{(\min)}} = \gamma_r^2 \frac{55}{13} \frac{I_5}{\int_{s_0}^{s_0+C} \frac{\beta_y}{|\rho^3|} \mathrm{d}s}.$$

If one assumes that the integral in the denominator can be approximated by $(2\pi)^3 \bar{\beta}_y / C^2$ and take the values for PETRA IV (or any other synchrotron light source), then the horizontal emittance $\epsilon_{0,x}$ is approximately five orders of magnitude higher than $\epsilon_{0,y}^{(\min)}$. Even in a non-ideal machine, where vertical dispersion is generated the equilibrium vertical emittance is at most a few percent of $\epsilon_{0,x}$. Therefore if a round beam operation is desired, a method to generate vertical emittance has to be engineered. There are at least three straight forward ways in which vertical emittance can be generated. In this thesis the possibility of controlling the equilibrium vertical emittance with three different methods is discussed: AC dipole excitation, vertical dispersion waves and emittance sharing. The results from numerical studies will be presented in Chapter 4.

2.4.1. Vertical dispersion waves

The first method considered is the generation of vertical dispersion waves. Analogously to the horizontal plane one can generate vertical dispersion by introducing vertical bending. This can be achieved with dedicated sections with vertical bending or with the appropiate use of vertical orbit correctors in the H6BA cells. In this case vertical dispersion is generated as in the horizontal plane (equation 2.3)

$$D_y(s) = \frac{\sqrt{\beta_y(s)}}{2 \sin \pi Q_y} \int_{s_0}^{s} \frac{\sqrt{\beta_y(\bar{s})}}{\rho_y(\bar{s})} \cos\left(\phi_y(\bar{s}) - \phi_y(s) - \pi Q_y\right) \mathrm{d}\bar{s}.$$

Thus the vertical equilibrium emittance is given by equation 2.25

$$\epsilon_{y,0} = C_q \gamma^2 \frac{I_{5,y}}{I_2} \qquad \text{with} \qquad I_{5,y} = \oint \frac{\mathcal{H}_y}{|\rho_y|^3} \, \mathrm{d}s \, .$$

This approach will be implemented in the Swiss Light Source II at the Paul Scherrer Institute in Villigen, Switzerland [18].

2.4.2. AC dipole excitation

As the second method the ansatz utilised at ESRF for controlling the vertical emittance [55] is followed. This is done by exciting the motion by making use of a set of kickers, that drive the oscillations (systematically) resonantly. The dynamics of the vertical betatron motion are described by equation 2.2. Including the damping in the dynamics leads to the effective EQoM in time domain

$$\ddot{y} + 2\lambda_y \dot{y} + \omega_\beta^2 y = 0$$

with $\omega_\beta = 2\pi Q_y f_{\mathrm{rev}}$. The revolution frequency is given by $f_{\mathrm{rev}} = c/C$, if the electron beam is ultra-relativistic. The main idea of the AC dipole excitation is to excite the vertical motion with an external electromagnetic wave. This in return leads to

$$\ddot{y} + 2\lambda_y \dot{y} + \omega_\beta^2 y = F(t), \tag{2.30}$$

where $F(t)$ is an arbitrary function of time. In principle, any function $F(t)$ would lead to an increment of the vertical betatron motion. In the following two common choices for $F(t)$ are considered. Namely, a sinus wave that acts resonantly on the unperturbed oscillation and a noise band that resembles the effect of a stochastic diffusion, as in the horizontal plane.

Sine wave excitation
When the beam is excited with a single sine wave, whose frequency lies exactly at the betatron resonance $f_\beta = q_y f_{\mathrm{rev}}$ ($\omega_\beta = 2\pi f_\beta$), the system can be treated as a forced damped harmonic oscillator. The excitation signal has thus the form $F(t) = f_0 \sin \omega_\beta t$. It follows then for the long term behaviour ($t \gg \tau_y, \tau_y$: vertical damping time) of the vertical motion of one particle with momentum deviation δ

$$y(t;\delta) \approx \frac{f_0}{2\omega_\beta^2} \frac{\cos(\omega_\beta t + \phi_0)}{\sqrt{(\bar{\xi}_y \delta)^2 + (\lambda_y/\omega_\beta)^2}}, \qquad \phi_0 = \arctan \frac{-\lambda_y}{\bar{\xi}_y \delta \omega_\beta}, \tag{2.31}$$

where $\bar{\xi}_y = \xi_y / q_y$ represents the (specific) vertical chromaticity and $\lambda_y = 1/\tau_y$ the damping rate. The approximation comes from $(1 + \bar{\xi}_y \delta)^2 \approx 1 + 2\bar{\xi}_y \delta$. The explicit form of the external normalized force amplitude f_0 depends on the device providing the excitation: for a stripline kicker with length L, $f_0 \approx \theta_{\max} m_e c^3/(p_0 L)$ with $\beta_r = v/c$. Here c represents the speed of light. For an AC dipole with length L, $f_0 \approx e\beta_r c B_0 \rho_0 \theta_{\max}/(m_e L)$. $B_0\rho_0$ is as before the magnetic rigidity of the beam and m_e is the electron mass. Note that in both cases $f_0 \propto \theta_{\max}$ and thus $f_0 = \kappa \theta_{\max}$. The emittance is then

$$\epsilon_y = \frac{\sigma_y^2}{\beta_y} = \frac{I_\delta \kappa^2}{4\omega_\beta^2 \lambda_y^2 \beta_y} \frac{\theta_{\max}^2}{\bar{\xi}_y} \tag{2.32}$$

with the integral I_δ

$$\begin{aligned} I_\delta &= \int \mathrm{d}x \lim_{T\to\infty} \frac{1}{T} \int_0^T \frac{\mathrm{d}t\, P(x)}{x^2+1} \cos^2(\omega_\beta t + \phi_0) \\ &= \int \frac{\mathrm{d}x\, P(x)}{(1+x^2)^2}. \end{aligned}$$

Here $P(x)$ is the probability distribution function of the momentum deviation δ with the variable substitution $x = \omega_\beta \bar{\xi}_y \delta/\lambda_y$. The expected emittance scales with the square of the kick amplitude $\theta_{\max}^2$ and inversely proportional to the chromaticity $\bar{\xi}_y$.

Noise band excitation
To model the functional dependency on the kick amplitude $\theta_{\max}$ from the noise band signal, next the expected behavior of a beam excited with a white noise signal is considered. The white noise signal would provide random kicks to particles every turn. Depending on how the noise signal was generated the probability distribution function $P(\theta)$ of having a kick θ can change. Common choices are uniform and normal distribution functions. In both cases random kicks are assumed such that effectively a random walk process is induced. Assuming that the main source of diffusion comes from the noise signal, then the EQoM reads [44]

$$\begin{aligned} \dot{Y} &= \omega_\beta P_y, \\ \dot{P}_y &= -2\lambda_y P_y - \omega_\beta Y + \sum_n \theta_{\mathrm{noise}} \delta(t - nT_{\mathrm{rev}}) \end{aligned} \tag{2.33}$$

with $(Y, Py) = (y/\sqrt{\beta_y}, \sqrt{\beta_y}p_y + \alpha_y Y)$, $\omega_\beta = 2\pi q_y f_{\text{rev}}$, $\lambda_y = 1/\tau_y$ and τ_y represents the vertical damping time. The times series of the noise signal is represented by θ_{noise}. Equation 2.33 leads to the Fokker-Planck equation [44]

$$\frac{\partial \Psi}{\partial t} + \omega_\beta p_y \frac{\partial \Psi}{\partial y} + (-\omega_\beta y - 2\lambda_y p_y)\frac{\partial \Psi}{\partial p_y} = 2\lambda_y \Psi + D\frac{\partial^2 \Psi}{\partial p_y^2}, \tag{2.34}$$

where $\Psi = \Psi(y, p_y)$ represents the particle distribution in phase-space. Equation 2.34 yields the stationary distribution

$$\Psi_0 = \frac{\lambda_y}{\pi D} \exp\left[-\frac{2\lambda_y}{D} J_y\right], \tag{2.35}$$

where D is the diffusion coefficient and the action $2J_y = Y^2 + P_y^2$. The diffusion coefficient for noise drawn from a uniform distribution

$$P(\theta) = \begin{cases} \frac{1}{\theta_{\text{max}}}, & \text{for } \theta \in [-\frac{\theta_{\text{max}}}{2}, \frac{\theta_{\text{max}}}{2}], \\ 0 & \text{else,} \end{cases} \tag{2.36}$$

is given by

$$D = \frac{1}{2T_{\text{rev}}} \int_{\mathbb{R}} \theta^2 P(\theta)\, \mathrm{d}\theta = \frac{1}{24}\frac{\theta_{\text{max}}^2}{T_{\text{rev}}} \tag{2.37}$$

and can be interpreted as the rate of increase of the variance due to the random kicks. Analogously for an additive white gaussian noise (AWGN) $D = \sigma_\theta^2/(2T_{\text{rev}})$, $P(\theta)$ is a normal distribution and σ_θ is the rms of the signal. From equations 2.35 and 2.37, the expected average action yields

$$\begin{aligned} \epsilon_y = \langle J_y \rangle &= \int_0^{2\pi} \mathrm{d}\phi \int_0^\infty J_y \Psi_0(J_y)\, \mathrm{d}J_y \\ &= \frac{D}{2\lambda_y} = \frac{\tau_y}{T_{\text{rev}}}\frac{\theta_{\text{max}}^2}{48}. \end{aligned} \tag{2.38}$$

2.4.3. Emittance sharing

The emittance sharing mechanism is based on the exploitation of a parametric resonance that is referred to as the coupling or difference resonance. This resonance has been intensively studied in the last coupled of decades, since transversal emittance exchange is for many applications undesired. Next the results of the available theory to describe the coupled dynamics and the coupling resonance are summarized.

Coupled dynamics

There are two common magnetic components that couple the transversal beam dynamics. These are solenoidal fields and tilted or skewed quadrupolar magnetic fields. When considering these components the EQoM described by equation 2.1 can be extended to

$$\begin{aligned} x'' + K_x x &= -(K_s + S')y - 2S\zeta' \\ y'' + K_y y &= -(K_s - S')x + 2Sx' \end{aligned} \tag{2.39}$$

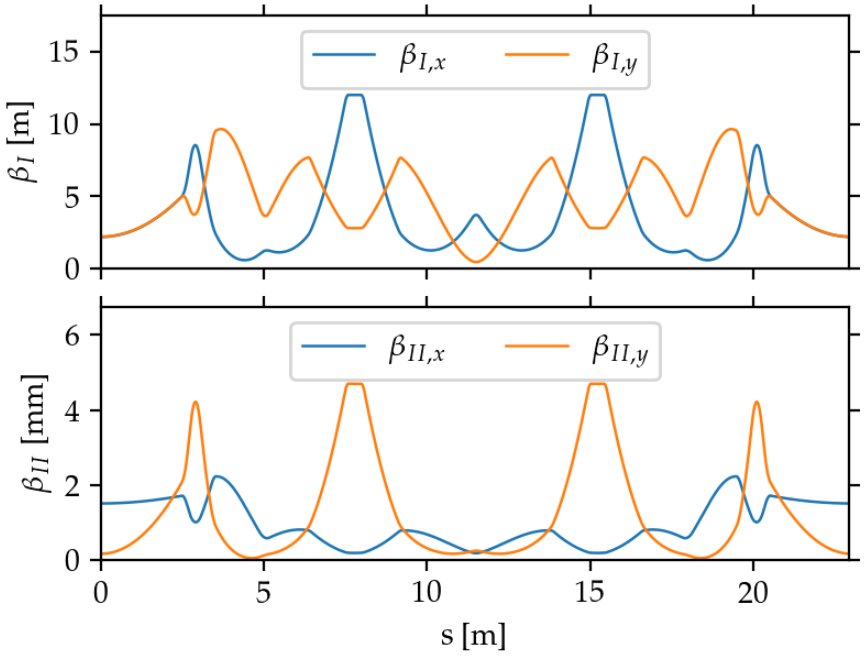

Figure 2.5: Exemplary coupled optics with skew quadrupole components in the first quadrupole triplet of the H6BA. Calculation performed with MADX [34]. Note that β_I is close to the nominal optics functions of the uncoupled case shown in figure 2.2. The β_{II} resemble β_I by exchanging the planes. Notice the vertical axis unit, which is in millimeters.

where the dynamics are considered for on-momentum particles. $K_s = K_s(s)$ is the skew quadrupole component and $S = S(s)$ the solenoidal component in the lattice. Solenoid components are usually not found in modern synchrotron light sources, but are important for collider interaction points. The parametrization of this dynamics is attributed to G. Ripken [56], D. Edwards and L. Teng [57]. Uncoupled motion is associated with two independent motion modes (simply horizontal and vertical motion given by equation 2.2). However for lattices where solenoidal or skew components are substancial, the transversal motion is coupled. The main results of these studies can be summarized as following: the parametrization of the transversal coupled betatron motion gives rise to four modes. These are expressed such that one can associate four β-functions to the motion $(\beta_{x,I}, \beta_{x,II}, \beta_{y,I}, \beta_{x,II})$. The motion is then given by [58]

$$\begin{aligned} x(s) &= \sqrt{\epsilon_{I,x}\beta_{I,x}}\cos\left(\psi_{I,x} + \psi_{I,0,x}\right) + \sqrt{\epsilon_{II,x}\beta_{II,x}}\cos\left(\psi_{II,x} + \psi_{II,0,x}\right) \\ y(s) &= \sqrt{\epsilon_{I,y}\beta_{I,y}}\cos\left(\psi_{I,y} + \psi_{I,0,y}\right) + \sqrt{\epsilon_{II,y}\beta_{II,y}}\cos\left(\psi_{II,y} + \psi_{II,0,y}\right). \end{aligned} \tag{2.40}$$

Analogous to the uncoupled motion, there are associated phase advances ψ. The free parameters $(\epsilon_{I,II,x,y}, \psi_{I,II,0,x,y})$ are defined correspondingly from initial conditions. These optical functions are to be computed numerically and directly dependent on the distribution of skew and solenoid components in the accelerator. Note that the coupled dynamics also give rise to coupled dispersion modes. Therefore the equilibrium emittances have to be recomputed in terms of coupled lattice modes. This calculation has been performed and can be found e.g. in [59]. An example of coupled optical functions are displayed in figure 2.5. Note that the y-axis of the lower panel is in mm. Although the general case has been studied,

the expressions for equilibrium emittances can be significantly simplified when the machine is operated near the coupling resonance. For sake of simplicity only this case is considered.

Coupling resonance
In order to study the coupling resonance the simplification and assumption $S(s) = 0$ is made, hence the coupled EQoM reads

$$\begin{aligned} x'' + K_x x &= -K_s y, \\ y'' + K_y y &= -K_s x. \end{aligned} \tag{2.41}$$

Following Guinard the corresponding Hamiltonian that governs the EQoM reads [59]

$$H = H_0 + H_1 \tag{2.42}$$

with

$$H_0 = \frac{1}{2}\left(K_x x^2 + K_y y^2 + p_x^2 + p_y^2\right), \qquad H_1 = K_S x y. \tag{2.43}$$

Applying perturbation theory, truncating to low-frequency terms and decomposing H_1 in a so-called resonance basis *á la Guinard* yields for the perturbation term

$$H_1 = \sqrt{J_x J_y}\left(h_{1001} e^{i[\psi_{x,0} - \psi_{y,0} + (Q_x - Q_y)s/R]} + c.c. + h_{1010} e^{i[\psi_{x,0} + \psi_{y,0} + (Q_x + Q_y)s/R]} + c.c.\right). \tag{2.44}$$

Here R is the average radius of the machine and $c.c.$ stands for complex conjugate. The actions $J_{x,y}$ are given by equation 2.8 and the resonance driving terms read [59]

$$\begin{aligned} h_{1001} &= \frac{1}{2\pi R}\int_0^{2\pi} \mathrm{d}\theta \sqrt{\beta_x \beta_y} K_s e^{i\left[(\psi_x - \psi_y) - (Q_x - Q_y - p)\theta\right]} \\ h_{1010} &= \frac{1}{2\pi R}\int_0^{2\pi} \mathrm{d}\theta \sqrt{\beta_x \beta_y} K_s e^{i\left[(\psi_x + \psi_y) - (Q_x + Q_y - p)\theta\right]}, \end{aligned} \tag{2.45}$$

where p represents an integer such that $Q_x - Q_y - p = 0$ for h_{1001} or $Q_x + Q_y - p = 0$ for h_{1010}. With these results one can extend the analysis and generalize the expected equilibrium emittances. In the following the discussion is restrained to the results for the case where the difference resonance is excited. The difference resonance, also referred to as the coupling resonance is excited when the transversal fractional tunes fulfill the condition [58]

$$\Delta = q_x - q_y = 0. \tag{2.46}$$

In this case the ratio of the transversal emittances is given by

$$\frac{\epsilon_y}{\epsilon_x} = \frac{\kappa^2}{\kappa^2 + \Delta^2}, \tag{2.47}$$

where the integrated coupling resonance driving term κ is given by

$$\kappa = 2|h_{1001}|. \tag{2.48}$$

Here following approximations have been made: the vertical dispersion is negligible and the perturbed optics are close to the unperturbed ones ($\beta_{II,x} = \beta_{II,y} \approx 0$). Under these approximations, one can show that for $\Delta = 0$ [60]

$$\epsilon_x = \epsilon_y = \frac{\epsilon_{0,x}}{1 + 1/j_x}. \tag{2.49}$$

Therefore the excitation of the coupling resonance allows for a practical implementation and control of different emittance ratios. In general κ is unknown for a real machine, but determined by magnet misalignment errors. This term can be either extracted from equation 2.47, after the tunes have been measured or by more sophisicated techniques, e.g. the closest tune approach [61]. In third and fourth-generation synchrotron light sources dedicated skew quadrupoles are intentionally introduced to correct the integrated resonance driving term. Finally full control of the emittance ratio is given by control of the fractional tune values $q_{x,y}$, which is in general possible by control of quadrupole strengths.

2.5. Collective phenomena

In this section some of the most relevant effects that can affect the performance of the machine are recompiled. These effects are directly related to collective phenomena, namely, they arise due to the mere number of charged particles in the beam. The topics discussed above only consider single particle dynamics, where the transversal and longitudinal motion are only dictated by the storage ring lattice elements. Here this dynamics is assumed and extended to account for multiple particles. Only the results of a selected subset of these collective phenomena are collected and reviewed. A more thorough compilation can be found e.g. in [62, 63].

2.5.1. Touschek scattering

Once one considers multiple particles in a bunch, then the first effect that is discussed is a special case of Coulomb scattering of two particles. A scattering event between two particles, where the particles acquire an energy deviation high enough to lead to particle loss is referred to as Touschek scattering, after the Austrian physicist Bruno Touschek. The scattering event is illustrated in figure 2.6. This effect was first observed in the Frascatti electron-positron storage ring [64]. The rigorous description of Touschek scattering together with intra-beam scattering lead to the Wilson prize recognition in 2018 [65].

The available formulas found in standard literature [30, 31, 32] for the computation of the Touschek lifetime typically assume a flat beam, hence the consequences of increasing the vertical emittance cannot be properly assessed. Fortunately more general formulas derived by Anton Piwinski are available. The derivation is quite lengthy, but in summary the beam lifetime due to Touschek scattering[2] is given by Piwinski's formulae [66]

$$\frac{1}{\tau_{\mathrm{LT}}} = \frac{r_e^2 N_p}{8\sqrt{\pi}\gamma_r^2 T_{\mathrm{rev}}} \int_{s_0}^{s_0+C} \mathrm{d}s \frac{F(\tau_m, B_1, B_2)}{\sigma_z \sqrt{\sigma_x^2\sigma_y^2 - \sigma_\delta^4 D_x^2 D_y^2}}, \tag{2.50}$$

[2] A. Piwinski computes the time it takes for the particle count to be reduced by a factor two.

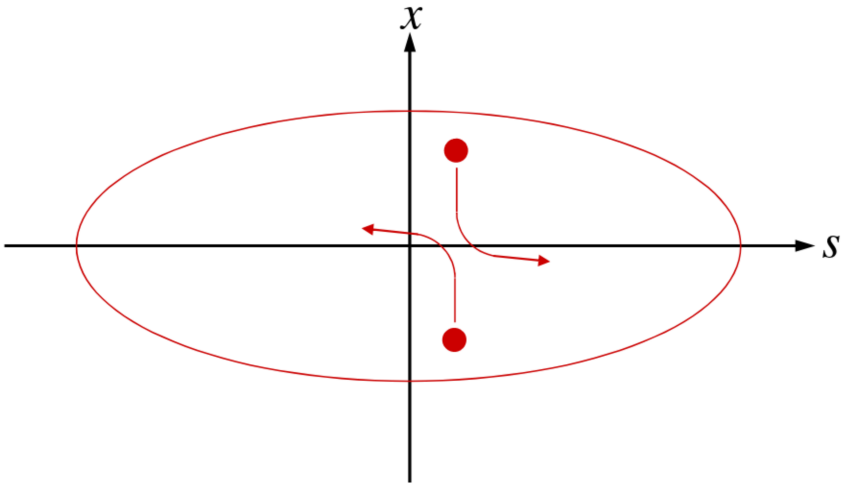

Figure 2.6: Cartoonish depiction of a Touschek scattering event. All the transversal momentum is transfered to the longitudinal plane. This leads to a pair of scattering particles to go beyond the local momentum acceptance and get finally lost. Picture taken from Andy Wolski's lectures at the International Accelerator School for Linear Colliders `https://agenda.linearcollider.org/event/3475/contributions/`

$$F(\tau_m, B_1, B_2) = \sqrt{(B_1^2 - B_2^2)} \times G(\tau_m, B_1, B_2), \tag{2.51}$$

and

$$G(\tau_m, B_1, B_2) = \int_{\tau_m}^{\infty} \mathrm{d}\tau \left[\left(2 + \frac{1}{\tau}\right)^2 \left(\frac{\tau/\tau_m}{1+\tau} - 1\right) + 1 - \sqrt{\frac{1+\tau}{\tau/\tau_m}} - \frac{1}{2\tau}\left(4 + \frac{1}{\tau}\right) \ln \frac{\tau/\tau_m}{1+\tau} \right] \frac{e^{-B_1\tau} I_0(B_2\tau)\sqrt{\tau}}{\sqrt{1+\tau}}. \tag{2.52}$$

Here r_e represents the classical electron radius, T_{rev} the revolution time and I_0 the modified Bessel function of first kind. The quantities in equations 2.50 and 2.52 are defined as follows

$$\frac{1}{\sigma_h^2} = \frac{1}{\sigma_\delta^2} + \frac{D_x^2 + \tilde{D}_x^2}{\epsilon_x \beta_x} + \frac{D_y^2 + \tilde{D}_y^2}{\epsilon_y \beta_y}, \tag{2.53}$$

$$B_1 = \frac{1}{2(\beta_r \gamma_r)^2} \sum_{i \in [x,y]} \frac{\beta_i}{\epsilon_i} \left(1 - \frac{\tilde{D}_i^2 \sigma_h^2}{\beta_i \epsilon_i}\right), \tag{2.54}$$

$$B_2^2 = B_1^2 - \left(\frac{\sigma_h}{(\beta_r\gamma_r)^2 \epsilon_x \epsilon_y \sigma_\delta}\right)^2 \left([\sigma_x \sigma_y]^2 - [\sigma_\delta^2 D_x D_y]^2\right), \tag{2.55}$$

$$\tag{2.56}$$

and

$$\tilde{D} = \alpha D + \beta D_p, \tag{2.57}$$

$$\tau_m = \beta_r^2 \delta_m^2, \tag{2.58}$$

where δ_m represents the maximum momentum deviation the dynamics allow before a particle gets lost. This parameter is referred to as the local momentum acceptance (LMA)

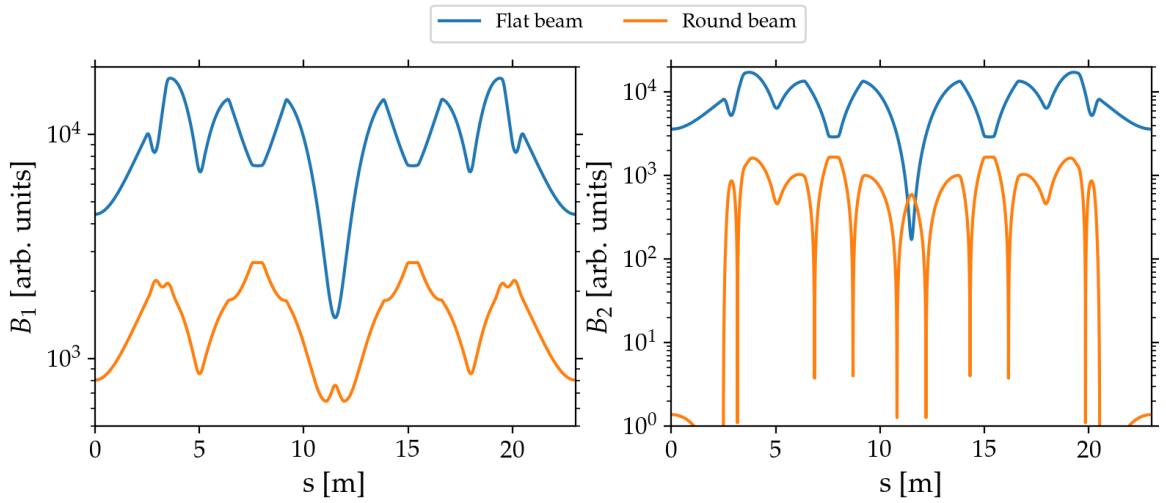

Figure 2.7: Comparison of B_1 and B_2 parameters from Piwinski's formulae for round and flat beam configurations. For this calculation the flat beam configuration had $\epsilon_y = 0.1\epsilon_x$. For both flat and round beams the values $\sigma_\delta = 10^{-3}$ and $\epsilon_x = 20$ pm rad are used. The optical functions for the hybrid six-bend achromat are assumed and illustrated in figure 2.2. A 6 GeV electron beam is assumed as well.

and is normally recovered from tracking simulations. Further these formulae are applicable for unpolarized electron beams. A recent study extends to the case where polarization is non-negligible [67].

To simplify and illustrate the flat and round beam case, some usual approximations are made. First the ultra-relativistic case such that $\beta_r \approx 1$ is assumed and for simplicity the case where $D_y = D_{py} \approx 0$ as well. Then equation 2.50 simplifies to

$$\frac{1}{\tau_{\mathrm{TL}}} = A \int_{s_0}^{s_0+C} \mathrm{d}s \frac{G(\tau_m, B_1, B_2)}{\sqrt{1 + \frac{\sigma_\delta^2 (D_x^2 + \tilde{D}_x^2)}{\epsilon_x \beta_x}}} = A \times I_{\mathrm{Piw.}} \tag{2.59}$$

with

$$A = \frac{r_e^2 N_p}{8\sqrt{\pi}\gamma_r^4 T_{\mathrm{rev}} \sigma_z \epsilon_x \epsilon_y}. \tag{2.60}$$

To compare the round and the flat beam configurations, first flat beam operation is defined when $\epsilon_y = 0.1\epsilon_x$. Further an rms momentum deviaton σ_δ of 10^{-3} is assumed. With these assumptions the Piwinski's B_1 and B_2 parameters can be calculated. An example using the optical functions of the hybrid six-bend achromat (figure 2.2) are shown in figure 2.7. The parameters B_1 and B_2 follow the trend of the optical β-functions. For the flat beam the vertical influence is more pronounced, whereas for the round beam the trend is mixed between both planes.

Next, the integral $G(\tau_m, B_1, B_2)$ described by equation 2.52 is considered. This is depicted in figure 2.8. In the left panel the dependency on δ_m with fixed (B_1, B_2) can be appreciated. The value of the integral drops faster than exponential for high values of δ_m. The expected minimum local momemtum acceptance (LMA) for the H6BA is approximately 3.5%. On the

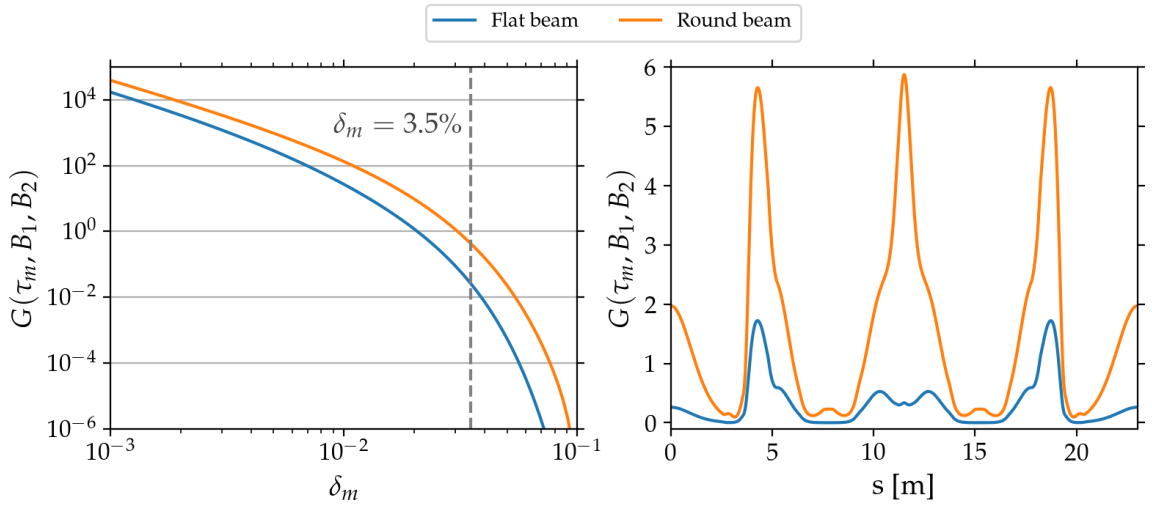

Figure 2.8: Comparison of the integral G from Piwinski's formulae described by equation 2.52 for round beam and flat beam configurations. On the left panel the parameters $(B_1, B_2) = (\langle B_1 \rangle, \langle B_2 \rangle)$ are fixed to the average from the values shown in figure 2.7. On the right panel δ_m was fixed to 3.5%. The same values used for the calculation of parameters B_1, B_2 (figure 2.7) are assumed.

right panel of figure 2.8 the value of G can be appreciated. In both panels one notices that the round beam case yields higher values. This is directly related with the lower values of B_1 and B_2, which weight the integral exponentially (see equation 2.52).

With these results one can numerically evaluate the expected Touschek lifetime. Some lifetime calculation results will be presented in Chapter 3. Here the expected lifetime ratio from both flat and round beam configurations is considered. This is given by

$$\frac{\tau_{\text{round}}}{\tau_{\text{flat}}} = \frac{1}{R_{\text{flat}}} \frac{I_{\text{Piw., flat}}}{I_{\text{Piw., round}}}, \qquad R_{\text{flat}} = \frac{\epsilon_y}{\epsilon_x} = 0.1, \tag{2.61}$$

since $R_{\text{round}} = 1$ and can be obtained by making use of $\epsilon_y = R\epsilon_x$. Considering the values shown in figure 2.8 on the right panel one can observe that $I_{\text{Piw., flat}} < I_{\text{Piw., round}}$. From this perspective there is still no evident lifetime gain. Considering their numerical values yield $I_{\text{Piw., round}} \approx 15.69\,\text{m}$ and $I_{\text{Piw., flat}} \approx 3.04\,\text{m}$. Plugging them into equation 2.61 leads to the lifetime gain of

$$\tau_{\text{round}} \approx 2\tau_{\text{flat}}.$$

This result in fact is the same value that Piwinski reports [66].

2.5.2. Intra-beam scattering

In the previous section only scattering events that lead to particle loss were considered. Of great importance is the consideration of multiple Coulomb scattering events. This phenomenon has been quantified by Anton Piwinski [68], James Björken and Sekazi Mtingwa [69]. Their studies were later extended by multiple authors (e.g. [70, 71]). The conclusion is that multiple interactions lead to an increase of the overall emittance of the beam and are characterized by an emittance growth rate for each motion plane. In the following the most recent results of

the intra-beam scattering (IBS) emittance growth rates are summarized, referred to as the completely integrated modified Piwinski (CIMP) formulae. The emittance growth rates due to intra-beam scattering events (approximately) read [72]

$$\frac{1}{T_{\delta,\text{ibs}}} = \frac{A}{2\sigma_\delta}\int_{s_0}^{s_0+C} \mathrm{d}s \frac{\sigma_H^2}{\sigma_\delta^2}\left(\frac{\log(\frac{q}{a_x})g(\frac{a_y}{a_x})}{a_x} + \frac{\log(\frac{q}{a_y})g(\frac{a_x}{a_y})}{a_y}\right), \tag{2.62}$$

$$\frac{1}{T_{x,\text{ibs}}} = \frac{A}{2\sigma_\delta}\int_{s_0}^{s_0+C} \mathrm{d}s \left[-a_x \log\left(\frac{q}{a_x}\right) g\left(\frac{a_y}{a_x}\right) + \frac{\mathcal{H}_x\sigma_H^2}{\epsilon_x}\left(\frac{\log(\frac{q}{a_x})g(\frac{a_y}{a_x})}{a_x} + \frac{\log(\frac{q}{a_y})g(\frac{a_y}{a_x})}{a_y}\right)\right], \tag{2.63}$$

$$\frac{1}{T_{y,\text{ibs}}} = \frac{A}{2\sigma_\delta}\int_{s_0}^{s_0+C} \mathrm{d}s \left[-a_y \log\left(\frac{q}{b}\right) g\left(\frac{a_x}{a_y}\right) + \frac{\mathcal{H}_y\sigma_H^2}{\epsilon_y}\left(\frac{\log(\frac{q}{a})g(\frac{a_y}{a_x})}{a_x} + \frac{\log(\frac{q}{b})g(\frac{a_y}{a_x})}{a_y}\right)\right], \tag{2.64}$$

with

$$A = \frac{r_e^2 N}{8\sqrt{\pi}\gamma_r^4 T_{\text{rev}}\epsilon_x\epsilon_y\sigma_z},$$

$$\frac{1}{\sigma_H^2} = \frac{1}{\sigma_\delta^2} + \frac{\mathcal{H}_x}{\epsilon_x} + \frac{\mathcal{H}_y}{\epsilon_y}, \tag{2.65}$$

$$q = \sigma_H\sqrt{\frac{2d}{r_e}}, \tag{2.66}$$

$$a_{x,y} = \frac{\sigma_H}{\gamma_r}\sqrt{\frac{\beta_{x,y}}{\epsilon_{x,y}}}, \tag{2.67}$$

$$\tag{2.68}$$

and [73]

$$g(\omega) = \sqrt{\frac{\pi}{\omega}}\left[P^0_{-1/2}\left(\frac{\omega^2+1}{2\omega}\right) \pm \frac{3}{2}P^{-1}_{-1/2}\left(\frac{\omega^2+1}{2\omega}\right)\right], \tag{2.69}$$

where $P^0_{-1/2}$ and $P^{-1}_{-1/2}$ are the associated Legendre functions given by

$$P^0_{-1/2}(z) = \frac{1}{\pi}\int_0^\pi \mathrm{d}\phi \left(z + \sqrt{z^2-1}\cos\phi\right)^{-1/2}, \tag{2.70}$$

$$P^{-1}_{-1/2}(z) = (z^2-1)^{-1/2}\int_1^z \mathrm{d}\bar{z} P^0_{-1/2}(\bar{z}). \tag{2.71}$$

The approximation holds for ultra-relativistic particles whose probability density function (pdf) is a normal distribution. Making the same assumptions as before, such that flat beam is considered with an emittance ratio $R_{\text{flat}} = \epsilon_y/\epsilon_x = 0.1$ and $R_{\text{round}} = 1$ leads to equation 2.61

$$\frac{T^{(\text{round})}_{i,\text{ibs}}}{T^{(\text{flat})}_{i,\text{ibs}}} = \frac{1}{R_{\text{flat}}}\frac{I^{(\text{flat})}_{i,\text{ibs}}}{I^{(\text{round})}_{i,\text{ibs}}}, \qquad i \in \left[x, y, \delta\right], \tag{2.72}$$

with $I_{i,\mathrm{ibs}}$ given by the integral part of the right hand side of equations 2.62, 2.63 and 2.64. Using for example the optical functions of the hybrid six-bend achromat yields

$$T_{\delta,\mathrm{ibs}}^{(\mathrm{round})} \approx 5T_{\delta,\mathrm{ibs}}^{(\mathrm{flat})}, \qquad T_{x,\mathrm{ibs}}^{(\mathrm{round})} \approx 5T_{x,\mathrm{ibs}}^{(\mathrm{flat})}, \qquad T_{y,\mathrm{ibs}}^{(\mathrm{round})} \approx T_{y,\mathrm{ibs}}^{(\mathrm{flat})}. \tag{2.73}$$

It is less straight forward to make a conclusion out of these estimations, since the equilibrium emittance has to be computed numerically by integrating

$$\frac{\mathrm{d}\epsilon_i}{\mathrm{d}t} = 2\lambda_i(\epsilon_i - \epsilon_{0,i}), \qquad i \in \left[x, y, \delta\right], \tag{2.74}$$

with

$$\lambda_i = \frac{1}{\tau_i} + \frac{1}{T_{i,\mathrm{ibs}}} \tag{2.75}$$

similar to equation 2.18. This exercise is postponed to Chapter 4.

2.5.3. Wakefields and space charge

Although it is not a subject of this thesis, it shall not remain unmentioned the crucial influence of wakefields/impedance and space charge in fourth-generation light sources. The effects of wakefields induced by mirror images in different accelerator components generate a constraint to the achievable current that can be stored. Particles interact with wakes generated by themselves or from other bunches and these interactions can lead to unstable motion. Furthermore, the energy deposited in these wakefields can lead to unacceptable heat load on certain components. Therefore these effects are monitored closely and modeled intensively at all stages of an accelerator design and operation. In electron storage rings, usually the vertical wakes are dominant and determined by impedance generated at insertion devices. Hence the vertical wakes are responsible of the limits in associated figures of merit related to wakefields, e.g. single bunch current thresholds, coupled bunch instabilities growth rates, micro-wave instability threshold, Robinson-instability threshold, etc. An important mitigation mechanism is offered by operating the machine near the coupling resonance, thereby sharing the wake impact on the motion between the two transversal planes [74]. An active investigation on this topic is being currently pursued within the beam dynamics team.

Lastly, the impact of space charge in electron machines has been deemed negligible due to its steep dependence on the inverse of the cubic relativistic factor γ_r^3 [75]. During the course of this thesis it was established that the space charge effect will serve as a mitigation mechanism of collective instabilities due to the tune spread it generates. Our results have been reported in [27]. Unfortunately, a round beam operation also decreases the impact of space charge in the dynamics. It remains an open question, if the benefits of space charge mitigation are considerable when operating the machine with round beams at PETRA IV.

3

PETRA IV beam dynamics

With the theoretical framework established, we now proceed to a detailed description of the beam dynamics in the PETRA IV upgrade project. From this chapter onward, a general remark is made regarding the use of passive voice up to this point. In the following sections, the use of "we" refers to the author and the reader. Contributions from other researchers will be explicitly acknowledged, with proper citations provided where applicable.

3.1. Storage ring

The storage ring is composed of seventy two hybrid six-bend achromat cells (nine cells per arc), four short (approx. 64 m) and four long (approx. 108 m) straight sections. This unusual geometry for a synchrotron light source was inherited from the high energy physics programme and the collider constraints for the tunnel geometry. The circumference of the ring coincides with its predecessor and existing tunnel length. DESY will continue to house the longest synchrotron light source ever conceived. An illustration of a bird-eye view of the storage ring is shown in figure 3.1. The position of the planned photon beamlines are signalized with grey dots. The rest of the cell straigths are signalized by grey rings. These spaces will be either kept empty or damping wigglers will be installed. The damping wigglers will balance the total radiated energy and thus the equilibrium emittance to ~20 pm rad.

Table 3.1: Design parameters of PETRA III and IV for the current and foreseen operation modes. The parameters have been taken from PETRA IV's concept design report [19].

Design parameter	PETRA III		PETRA IV	
Energy [GeV]	6		6	
Circumference [m]	2304		2304	
Operation mode	Continuous	Timing	Brightness	Timing
Emittance (H/V) [pm rad]	1300 / 10		<20 / 4	<50 / 10
Total current [mA]	100		200	80
No. of bunches	960	40	1920	80
Bunch current [mA]	0.1	2.5	0.1	1.0
Bunch separation [ns]	8	192	4/20(gaps)	96

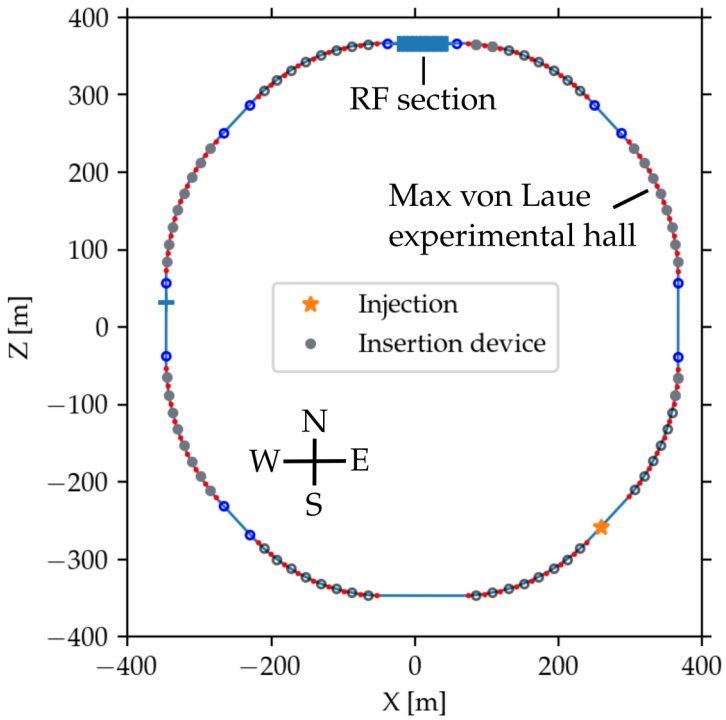

Figure 3.1: Survey plot of PETRA IV storage ring. The location of foreseen insertion devices are indicated with full grey dots. RF sections and the Max von Laue experimental hall are indicated for reference. The injection point is signalized with an orange star in the south-east. The empty grey dots are empty insertion device spaces or damping wigglers. The empty blue dots show possible spaces for longer flagship insertion devices. The red dots indicate the position of the H6BA cells.

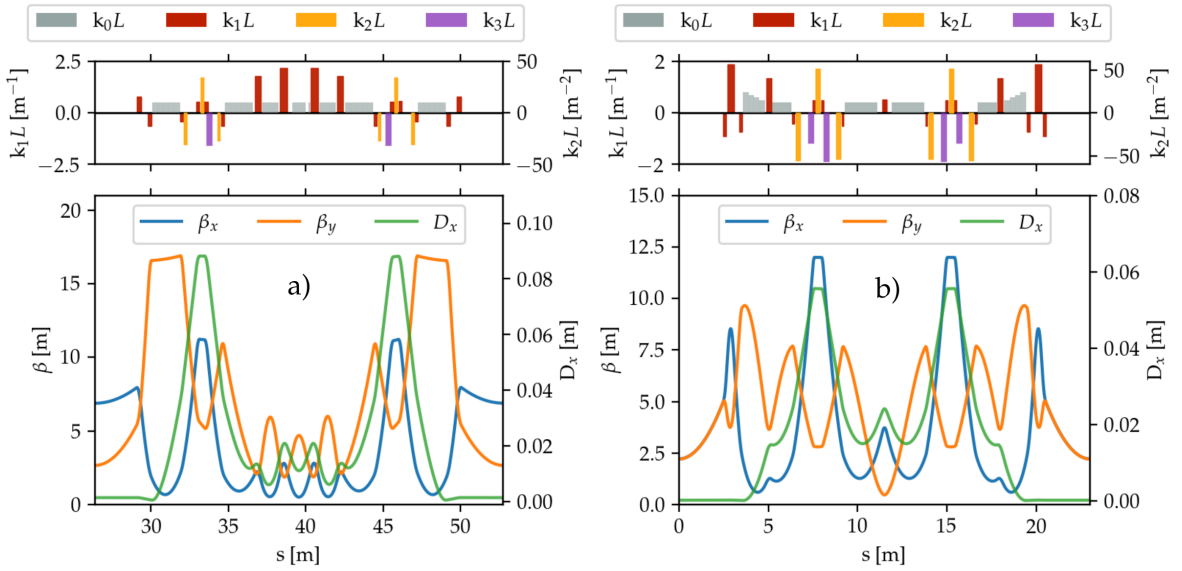

Figure 3.2: Comparison between hybrid multi-bend achromat cells. (a) Left lower panel: the optical functions of the hybrid seven-bend achromat cell are shown. The position of the cell elements are shown in the top panel. The strength of the quadrupoles are shown in red, sextupoles in yellow and octupoles in lila. The position of the bending magnets is illustrated with grey. (b) Same information as in (a) but for the hybrid six-bend achromat. These optical functions are also shown in figure 2.2.

Space for the installation of longer insertion devices, commonly described as DESY's ID flagships, are signalized with blue rings and are located at the start and end of the arcs.

In Table 3.1 a comparison of the design parameters for the current and foreseen operation modes of PETRA III and IV are listed. The machine will be operated with 6 GeV electron beams. Decreasing the energy to 5 GeV has been considered but deemed unsufficient in terms of performance [19]. There will be two main operation modes, a high-brigthness, high-coherence continuous mode and a timining mode with reduced number of bunches but increased single bunch population. These operation modes define the constraints and indirectly the optimization strategies for performance enhancement of the machine.

Achromat cell

Building on the discussion, the design of the achromat cells are revisited. Over the years various designs have been considered for the storage ring [76]. However, at its core the design has always considered the hybrid seven-bend achromat cell. Originally proposed for the upgrade of the European Synchrotron Radiation Facility (ESRF) storage ring in Grenoble, France [77], this cell optics—introduced by Pantaleo Raimondi—has demonstrated multiple advantages [14, 78, 79] over the "pure" multi-bend achromat proposed by Dieter Einfeld, Jan Schaper and Mark Plesko [8]. As a result, it has been adopted in the upgrade designs of several facilities (e.g. [17, 15, 80, 81]). A collaborative effort between DESY and ESRF led to a modified version of this design: the hybrid six-bend achromat, also proposed by P. Raimondi. A comparison between both cell designs is shown in figure 3.2.

One of the main differentiators are the equal β-functions at the insertion device straight.

The ESRF storage ring achieves a natural emittance of (120 ± 8) pm rad and it is therefore still advantageous to operate the machine with flat beams ($\epsilon_y/\epsilon_x \approx 10/120$) and asymmetric β-functions in the cell straight [14, 79]. For PETRA IV the reduction of the equilibrium emittance by a factor of six enables round beam operation, allowing for symmetric β–functions in the cell straight. A more detailed description of the ESRF storage ring is reported in [14, 79].

Meanwhile, recent discussions have focused on the optimal design parameters for fourth-generation light sources. In particular, the discussions on the design of two light sources with comparable circumferences of approximately 2 km are considered [23, 81]. A concept design of a dedicated synchrotron light source inspired by the constraints of the PETRA III tunnel is reported in [82]. The technical design and beam dynamics performance of PETRA IV with realistic constraints, collective beam dynamics and detailed considerations of injection are documented in [23]. The upgrade study for the Stanford synchrotron light source reports similar performance with a storage ring of comparable circumference (2.190 km) [81]. This machine could be installed in the tunnel of the former PEP (Positron-Electron Project) collider. As highlighted in [23, 82], *a-posteriori* specifications that define the beam dynamics performance of a storage ring of this scale can be summarized as follows:

1. Transversal emittances $\epsilon_{x,y}$ in the range of $\leq$10 pm rad to approximately achieve diffraction limited X-rays with $\lambda = 10^{-10}$ m wavelengths and peak brightness in excess of 10^{22} photons mm^{-1} mrad^{-1} at 0.1% bandwidth.
2. Beam lifetime in excess of 10 hours and a transversal dynamic aperture (DA) of ~10×3 mm^2 (H × V at injection point).

These requirements represent a reasonable enhancement compared to the current operations of third-generation light sources and serve as a guideline. A facility like PETRA is well-suited to meet these specifications. The first point concerns the equilibrium emittance ϵ_0 and the desired optics at the insertion device straights. The second point addresses the requirements for the injector chain, particularly the beam quality delivered by the booster synchrotron. A prolonged beam lifetime is also desirable from the perspective of photon users, as injection events are expected to cause disturbances. Additionally, a large dynamic aperture facilitates both the accumulation and charge top-up processes.

The design of the PETRA IV storage ring has been frozen by the time of writing of this thesis. The optical functions of the ring are shown in figure 3.3. The northernmost rf long straight section is signalized in the upper panel. Relevant beam and operation parameters are listed in table 3.2.

Beam dynamics performance (a summary)

The beam dynamics performance of a storage ring is assessed using a set of figures of merit that align optimally with the specified requirements. Key metrics include injection efficiency, beam lifetime, single- and multi-bunch current intensity thresholds, and electron beam characteristics. A common proxy for evaluating injection efficiency is the computation of the dynamic aperture, which is typically emphasized in design reports. Beam lifetime is often associated with the Touschek lifetime and, therefore, linked to the machine's local momentum acceptance, making it a crucial parameter in evaluating overall performance. In beam dynamics performance studies, magnet and girder misalignments must be considered. The fourth-generation of synchrotron light sources are highly sensitive to these unavoidable technical imperfections, necessitating dedicated correction and commissioning campaigns to

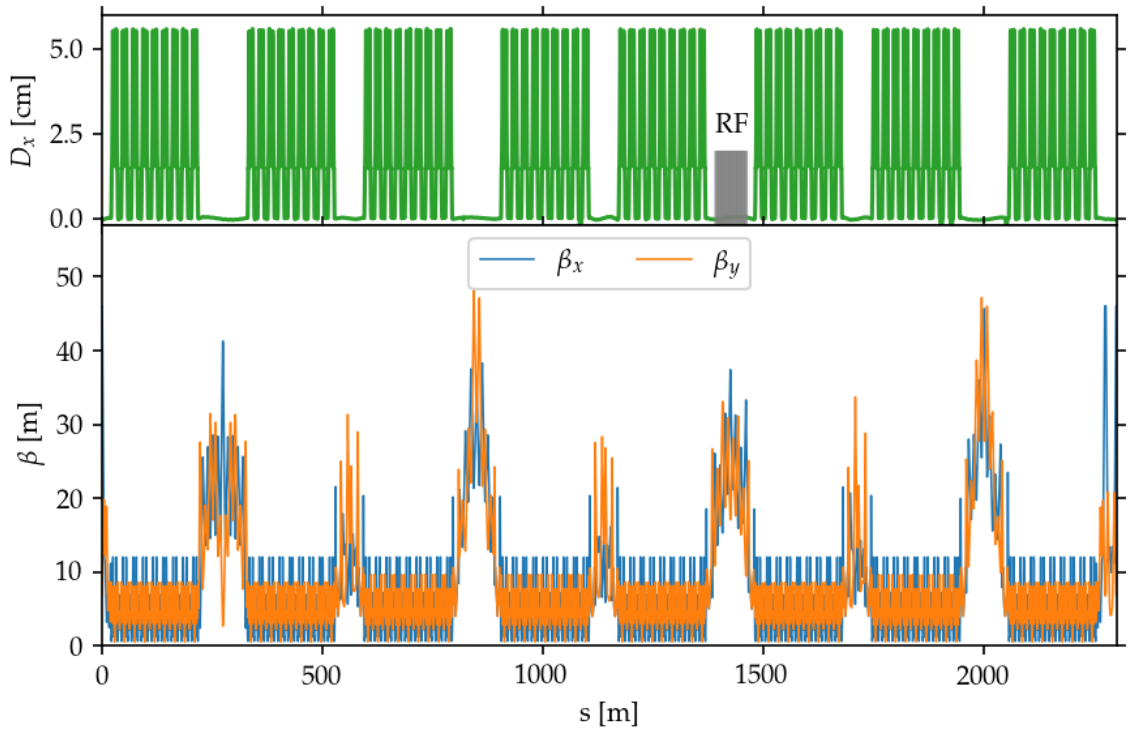

Figure 3.3: Optical functions of PETRA IV. The start $s = 0$ m indicates the injection point signalized with an orange star in figure 3.1. The rf long straight section is marked in the upper panel.

Table 3.2: Parameters of the H6BA lattice for the baseline operation. The parameters consider the use of damping wigglers (DW) to balance the emittance to the listed value.

Parameter	Value
Tunes Q_x,Q_y	135.18, 86.27
Natural chromaticity ξ_x,ξ_y	-232, -156
Corrected chromaticity ξ_x,ξ_y	8.1, 7.3
Momentum compaction factor α_C	3.3×10^{-5}
Standard ID space	4.9 m
$\beta_{x,y}$ at ID, standard cell	2.2 m, 2.2 m
Natural emittance $\varepsilon_{0,x}$	20 pm rad
Rel. energy spread δ_E	0.9×10^{-3}
Energy loss per turn	4.0 MeV
Damping time $\tau_{x,y,z}$ [ms]	18, 22.5, 12.9
Partition number $j_{x,y,z}$	1.25, 1, 1.75

optimize the machine's operation [83, 84]. To quantify the machine imperfections impact on the optics the rms β-beating is used. Along this thesis we define the β-beating as

$$\beta\text{-beating} = \sqrt{\left(\frac{\beta_x - \beta_{x,0}}{\beta_{x,0}}\right)^2 + \left(\frac{\beta_y - \beta_{y,0}}{\beta_{y,0}}\right)^2}, \tag{3.1}$$

where the unpertubed or perfect machine optics $(\beta_{x,0}, \beta_{y,0})$ are used as reference. In the following we might refer to the rms β-beating only as the β-beating.

Although a full commisioning chain is necessary to reduce the rms β-beating to a few percent, many of the beam dynamics simulations studies rely on a reduced set of aligment errors that effectively induce a conservative 3 to 5% rms β-beating. This approach has shown to be equivalent to carrying out the full start up and tuning procedure with the complete set of misalignments reported in [83, 84]. State-of-the-art machines such as the one at ESRF have achieved an rms β-beating of 1.5% [14]. Further, the baseline parameters for the chromaticity and octupole settings have been established after a multi-objective optimization campaign involving the dynamic aperture (DA) and the local momentum acceptance (LMA) [23].

With these considerations in mind, the first point of the list of specifications can be reached if the natural emittance is shared between transverse planes. Regarding the second point some challenges and cures have been already encountered. We would like to discuss in detail the dynamic aperture, machine protection, collimation strategy and injection efficiency. The rest of the figures of merit such as beam lifetime and the electron beam parameters will only be summarized in this chapter.

Dynamic aperture

To begin the dynamic aperture is considered as it is independent of the electron beam properties. We refer to dynamic aperture as the set of coordinates, where the edge between bounded and unbounded motion is found. The practical way to compute the dynamic aperture is with element-by-element tracking of particles with different initial transversal amplitudes. For electron machines tracking for a few synchrotron radiation damping times should allow the determination of stable or unstable motion. The initial transversal amplitude can be varied and the edge at which particles go from stable to unstable motion is referred to as dynamic aperture. The current lattice design enables a dynamic aperture of approximately $10{\times}3\,\mathrm{mm}^2$ (H×V) with optimized octupole and sextupoles settings compared to the previous lattice designs with $3{\times}1\,\mathrm{mm}^2$ [76]. These values are obtained including the physical aperture limitations. The dynamic aperture calculation is illustrated in figure 3.4. Different machine realizations with an average rms β-beating of 3% are shown. With the enhanced dynamic aperture (DA), off-axis injection becomes feasible. However, various injection scenarios have also been considered to ensure flexibility in case the available DA is significantly lower than anticipated [85].

Finally, the dynamic aperture is limited by the crossing of the half-integer resonance in the horizontal plane and the integer resonance in the vertical plane, both induced by amplitude detuning. This is better illustrated in figure 3.5, where the amplitude dependent tunes are shown. The tunes dependency on the horizontal action J_x can be modeled with a polynomial function. Under this premise the tunes with amplitude dependency read

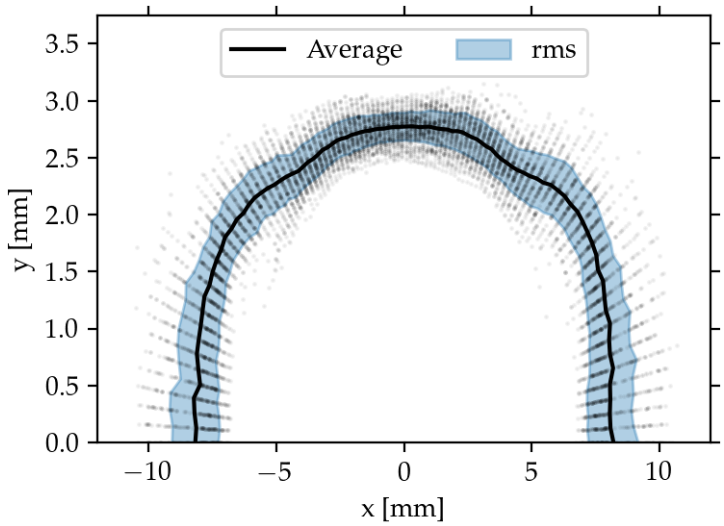

Figure 3.4: Dynamic aperture of the storage ring at injection. Hundred error seeds have been used to generate an rms β-beating $\approx 3\%$. The single seed values are shown as dots. The average and rms values are displayed as a black solid curve and a blue shaded area respectively. The optical functions at observation point are $(\beta_x, \beta_y) = (46\,\text{m}, 7\,\text{m})$ with vanishing $\alpha_x = \alpha_y = 0$. These values correspond to $s = 0$ m, i.e. the injection point. The tracking simulation includes synchrotron radiation damping, quantum excitation and third harmonic cavity system. The aperture model is included as well (see next subsection).

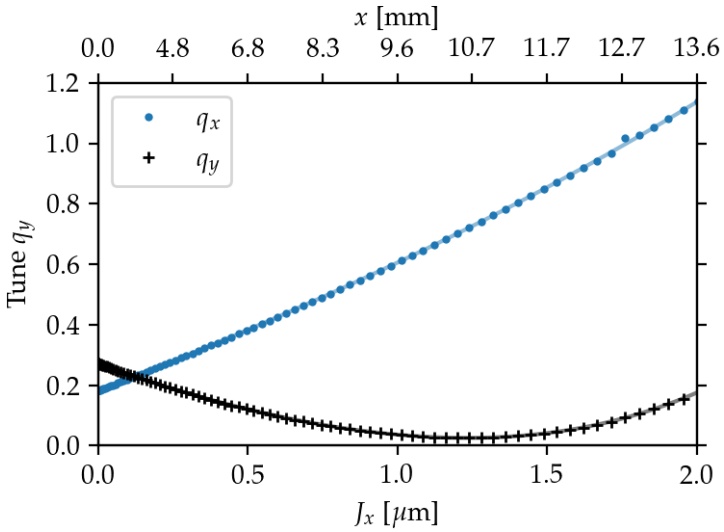

Figure 3.5: Detuning with horizontal amplitude in PETRA IV. On the top axis the corresponding amplitude at injection is shown $(\beta_x, \alpha_x) = (46\text{m}, 0)$. Note that at approximately 8.3 mm the half order resonance is crossed by q_x and the vertical tune approaches the integer resonance. This is in fact the dynamic aperture limitation illustrated in figure 3.4.

Table 3.3: Amplitude dependent coefficients of polynomial model.

Coefficients	Horizontal	Vertical
κ [μm^{-1}]	0.390	-0.358
$\kappa^{(2)}$ [μm^{-2}]	0.027	0.113
$\kappa^{(3)}$ [μm^{-3}]	0.009	0
$\kappa^{(4)}$ [μm^{-4}]	0	0.011

$$q_x = q_{x,0} + \kappa_x J_x + \kappa_x^{(2)} J_x^2 + \kappa_x^{(3)} J_x^3, \tag{3.2}$$

$$q_y = q_{y,0} + \kappa_y J_x + \kappa_y^{(2)} J_x^2 + \kappa_y^{(4)} J_x^4. \tag{3.3}$$

The coefficients $\kappa_{x,y}^{(n)}$ are determined with a least-squares difference fit and listed in Table 3.3. This dependency restricts the horizontal motion to actions in the range of $J_x < 0.75\,\mu m$. The stored beam with an emittance of 20 pm won't be affected by amplitude detuning.

Machine protection and collimation strategy

During this thesis, a new collimation strategy was developed to enhance machine protection[1]. The collimator system must be designed to capture and intercept particle losses and hence protect sensitive equipment; special attention is given to in-vacuum insertion devices that can suffer from radiation damage. The primary sources of particle losses are expected to be Touschek scattering and beam interactions with residual gas particles. Additionally, the collimation system is designed to serve as an emergency beam dump. Particles injected significantly outside the dynamic aperture should also be captured by the collimator jaws. The positions of the collimators, the aperture model, and an example loss map for injected particles are presented in figure 3.6.

The former collimation strategy reported in [86] achieved insufficient collimation capture efficiency of 65% of scattered particles. The new design [23] achieves a collimation capture efficiency of up to 90%. This strategy entails repositioning the four horizontal collimators within the arc cells to align with the position of an octupole, which is then removed. To compensate, the strengths of the remaining octupoles are increased, preserving the overall integrated octupole strength. While this approach maintains the amplitude detuning of the transverse dynamics, it also enhances parametric resonances, which adversely affect the dynamic aperture. To evaluate the impact of this modification, a frequency map analysis is performed. Particles are tracked for a total of 1024 turns over a grid (150×150) in configuration space from $x \in [-20\text{mm}, 20\text{mm}]$ and $y \in [0\text{mm}, 3\text{mm}]$. The tracking data is divided in two halves, whose tune value is later compared. With this information a tune diffusion is recovered. This analysis is commonly known as a frequency map [87]. The results are shown in figure 3.7. Tracking is performed with `ELEGANT` [88]. In the simulations particles are tracked element-by-element neglecting synchrotron radiation, quantum excitation and misalignment errors. The longitudinal coordinates are frozen to zero.

The average dynamic aperture including error misaligments yield the same results as in figure 3.4. From this perspective the dynamics has not been spoiled. It is evident that particles

[1] by L. Malina

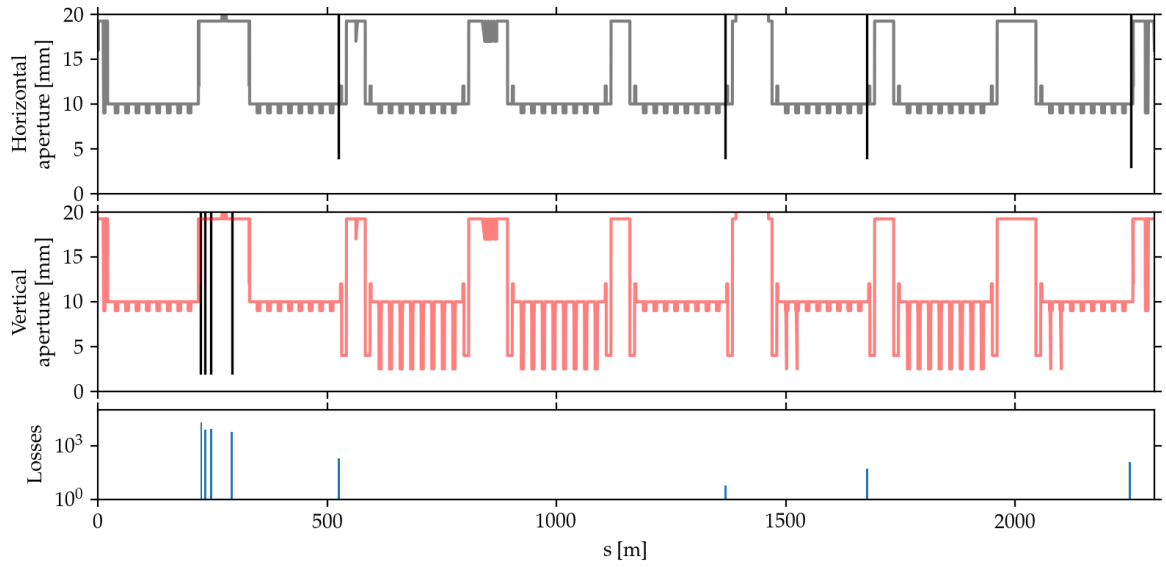

Figure 3.6: Transversal aperture model of the storage ring. The location of horizontal and vertical collimators is indicated with thick black lines. Vertical collimators are installed in a long straight section, whereas horizontal collimators are installed in four arc cells. An exemplary loss map of injected particles intercepted by the collimators is shown in the lowest panel.

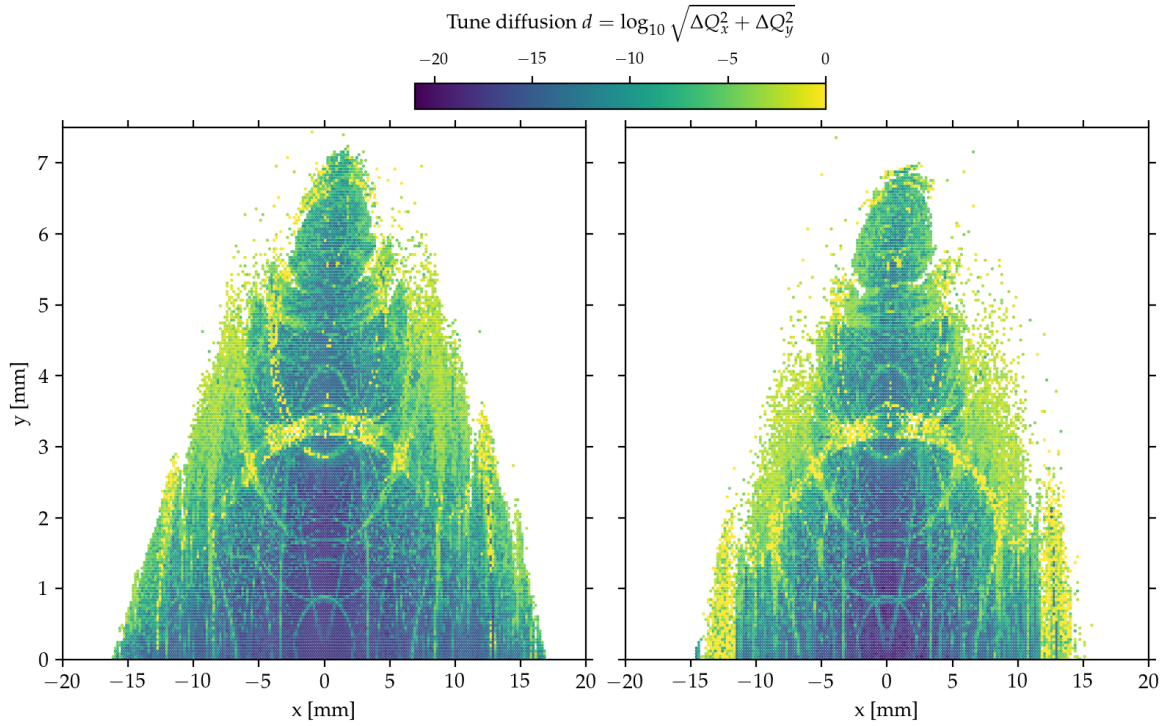

Figure 3.7: Comparison of a frequency map analysis of a baseline PETRA IV storage ring (left) and a ring with four octupoles removed to free space for collimators (right). Synchrotron radiation and quantum excitation are excluded in the tracking. No misaligments are considered in these simulations and the longitudinal coordinates are frozen to zero. The observation point is the injection straight starting point (s=0 m) with $(\beta_x, \beta_y) = (46\,\text{m}, 7\,\text{m})$ and vanishing $\alpha_x = \alpha_y = 0$.

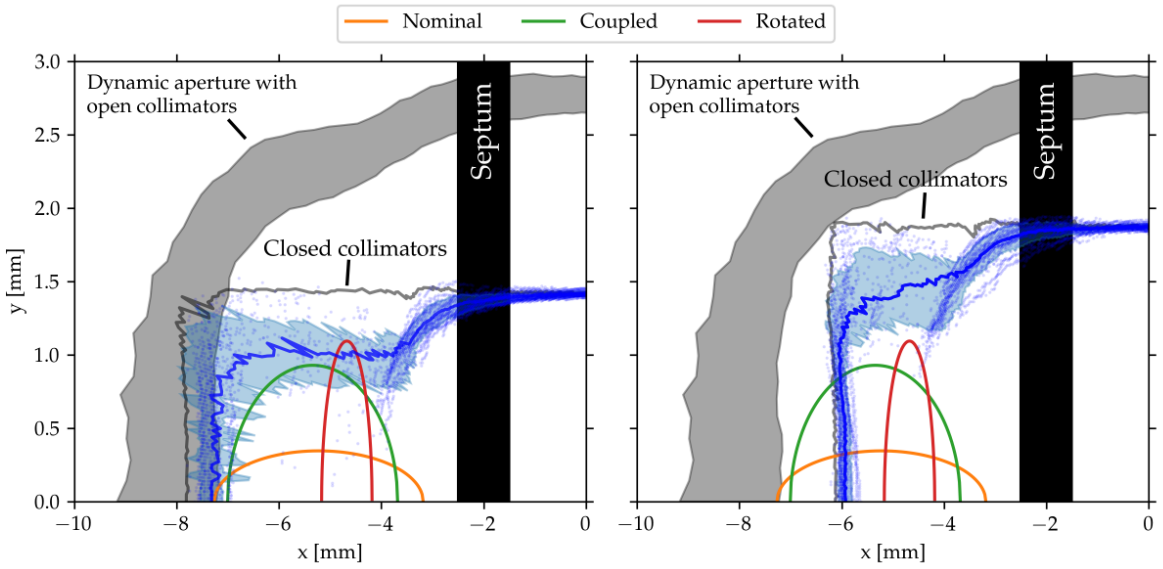

Figure 3.8: Dynamic aperture with closed collimators and misalignment errors. The uppermost shaded grey area indicates the rms dynamic aperture shown in figure 3.4. Three rms beam sizes are shown for the nominal, rotated and coupled injected beam scenarios. Left: the horizontal collimators have been closed to 4 mm and vertical to 3 mm (half-gap). Right: the horizontal collimators have been closed to 3 mm and vertical to 4 mm (half-gap). The transparent blue dots illustrate thirty misalignment error seeds. The solid blue curve and shaded blue area indicate the average and rms aperture respectively. The ideal aperture limitation due to collimators is shown as well as a solid grey curve.

with initial horizontal amplitudes beyond 10 mm will likely get lost, unless the machine can be corrected and commissioned to achieve a β-beating of less than 3% and a scheme is applied to cross or avoid half integer resonances.

Injection efficiency

As part of this thesis and complementary to the study of the collimation strategy the injection efficiency has been evaluated. Previous assessments of injection efficiency [85] did not account for any collimation strategy. To evaluate injection efficiency, it is sufficient to determine the dynamic aperture and verify that the injected beam fits within. As highlighted in [85], an increase in rms β-beating reduces the dynamic aperture, thereby lowering injection efficiency. To address this, two beam manipulation techniques have been previously proposed to ensure the injected beam fits within the available dynamic aperture [85].

The first strategy makes use of the emittance sharing mechanism to equalize the transversal emittances to $\epsilon_x = \epsilon_y = 13.7\,\text{nm rad}$ (coupled beam) from the incoming beam delivered by the booster. The second strategy involves the complete exchange of emittances such that $\epsilon_x \rightarrow \epsilon_y$ and viceversa (rotated beam). The nominal injected beam is expected to have a natural emittance of 20 nm rad and an emittance ratio of 10% is assumed. The available dynamic aperture with closed collimators for two configurations is shown in figure 3.8. The dynamic aperture with open collimators is shown as well. Depending on the manipulation on the injected beam, the injection efficiency will differ according to the collimator settings. For instance, assuming the beam is completely rotated (red half-ellipse), the injection efficiency will decrease considerably for a collimator setting with closed vertical jaws down to 3 mm

Table 3.4: Parameters of the electron beam for the baseline operation modes of PETRA IV [23]. A third harmonic cavity was used to elongate the beam longitudinally. The vertical emittance was set to 10% of ϵ_x for the intra-beam scattering calculations.

Parameter	Reference	Brightness	Timing
Bunch current [mA]	0.01	0.1	1
Hor. emittance [pm rad]	18	24	37
Bunch length [mm]	11.4	13.9	21
Energy spread	0.90×10^{-3}	0.93×10^{-3}	1.1×10^{-3}

(left panel), whereas for a more relaxed setting the injection efficiency will be in excess of 99%. This is evident from the information shown in figure 3.8. Tracking simulations also confirm this claim. In summary, the injection efficiency will be in excess of 99%, when the collimator settings are paired to the right injected beam scenario.

Electron beam parameters

Next, we discuss the electron beam parameters. Generally, the beam parameters are sensitive to the bunch population and therefore depend on the operation mode. The storage ring is equipped with a third harmonic cavity system to longitudinally enlarge the electron bunches. This technique has been incorporated into the baseline design, as it is a common approach to mitigate density-dependent effects such as intra-beam scattering and particle losses due to Touschek scattering. Recently, the performance and design of one of the considered cavities has been reported in [89]. At zero current, the longitudinal bunch length is $\sigma_z = 2.3\,\mathrm{mm}$, with a single harmonic rf system operating at $f_{\mathrm{rf}} = 500\,\mathrm{MHz}$. With the addition of the third harmonic cavity system ($f_{\mathrm{rf}}^{(\mathrm{harm.})} = 1.5\,\mathrm{GHz}$), the bunch length will be elongated by nearly a factor of five, reaching $\sigma_z = 11.4\,\mathrm{mm}$. Additionally, the longitudinal profile is influenced by elongation due to wakefields. Transversely, the emittances are diffused by intra-beam scattering. Taking these effects into account, the expected beam parameters for the baseline operation modes are summarized in Table 3.4 [23].

Beam lifetime

The beam lifetime is expected to be limited by both residual gas content in the vacuum chamber and Touschek scattering losses. Reduction of the beam lifetime due to scattering with residual gas particles is usually referred to as the vacuum lifetime. For PETRA IV it is expected to be in excess of 50 hours [23] and will be the main lifetime limitation for the brightness mode. In contrast the lifetime when the machine is operated in timing mode will be dominated by Touschek scattered losses. These losses are determined by the quantities described in equation 2.50. One important component of the equation is the local momentum acceptance (LMA). This is illustrated in figure 3.9. The LMA has been calculated with element-by-element tracking simulations including the aperture model. The tracking has been performed with `ELEGANT` and includes the effects of synchrotron radiation, quantum excitation and the third harmonic cavity system. Note that the LMA limit is dominated by the dynamics in the arc cells. The straight section have an ample LMA and therefore contribute less to the loss rate. For the timing mode the Touschek lifetime is expected to be approximately 10 hours and 100 hours for the brightness mode [23]. More conservative figures are considered for the conceptual study reported in [90].

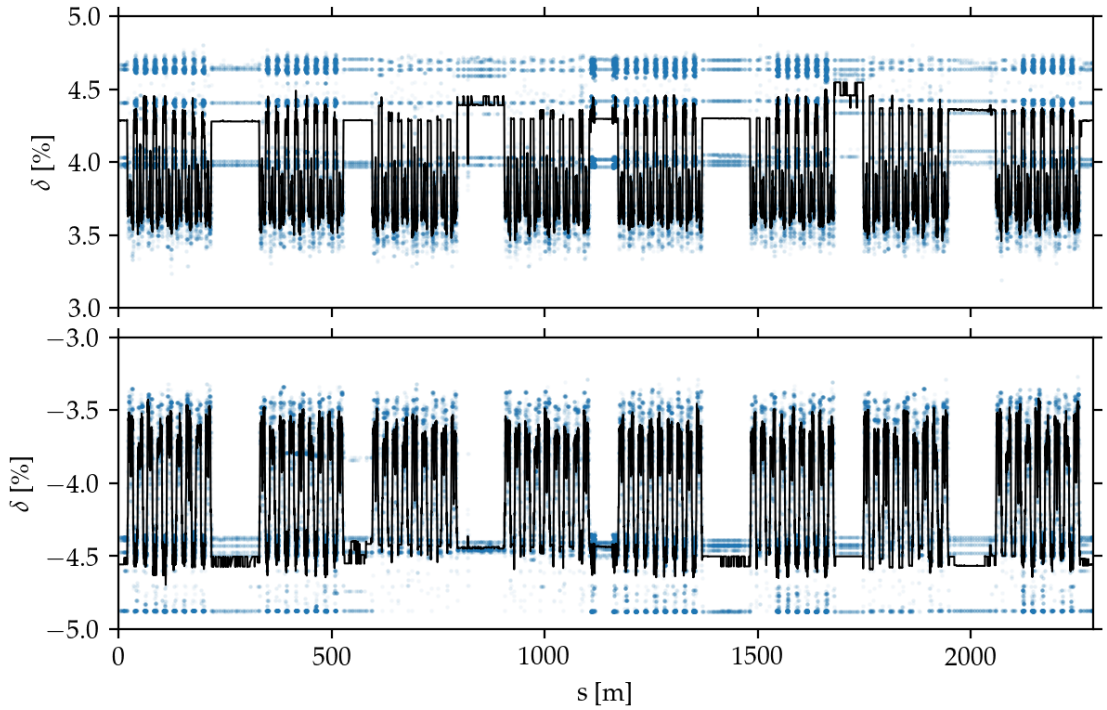

Figure 3.9: Local momentum acceptance of the complete ring. Six misaligment seed values are shown in blue and their corresponding average in black. Notice that the bottleneck of the momentum acceptance is in the arc cells.

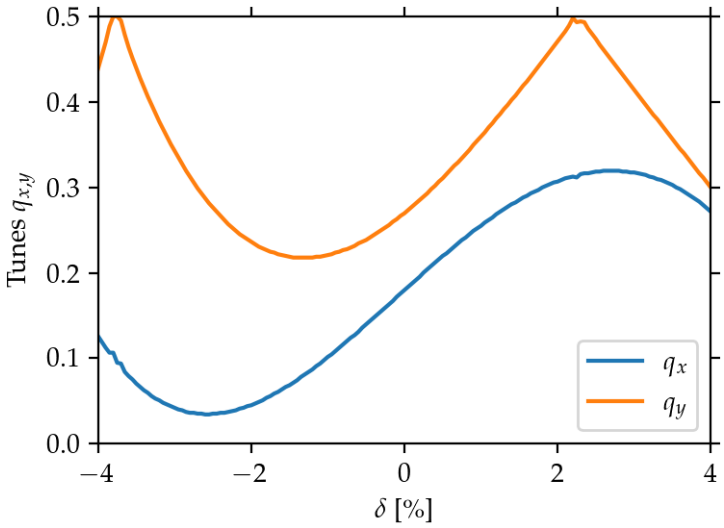

Figure 3.10: Global chromatic detuning calculated at the injection point with $(\beta_x, \beta_y) = (46\,\text{m}, 7\,\text{m})$ and vanishing $\alpha_x = \alpha_y = 0$. The computation is performed with `Xsuite` with element-by-element tracking with the longitudinal coordinates frozen. Third harmonic cavity has been included.

Table 3.5: Nominal parameters of the proposed DESY IV booster ring lattices and equilibrium parameters at extraction energy of 6 GeV.

Parameter	Symbol	6-fold	8-fold
Circumference	C	316.8 m	304.8 m
Tunes	Q_x/Q_y	17.37/12.15	15.19/5.34
Nat. chromaticity	ξ_x/ξ_y	-41.8/-13.8	-18.4/-12.12
Mom. compaction	α_c	3.17×10^{-3}	2.97×10^{-3}
Partition number	$\mathcal{J}_x, \mathcal{J}_y, \mathcal{J}_z$	2.56, 1, 0.44	2.335, 1, 0.665
Natural emittance	ϵ_0	19.1 nm rad	20.8 nm rad
Damping times [ms]	τ_x, τ_y, τ_z	0.8, 1.9, 4.5	0.8, 1.8, 2.75
Rms momentum spread	σ_p	2.64×10^{-3}	2.15×10^{-3}

Related to the LMA and beam lifetime the chromatic detuning for the nominal setup of PETRA IV is shown in figure 3.10. Here the transversal tunes as a function of the momentum deviation are illustrated. Note that although the half integer resonance is reached in the vertical plane around $\delta \approx 2.1\%$, with the effects of synchrotron radiation the resonance does not lead to particle losses. This is better illustrated in figure 3.9, where the LMA is shown.

3.2. Booster ring

The main purpose of the synchrotron booster ring is to deliver full energy electron bunches to the main storage ring. Usually the booster ring receives electron bunches from a linac and accelerates these bunches to its final energy. At DESY the booster ring receives electron bunches from an intermediate particle accumulator named the Positron Intensity Accumulator (PIA) [91]. Today it serves as an electron accumulator but the name remained. The electrons' energies are boosted from 450 MeV to 6 GeV and then delivered to the main storage ring.

The design considerations for the booster ring are primarily driven by the beam dynamics performance of the main storage ring. The most critical figures of merit for the booster ring design are the dynamic aperture and the beam lifetime from the main storage ring. It has been specified that the total stored current in the main ring must not decrease by more than one percent to avoid any significant impact on photon beam brightness. The current decrements have to be ultimately compensated by the booster synchrotron. Depending on the chosen injection scheme, adjustments to the ramping cycle may be required. A detailed description of the initial design proposal for the booster synchrotron can be found in [92].

Its optical functions are illustrated in figure 3.11. Six arc cells composed of a quasi seven-bend achromat cell are the backbone of this synchrotron. The straight sections have been designed to alternate between low- and high-β insertions. Low-β straights are reserved for rf cavities, thereby mitigating the impact of the cavities impedance on the single bunch current limit. The high-β straights would accomodate injection and extraction devices. For this machine, alternative storage ring beam dynamics performance was considered. The main storage ring previously achieved exceptional brightness due to its very low equilibrium emittance of 7.6 pm rad. However, other figures of merit were significantly compromised. For example, as previously noted, the dynamic aperture was horizontally limited to less than 3 mm, which prohibited the off-axis injection and accumulation procedure. Additionally, the

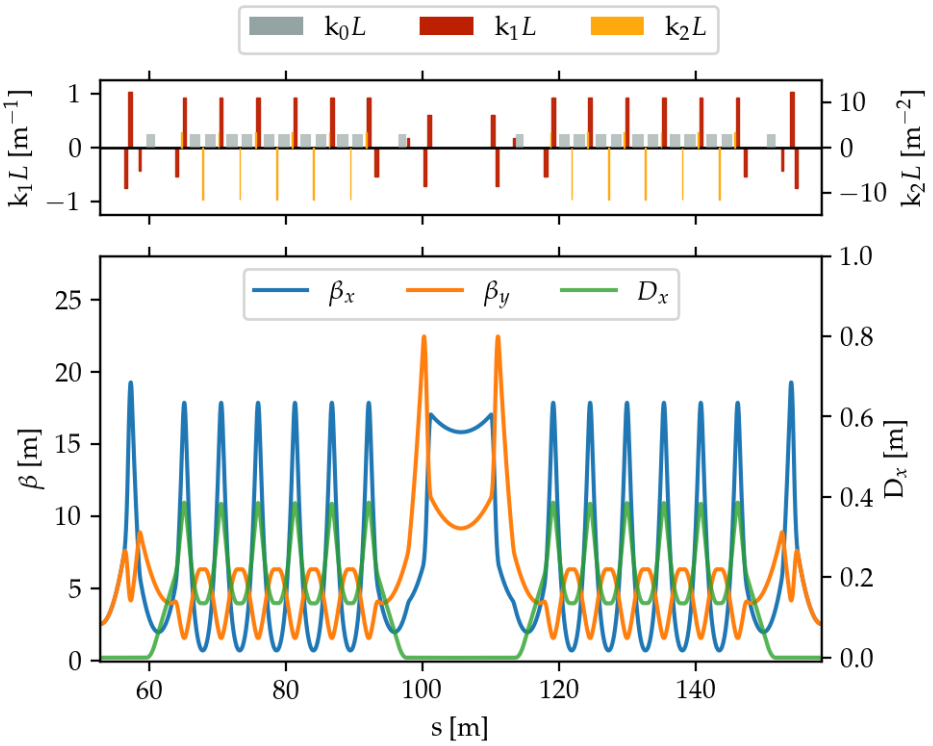

Figure 3.11: Lower panel: Optical functions of the first design of the booster ring upgrade DESY IV. Six arcs are composed of quasi seven-bend achromats. The straight sections alternate between low- and high-β insertions. Low-β straights are reserved for rf cavities and high-β straights for extraction and injection devices. This design was ruled out due to tunnel structure stability constraints. Upper panel: Quadrupole and sextupole integrated strengths are shown in red and yellow, respectively. The positions of the bending magnets are indicated as grey boxes.

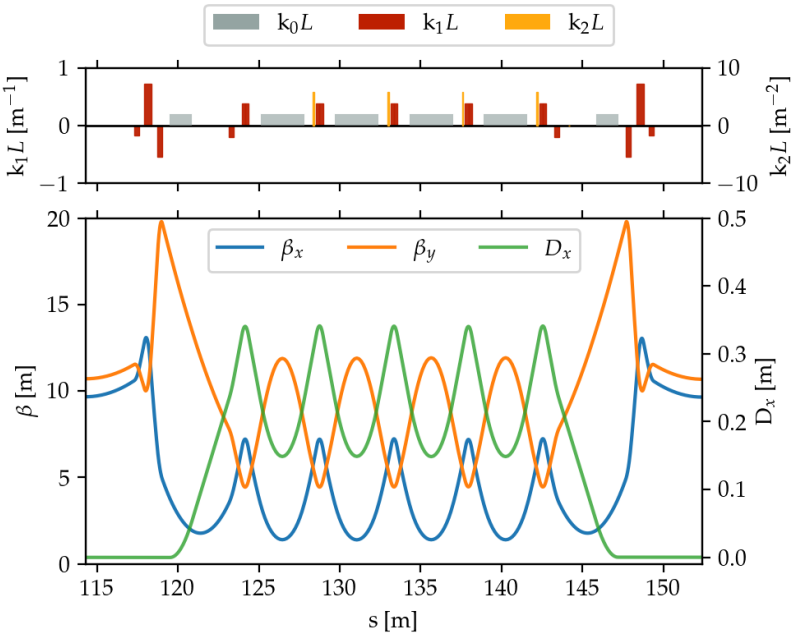

Figure 3.12: DESY IV optical functions of its six-bend achromat arc cell. The circumference has been scaled to 304.8 m and is composed of eight arc cells. Many of the elements have been fusioned to make space for beam diagnostics and vacuum devices. The long dipoles indicated in grey are combined function magnets with focusing and chromatic correction components.

beam lifetime was significantly reduced, reaching approximately 30 minutes in brightness mode and just a few minutes in timing mode.

To maintain the required current stability of one percent, a swap-out injection scheme was proposed, in which deteriorated stored beams are replaced with fresh electron bunches from the booster. Consequently, the first booster was specifically designed with an ambitious single-bunch charge threshold to compensate for the reduced lifetime and dynamic aperture. This design also aimed to deliver full charge electron bunches for timing mode operation, similar to the APS-U design. Later, with the development of the beam dynamics by the introduction of hybrid six-bend achromat arc cells, the high single bunch charge operation would not be needed. The machine was intended to be installed in the ceiling of the existing tunnel. Static analysis of the structure ruled out this possibility in 2024 and therefore a new design was developed.

The current design of the booster ring DESY IV[2] was derived from the previous one. The optical functions are illustrated in figure 3.12. The ring has been scaled in circumference from 316.8 m to 304.8 m. The straight sections are not alternating but identical. Eight arc cells now compose the ring and resemble a *pure* six-bend achromat. The performance of the booster ring is comparable to the prior design. Considering the lifetime of the main storage ring implies, that charge top-up has to happen every half hour for the brightness mode and every 6 min for the timing mode. This implies that the booster ring and the complete pre-injection chain would remain idle for long periods. The main parameters of both booster rings are summarized in table 3.5.

[2]designed by J. Keil

As a concluding side note to the booster synchrotron discussion, in 2024 after the impossibility of the installation of the six-fold symmetric lattice was established, a competing project proposal for an injector has gained momentum. This proposal envisions a high-repetition full energy laser-plasma accelerator [93, 90]. Therefore it has been tentatively considered to skip the installation of the new booster ring DESY IV and wait until the technologies necessary for the realization of the laser-plasma accelerator are available. Studies of a bridging solution, such as to refurbish and continue operating the current booster synchrotron DESY II have been studied. This also would require a refurbishment of critical components in the accelerator chain. Additionally, the integration of an extraction and transfer channel has not yet been considered in the design of DESY IV. The ability to deliver electron beams would fulfill the needs of the existing test user facility, which currently relies on parasitically sourced electron-positron beams from DESY II [94]. To address this requirement in Chapter 6 we summarize our proposal for a resonant slow extraction from the booster ring.

4

Round beam operation

After examining the beam dynamics of the main storage ring and the booster ring, this chapter presents a comprehensive study on round beams at PETRA IV. The investigation covers generation methods, their impact on beam dynamics performance, and experimental results of off-axis injection at PETRA III and ESRF.

4.1. Generation of round beams at PETRA IV

To generate round beams the equilibrium vertical emittance has to be increased or the transversal emittances have to be equalized in order to avoid detrimental consequences for the photon brightness. As it has been discussed in Chapter 2, the theoretical considerations of three mechanisms to do this in a controled way are discussed. We now demonstrate some of the results with the PETRA IV lattice.

4.1.1. Vertical dispersion waves

The first method assessed is the introduction of vertical dispersion waves in the arc cells of the storage ring. With help of the available orbit correctors numerous closed dispersion waves can be generated. Ample space is also available in the straight sections. The critical regions, where residual vertical dispersion should be kept to a minimum, is in the arc cells straights sections. In these spaces, where insertion devices are intended to be installed, the photon production will be sentitive to the electron beam size

$$\sigma_y = \sqrt{\epsilon_y \beta_y + (D_y \sigma_\delta)^2},$$

where σ_δ is the rms equilibrium enegy spread (see tables 3.2 and 3.4). Next, we evaluate simple vertical dispersion closed bumps, similar to the implementation reported in [18]. The implementation of these dispersion waves is performed in `MADX` [34], together with the calculation of the transversal equilibrium emittances. Four of the available orbit correctors are used. Then various matching algorithms are utilized to close the bumps with numerical precision. The result of the simplest configuration is shown in figure 4.1. The bump generates approximately one pm rad of vertical emittance (see equations 2.3 and 2.25). The maximal corrector strength needed is 270 µrad and is well below the corrector specification of 500 µrad.

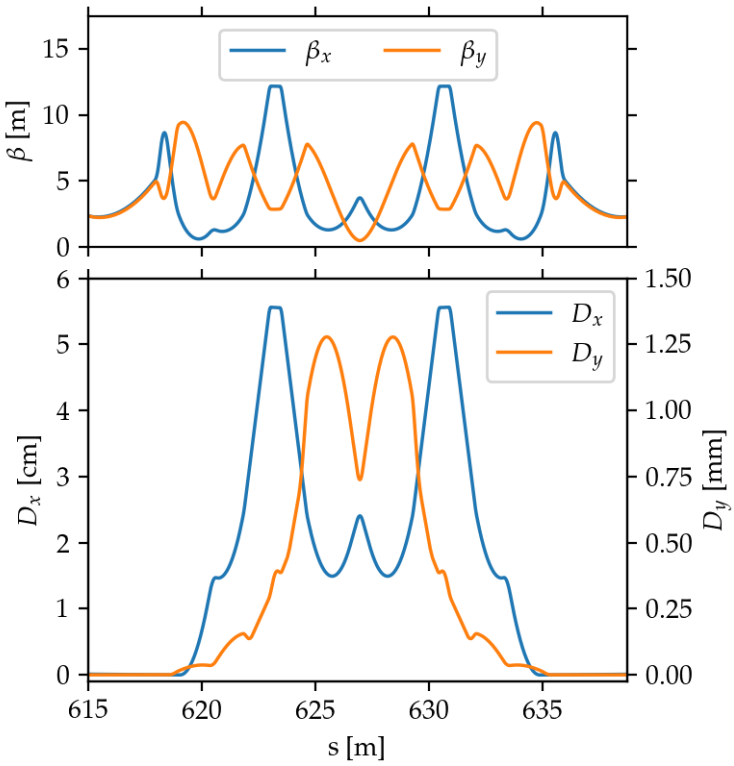

Figure 4.1: Simple closed vertical dispersion bump implemented in one H6BA arc cell. The vertical dispersion generates one pm rad increment in the equilibrium emittance.

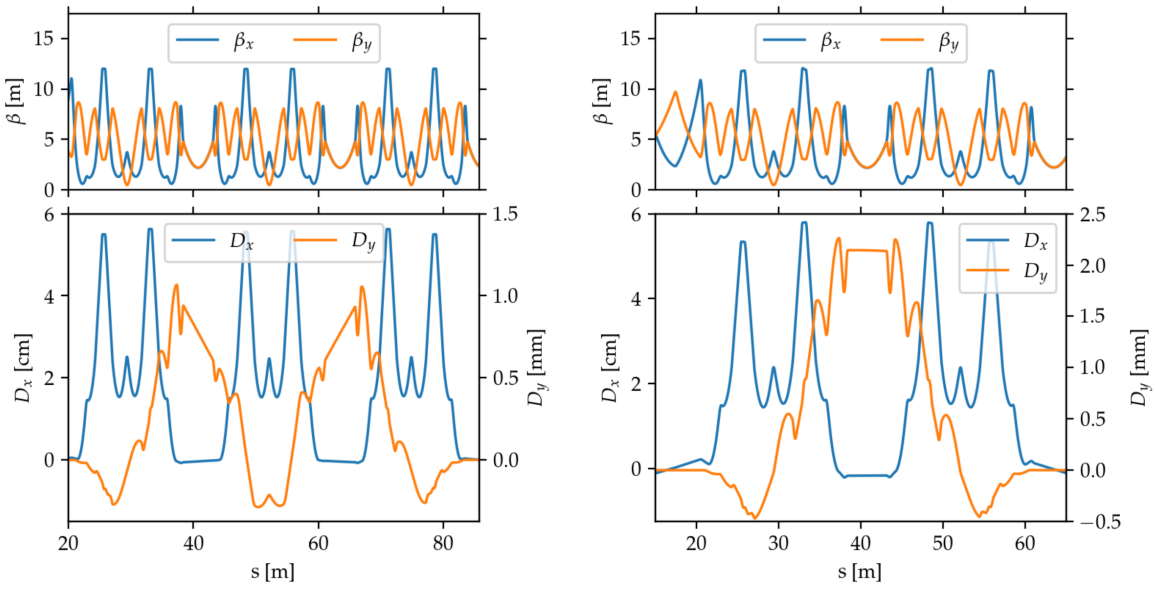

Figure 4.2: Possible vertical dispersion waves at the straight sections designated for damping wigglers. Generation of vertical emittance is less effective.

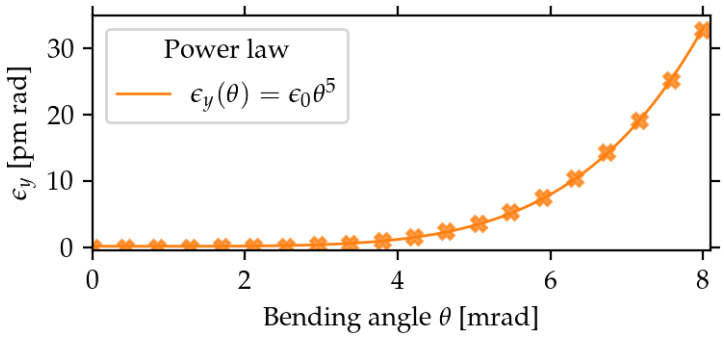

Figure 4.3: Vertical emittance against bending angle in a simple closed vertical orbit bump. The crosses indicate the calculation from MADX [34]. The vertical emittance follows a simple power law (solid curve).

Other possible configurations are illustrated in figure 4.2, where straight sections designated for damping wigglers are considered. Generation of the bumps is possible, but perfect closing of the waves appears to be less straightforward. Also, contribution to the equilibrium emittance is less effective, being approximately half a pm rad for each of the configurations displayed.

To finalize this exercise, we consider the case where dispersion has been created with a simple closed vertical orbit bump in free straight sections: three bumpers spaced equally with the first and third bumper giving a kick θ and the middle one -2θ. The β-functions are symmetric around the position of the middle vertical kicker. We assume that the bending angle is fixed and thus the (local) bending radius $\rho_y = L_D/\theta$ with L_D being the length of the bending magnet ($\rho_y = -L_D/2\theta$ for the middle bumper). This setup is also commonly known as a chicane. Following equation 2.3 it is easy to follow that $D_y \propto 1/\rho_y = \theta/L_D$. Since $\mathcal{H}_y \propto 1/\rho_y^2$, then the vertical emittance scales as

$$\epsilon_y(\theta) \propto \frac{1}{|\rho_y|^5} = \left|\frac{\theta}{L_D}\right|^5 . \tag{4.1}$$

This dependency is illustrated in figure 4.3, where three closed vertical orbit bumps are installed in PETRA IV at free insertion device (ID) slots. The coefficient ϵ_0 is in this case close to unity.

To summarize, the generation of vertical dispersion waves in PETRA IV is feasable. To generate round beams 20 arc cells need to include simple closed bumps as illustrated in figure 4.1. The maximum needed corrector strength is 270 µrad and is about half of the specified maximal strength to perform orbit correction. This might be an impediment for the scheme, since the corrector strengths in designated cells for vertical dispersion bumps could approach saturation more promptly. They would need to be able to keep the orbit flat and generate vertical dispersion.

Additionally the generation of more sophisticated waves can be pursued (see figure 4.2), but no evident advantage for this has been identified thus far. The implementation of simple vertical bumps can also be done at available straight sections. For this simplified version, we illustrate the functional dependency on the chichane bending angle. The contribution to the vertical emittance follows a simple power law.

To evaluate more properly the technical considerations and performance contraints of this approach a systematic study including realistic misaligment and magnetic gradient errors has to be performed, similar to the one reported in [95]. The extension of the vertical dispersion bump functionality beyond vertical emittance control could also be assessed. Especially a longer closed bump with even higher dispersion values can function as a good technique to extend the machine protection capabilities. This goes beyond the scope of the current study on vertical dispersion waves at PETRA IV.

4.1.2. AC dipole excitation

Another possibility to increase the vertical emittance in a controled manner is to actively drive the betatron motion. The most efficient way to do this, is by doing so resonantly, hereby including the betatronic oscillation frequency in the spectrum of the excitation wave. The manipulation and forming of beams through external electromagnetic waves have broad applications in particle accelerators. These can range from triggering emittance dilution in case of an emergency abort [96], populating non-linear transversal resonance island buckets [47, 97] to controlling the blow-up of emittance for resonant slow extraction [98]. Vertical emittance blow-up with an external quasi-noise signal is currently used at ESRF-EBS in operations [99].

Although the method is straightforward, the challenge lies in selecting the optimal excitation signal to efficiently stimulate betatron motion. In this section, we present results from two considered signals: a colored noise band and a single sine wave. Part of this work has been included in a deliverable for the "European network for developing new horizons in research infrastructures" (EURIZON) [100].

Sine-wave

For the sine-wave excitation signal it is assumed that the tune q_y is known and only affected by chromatic spread. The frequency of the excitation is set to $\omega_{\text{exc}} = 2\pi f_{\text{rev}} q_y$. Next, a multi-particle simulation is performed with `Xsuite` [101] to evaluate the validity of equation 2.32. The beam is initialized with the values listed in Table 3.4 and is composed of a sample of 10^4 particles. Particles are tracked element-by-element (thin) with the effects of synchrotron radiation and quantum excitation. Several excitation amplitudes are utilized. The results are illustrated and summarized in figure 4.4. The equilibrium emittance scales quadratically with the kick amplitude θ_{max}. According to the simulation, 15 nrad are sufficient to generate $\epsilon_y = 20\,\text{pm rad}$. Note that a coherent centroid oscillation is excited, as depicted in the top panel of figure 4.4. This might become a limitation for the method since the centroid stability strived for is constrained to be no more than 10% of the beam size, in this case $|\bar{y}_{\text{max}}| < 1.2\,\mu\text{m}$.

Additionally, we evaluate the expected equilibrium emittance dependency on the vertical chromaticity by performing a scan over this parameter. To this end tracking simulations are performed with the same setup and fixed excitation amplitude $\theta_{\text{max}} = 15\,\text{nrad}$. The results are illustrated in figures 4.5 and 4.6. Note that the equilibrum vertical emittance functional dependency on the vertical chromaticity follows the expected inverse law as described in equation 2.32. This behaviour appears to be valid for expected operational values of the vertical chromaticity ($\xi_y > 4$). Below this threshold the emittance is dictated by coherent oscillations of the bunch and therefore not optimal for operation or generation of round beams.

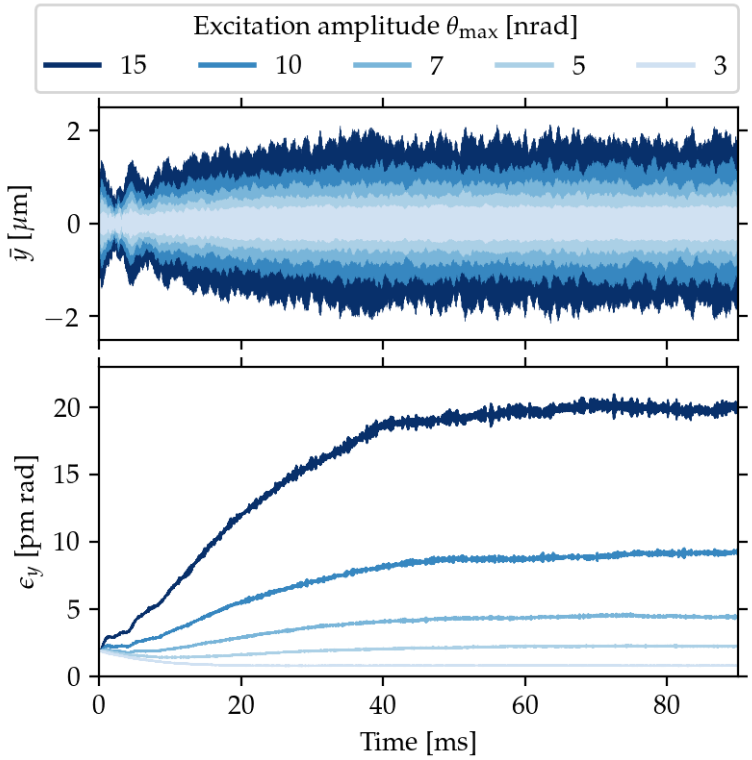

Figure 4.4: Vertical emittance and centroid evolution during excitation. Upper panel: Vertical beam centroid during excitation with a sine-wave, whose frequency lies at the betatron resonance $f_{exc} = q_y f_{rev}$. Lower panel: Vertical beam emittance during the excitation process. The different shades of blue indicate the strength of the excitation. The beam centroid oscillations are recorded at injection point with (β_y, α_y) =(7 m, 0) and nominal chromaticities (see table 3.2).

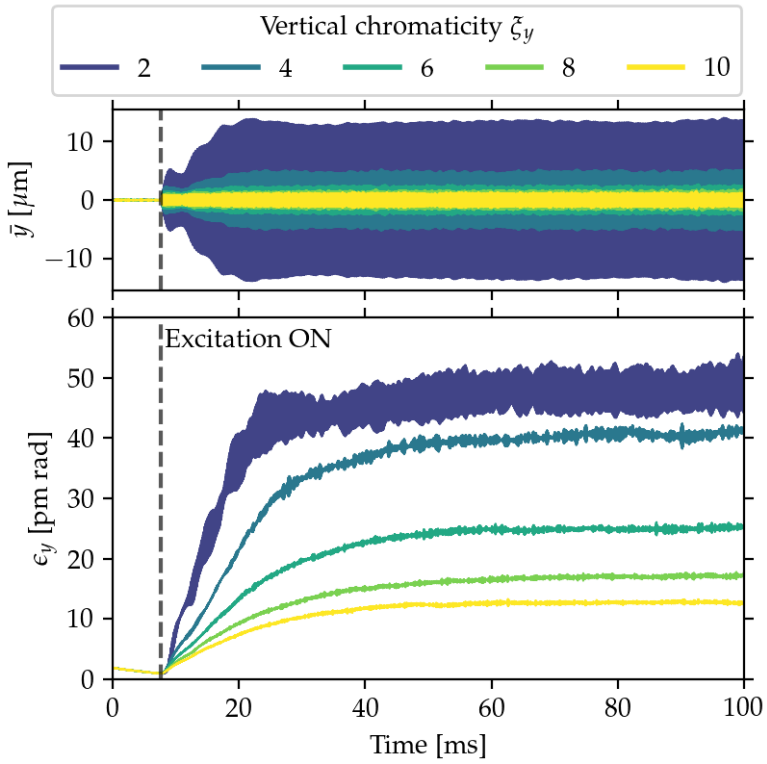

Figure 4.5: Vertical emittance and centroid evolution during excitation. Upper panel: Vertical beam centroid during excitation with a sine-wave, whose frequency lies at the betatron resonance $f_{\mathrm{exc}} = q_y f_{\mathrm{rev}}$. Lower panel: Vertical beam emittance during the excitation process. The different colors indicate the value of the vertical chromaticity. The excitation strength $\theta_{\mathrm{max}} = 15\,\mathrm{nrad}$. The beam centroid oscillations are recorded at injection point with (β_y, α_y) =(7 m, 0). For low chromaticities $\xi_y \leq 2$ the beam centroid oscillations account for most of the beam vertical emittance.

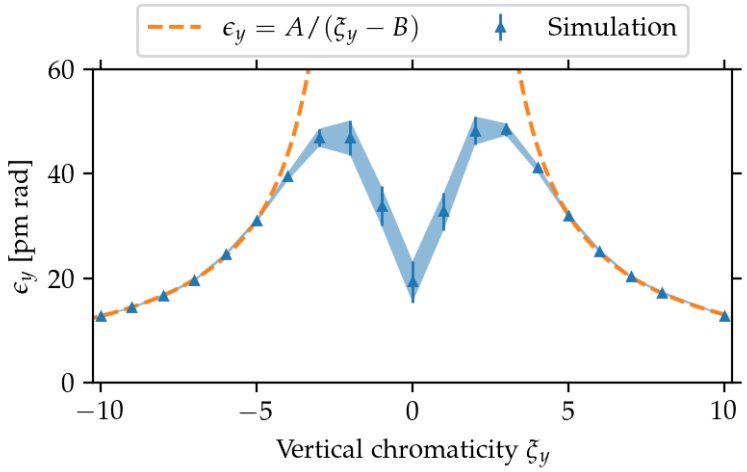

Figure 4.6: Emittance dependency on the vertical chromaticity. The $1/\xi_y$ behaviour is reproduced for operational values of the chromaticity.

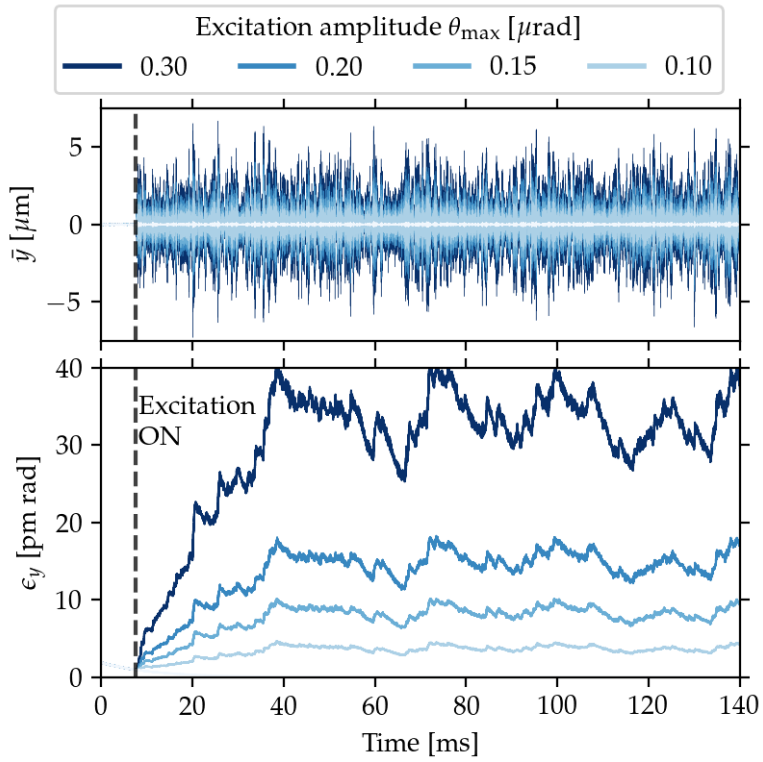

Figure 4.7: Upper panel: Vertical beam centroid during excitation with a noise-band signal, whose spectrum covers the betatron resonance $f_{exc} = q_y f_{rev}$. Lower panel: Vertical beam emittance during the excitation process. The different shades of blue indicate the strength of the excitation. The beam centroid oscillations are recorded at injection point with (β_y, α_y) =(7 m, 0) and nominal chromaticities (see Table 3.2).

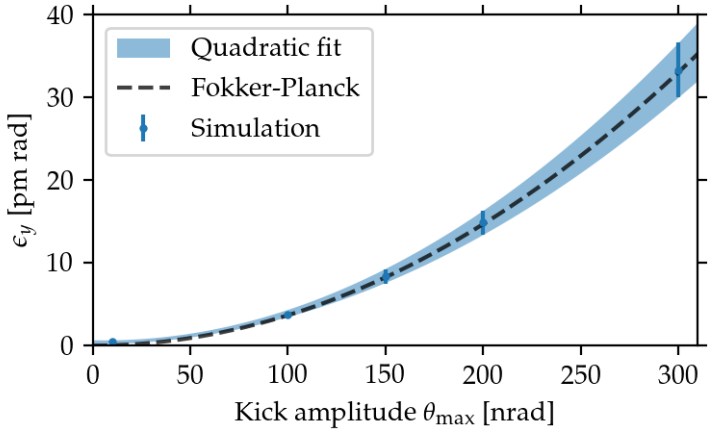

Figure 4.8: Emittance as a function of excitation strength. The diffusion coefficient for the displayed Fokker-Planck functional dependency is multiplied by a factor six.

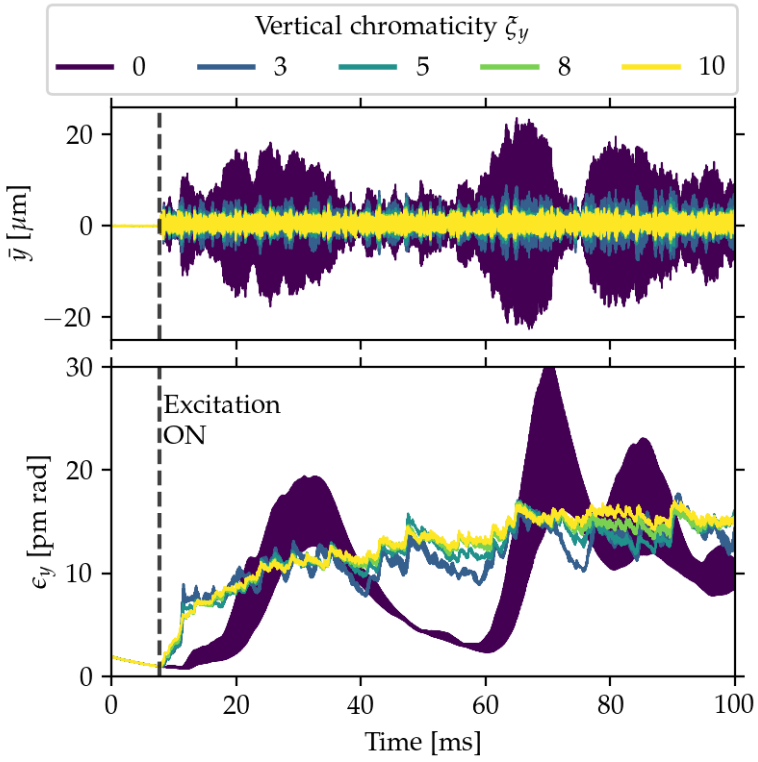

Figure 4.9: Upper panel: Vertical beam centroid during excitation with a noise-band signal, whose spectrum covers the betatron resonance $f_{\mathrm{exc}} = q_y f_{\mathrm{rev}}$. Lower panel: Vertical beam emittance during the excitation process. The different colors indicate the value of the vertical chromaticity. The excitation strength $\theta_{\mathrm{max}} = 200\,\mathrm{nrad}$. The beam centroid oscillations are recorded at injection point with (β_y, α_y) =(7 m, 0). For vanishing chromaticity the beam centroid oscillations account for most of the beams' vertical emittance.

White noise
Next the same simulations as presented before are performed, but with a different excitation signal. In this case, a noise band is generated, such that its spectrum covers at least the base betatron resonance $f_\beta = f_{\text{rev}} q_y$. The noise was generated from a sample drawn from a uniform distribution. The Nyquist-frequency of the signal is limited to $f_{\text{Nyq.}}$ =37.5 kHz and is enough to cover the betatron resonance and the expected chromatic spread of the beam. The amplitude scan results are illustrated in figures 4.7 and 4.8. Note that the results presented in figure 4.7 suggest that with this type of excitation no equilibrium state is reached. The vertical emittance does scale quadratically with the kick amplitude of the signal, but the diffusion coefficient from equation 2.37 does not predict the vertical emittance value from simulation. On the other hand the average emittance appears to be agnostic to the vertical chromaticity except for the case when it vanishes. This is illustrated clearly in figure 4.9. These two observations lead to the conclusion that the system cannot be well described as a diffusive process governed by the Fokker-Planck equation. The system exhibits a hybrid nature between a diffusive system and a collection of harmonic oscillators. The signal also excites the centroid motion as in the previous case with the single-frequency sine-wave. Generation of round beams is feasable with this method but is not the preferred solution, since the users might be affected by coherent centroid motion.

4.1.3. Emittance sharing

As the final variant we consider emittance sharing. For this method the tunes have to be brought near the coupling resonance fulfilling the condition $q_x = q_y$. Simulations show as expected, that the emittance ratio can be controlled and follows equation 2.47

$$\frac{\epsilon_y}{\epsilon_x} = \frac{\kappa^2}{\kappa^2 + \Delta^2}.$$

The introduction of misalignment errors has been performed and for each seed the resonance driving term can be determined. For the case where the set tunes $\Delta = q_x - q_y = 0$, the emittances converge to $\epsilon_x = \epsilon_y \approx 12.5$ pm rad [25]. The method appears to be straight-forward in simulation and is the preferred option for the generation and control of vertical emittance. There are no further considerations, since the resonance driving term will be unknown and determined by the misalignments and magnetic field errors of the machine. This value can be measured [61], corrected and controlled with skew quadrupole correctors installed in the storage ring [83].

4.2. Consequences to beam dynamics performance

In this section we evaluate the consequences to the beam dynamics performance of operating the machine near the coupling resonance to generate round beams. It is conventional wisdom that operating a machine near a resonance is inadvisable. In this case the coupling of the transversal motion would be a concerning mechanism impacting the injection efficiency. As it is illustrated in figure 3.6, the half-gap aperture in the vertical plane is about 3 mm at the insertion devices. High initial horizontal oscillation amplitudes (see figure 3.8) that later due to the motion coupling (see equation 2.41) evolve to vertical oscillations could lead to beam losses at insertion devices. The study of the off-axis injection at PETRA IV is documented

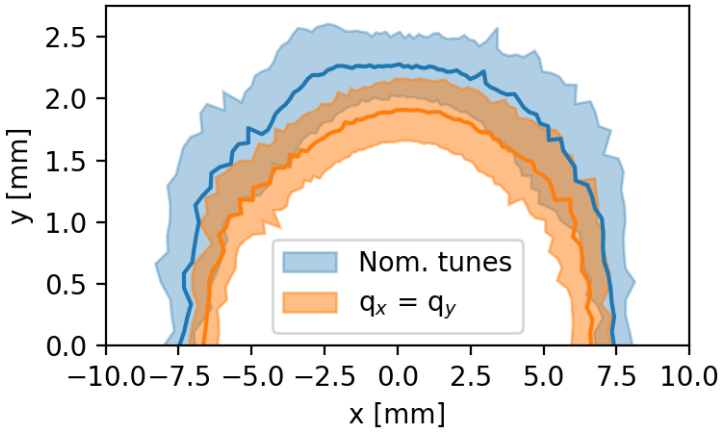

Figure 4.10: Comparison of dynamic aperture (DA) at the nominal working point and at the coupling resonance with $q_x = q_y = 0.18$. The solid lines indicate the average over ten machine realizations with an rms β-beating of approximately 5%. The shaded areas represent the corresponding rms of the calculated dynamic aperture over ten realizations. Figure taken from [25].

in [25] and here we summarize our results. We then include an extension of the impact on other figures of merit. Almost exclusively the operation of PETRA IV at the coupling resonance appears to be beneficial in terms of beam dynamics.

4.2.1. Dynamic aperture and local momentum acceptance

The calculation of the dynamic aperture is performed with `ELEGANT` with a reduced set of misalignment errors to generate a conservative rms β-beat of approximately 5%. The effects of synchrotron radiation and quantum excitation are included. Particle tracking is performed element-by-element with a third harmonic cavity system. The quadrupole strengths of the first two families in the arc cells are used to set $q_x = q_y = 0.18$. The chromaticity is maintained at the nominal values and the octupole strengths as well. The resulting dynamic aperture and a comparison to the nominal tune values is depicted in figure 4.10. The dynamic aperture is marginally decreased due to the vertical amplitude detuning. Since in this setup the vertical tune is closer to the integer resonance and the amplitude detuning is kept to a similar value with the octupole settings, the unperturbed machine reaches the integer resonance $q_y = 0$ at $J_x = 0.62\,\mu\text{m}$ or at injection $x_{\text{inj}} = 7.6\,\text{mm}$. For reference the horizontal tune hits the half-integer resonance $q_x = 1/2$ at $J_x = 0.78\,\mu\text{m}$ or at injection $x_{\text{inj}} = 8.5\,\text{mm}$ in the ideal machine.

On the other hand the local momentum acceptance (LMA) has been calculated as well with `ELEGANT` with the same setup. The results are illustrated in figure 4.11. The simulation shows that the average LMA remains almost the same for both working points for the considered machine realizations. Considering the seed to seed fluctuations it is safe to assume that the LMA is not considerably decreased nor increased by operating the machine near the coupling resonance.

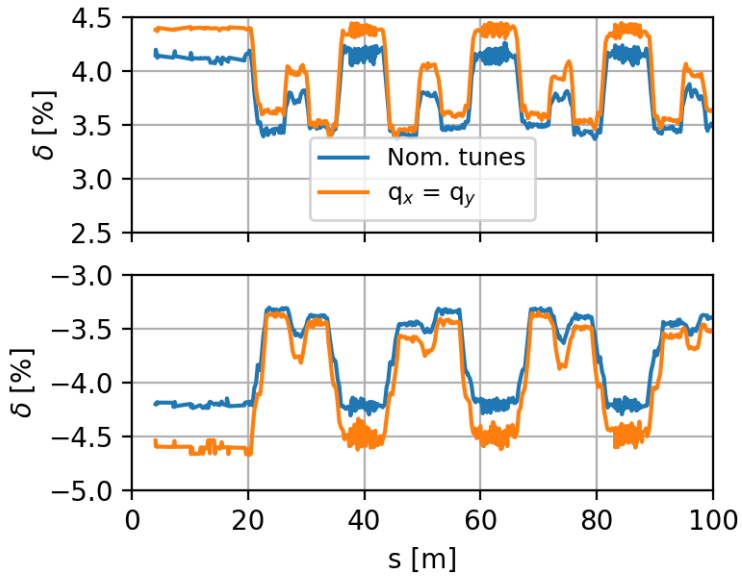

Figure 4.11: Comparison of local momentum acceptance (LMA) at the nominal working point and at the coupling resonance with $q_x = q_y = 0.18$. The solid lines indicate the average over ten machine realizations with an rms β-beating of approximately 5%. Figure taken from [25].

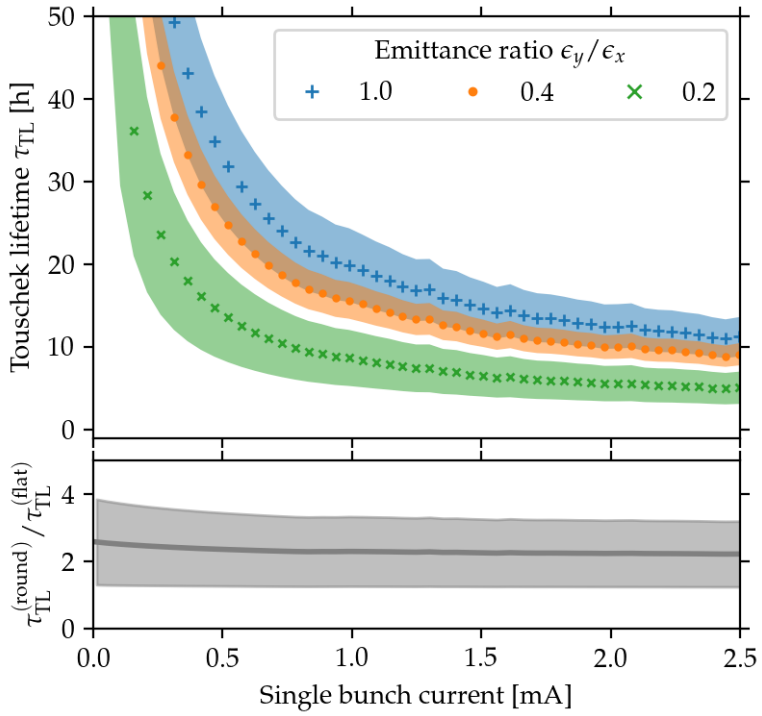

Figure 4.12: Touschek lifetime as a function of single bunch current. The top panel shows the lifetime for three different emittance ratios. The shaded areas indicate the rms value of different machine realizations with an rms β-beating of approximately 5%. The lower panel displays the lifetime ratio between the round beam $\epsilon_y/\epsilon_x = 1$ and the flat beam (20% emittance ratio) case.

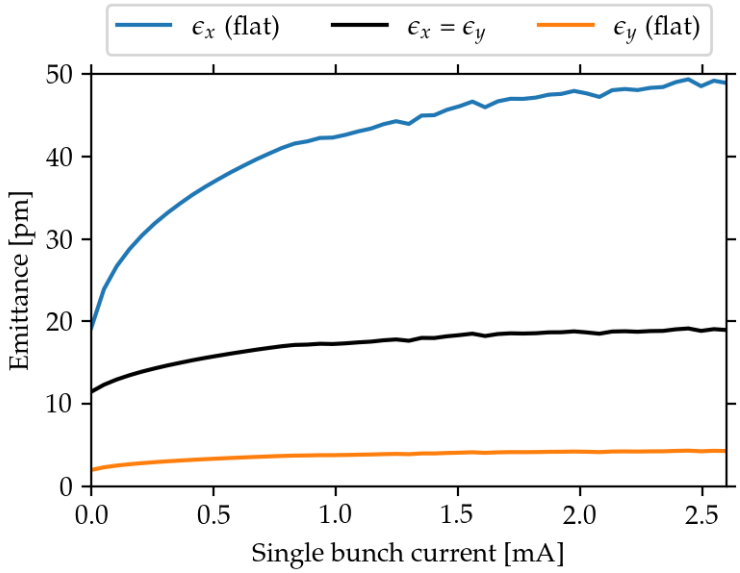

Figure 4.13: Transversal equilibrium emittances as a function of single bunch current for the round and flat ($\epsilon_y/\epsilon_x = 0.2$) beam operation modes. The effects of impedance and intra-beam scattering have been included.

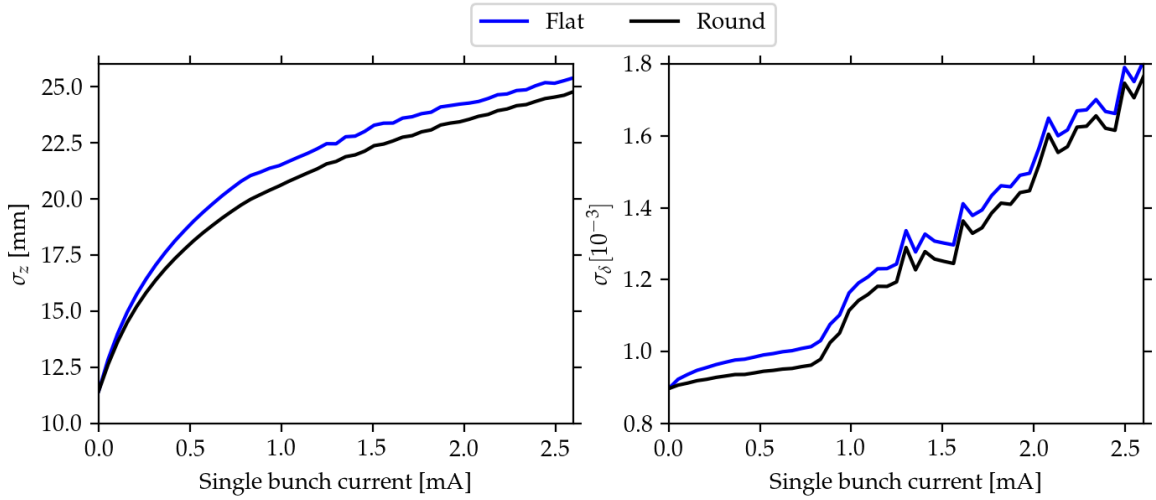

Figure 4.14: Longitudinal equilibrium beam parameters as a function of single bunch current for the flat and round beam operation modes. The effects of impedance and intra-beam scattering have been included.

4.2.2. Beam lifetime and electron beam parameters

The electron beam parameters have been calculated with a set of misalignment errors that generate an rms β-beating of approximately 5%. The resonance driving term has been determined and used to infer the tune distance $\Delta = q_x - q_y$ to generate an emittance ratio ϵ_y/ϵ_x of 20%, 40% and unity. The impedance model has been included in the calculation, since its influence elongates the beam longitudinally and after the microwave instability threshold (around 0.75 mA) also the momentum spread increases [23]. With these effects and the pre-calculated LMA of PETRA IV the Touschek lifetime has been computed with the tool implemented in `ELEGANT` for different single bunch currents[1]. The results are exemplified in figure 4.12. The lower panel shows clearly the increase of Touschek lifetime by a factor two. This result was reported by A. Piwinski [66] as discussed in Chapter 2 and showcased with the achromat cell.

Further, the equilibrium parameters of the electron beam are calculated including intra-beam scattering contributions with `ELEGANT`. The evolution of the transversal emittances as the single bunch current is increased is illustrated in figure 4.13. The longitudinal parameters are displayed in figure 4.14. While the transversal emittance blow-up leads for the flat beam configuration to a 120% increase in horizontal emittance at 2 mA single bunch current, the coupled beam configuration diminishes this increment to only 90%, from 11.5 pm rad to 19 pm rad. The blow-up is mitigated thanks to the lower beam density. The longitudinal plane appears to profit marginally from the decreased IBS scattering rate in round beam mode, nonetheless the beam deformation is still dominated mainly by wakefield contributions.

4.3. Off-axis injection

In this section we would like to dive more deeply into the consequences for the off-axis injection by operating the machine at the coupling resonance. We first discuss simulation results obtained for PETRA IV and continue with the presentation of experimental results of beamtime obtained at PETRA III and ESRF-EBS.

4.3.1. PETRA IV simulation

The injection efficiency of PETRA IV appears to be not compromised, as it is illustrated in figure 4.15. Here the injection efficiency has been calculated with tracking simulations and can be understood with help of the information displayed in figure 4.10.

First, for this set of simulations the injected beam has been manipulated, such that the beam emittance of the injected beam has been transformed from $(\epsilon_x, \epsilon_y) = (20\,\text{nm rad}, 2\,\text{nm rad})$ to $\epsilon_x = \epsilon_y = 13.7\,\text{nm rad}$. This substancially reduces the injected beam size such that a 3 rms bunch fits within the available dynamic aperture displayed in figure 4.10. Secondly, the amplitude detuning coefficients displace both transversal tunes such, that the coupling resonance is not excited, i.e. $\Delta = q_x - q_y \gg 0.1$. Hence no motion exchange between planes takes place and the horizontal oscillations damp due to synchrotron radiation.

An interesting result of the simulation campaign is the generation of resonance islands. These are illustrated in figure 4.16. Approximately 10% of injected particles get trapped in

[1] calculation is performed in close collaboration with C. Li

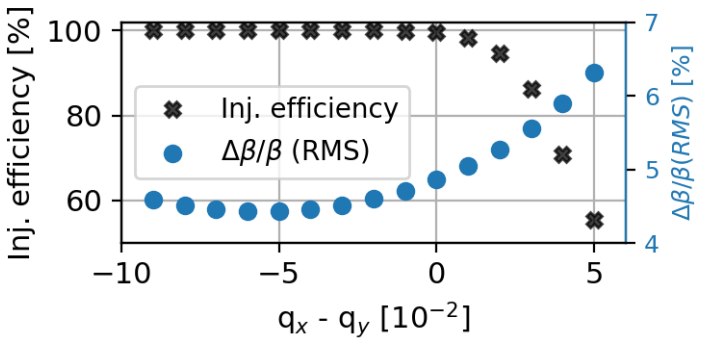

Figure 4.15: Black crosses indicate the PETRA IV injection efficiency as a function of the distance to the coupling resonance. The injection efficiency is not compromised by displacing the working point of the storage ring, until the coupling resonance. The blue dots illustrate the rms β-beating with respect to the nominal optics. Figure taken from [25].

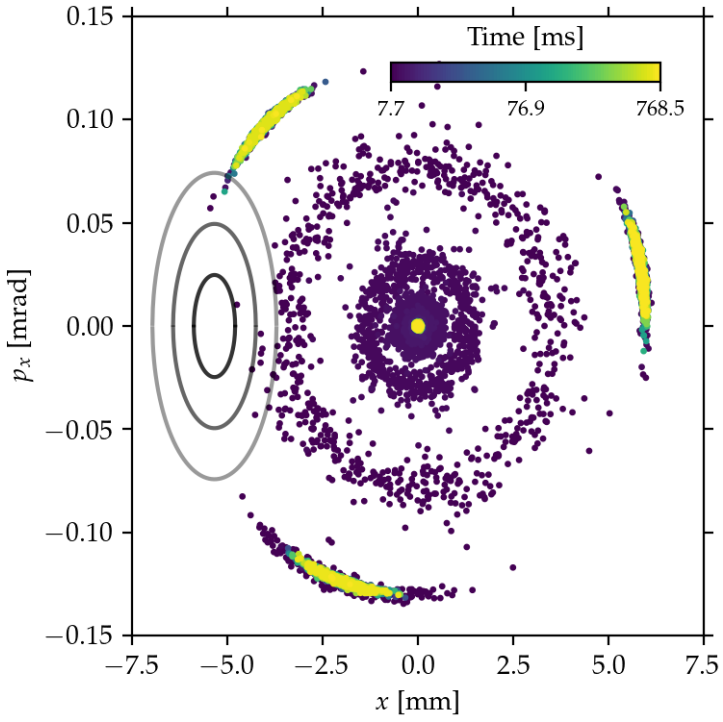

Figure 4.16: Evolution of a 3 rms injected particle distribution (left grey ellipses) at PETRA IV. The injected particle ensemble is shown every 1000 turns. 90% of the particles damp towards the center in a few synchrotron radiation damping times (approximately 60 ms). The rest is trapped in resonance islands around the core. This is observed in most of the machine realizations simulated. Observation point is at injection with $(\beta_x, \beta_y) = (46, 7)$m and $\alpha_{x,y} = 0$.

these islands during the off-axis injection process. The rest damps towards the center. In Chapter 5 we discuss in more detail this finding.

4.3.2. PETRA III experiment

To corroborate the results from the simulations performed for PETRA IV experimental campaigns are pursued at PETRA III. The main objectives of the campaigns are to investigate the round beam generation by setting the machine tunes at the coupling resonance and the investigation of the injection efficiency. PETRA III is the largest third-generation synchrotron light source ever conceived. The machine was repurposed after the high-energy physics programm was concluded. More details about the storage ring can be found in [20]. Next, we describe simulation results for PETRA III at DESY.

PETRA III simulation

To set the simulation a model that includes the magnet field and misalignment errors has been utilized [102][2]. The error model has been imported from `MADX` [34] to `Xsuite` [101]. Next, the off-axis injection has been simulated by displacing the transvesal tunes to the coupling resonance $q_x = q_y = 0.18$. The model yields a resonance driving term of $\kappa = 6 \times 10^{-4}$. Control of this parameter can be in principle achieved with help of the skew quadrupoles available at PETRA III.

Additionally, the amplitude detuning coefficients are key to ensure an effective off-axis injection, when the working points are at the coupling resonance. These coefficients for PETRA III with tunes $(Q_x, Q_y) = (37.18, 30.18)$ and nominal chromaticities $(\xi_x, \xi_y) = (2, 2)$ read $(\kappa_x, \kappa_y) = (-0.44, -2.05)$ mm^{-1}. These values have been calculated with tracking simulations in `Xsuite` and are compatible with the measurements performed at commissioning [103]. Note that the coefficients are three orders of magnitude lower than for the future light-source PETRA IV, i.e. the detuning with amplitude is almost negligible in PETRA III. This is a result of more prevalent linear optics at PETRA III, where stability and regular motion is ensured by design. In principle, the amplitude detuning coefficients can be increased to emulate more the situation for PETRA IV. This can be done by operating the machine at 5 GeV. This mode has been already implemented at DESY to save energy [104]. Unfortunately, simulations show that only a marginal increment in the coefficients is possible, with $(\xi_x, \xi_y) = (1, 10)$ then $(\kappa_x, \kappa_y) = (-0.75, -2.5)$ mm^{-1}.

Finally, tracking simulations are performed with 10^4 particles including the effects of synchrotron radiation and quantum excitation. A scan over the strength of the resonance driving term κ is performed to evaluate the constraints on the correction requirements to achieve efficient off-axis injection. Figure 4.17 illustrates two cases, one where the machine posseses a low resonance driving term (RDT) $\kappa = 10^{-3}$ and another case where the RDT is $\kappa = 10^{-2}$. It is clear that by increasing the resonance driving term the ample horizontal oscillations will couple into the vertical plane, thus increasing the vertical beam size considerably. This should be avoided. Figure 4.18 shows the centroid and emittances of the injected particles over 2048 turns. Note that when $\kappa = 10^{-2}$ the vertical centroid oscillations are in excess of 5 mm and thus too close to the physical aperture.

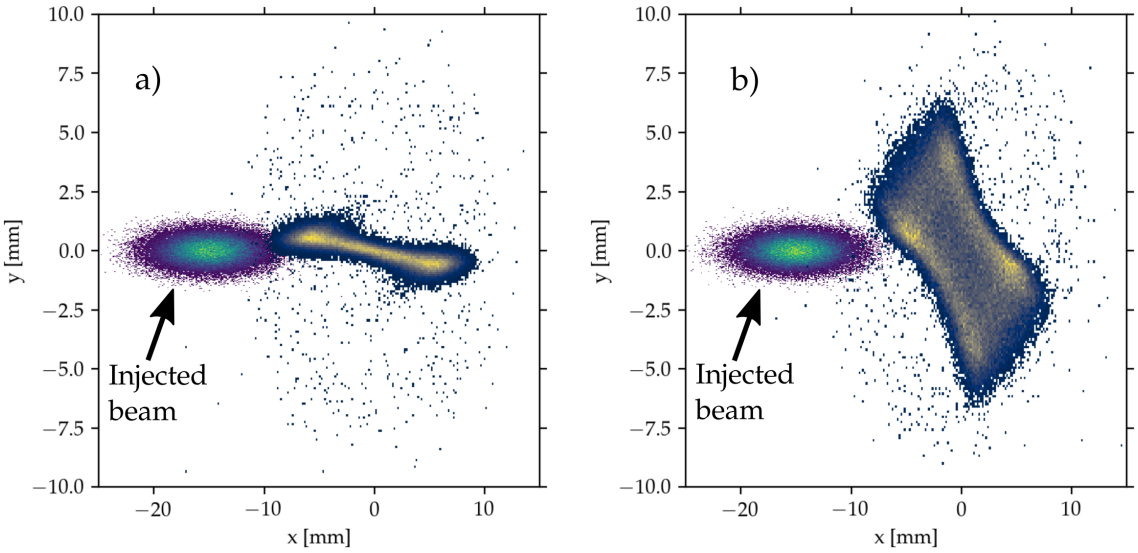

Figure 4.17: Injected beam distributions comparison after 2048 turns. (a) On the left the injected beam distribution and the damped distribution after 2048 turns are displayed. The resonance driving term has been increased to $\kappa = 10^{-3}$. (b) On the right the same information is illustrated, but here the resonance driving term has been increased to $\kappa = 10^{-2}$.

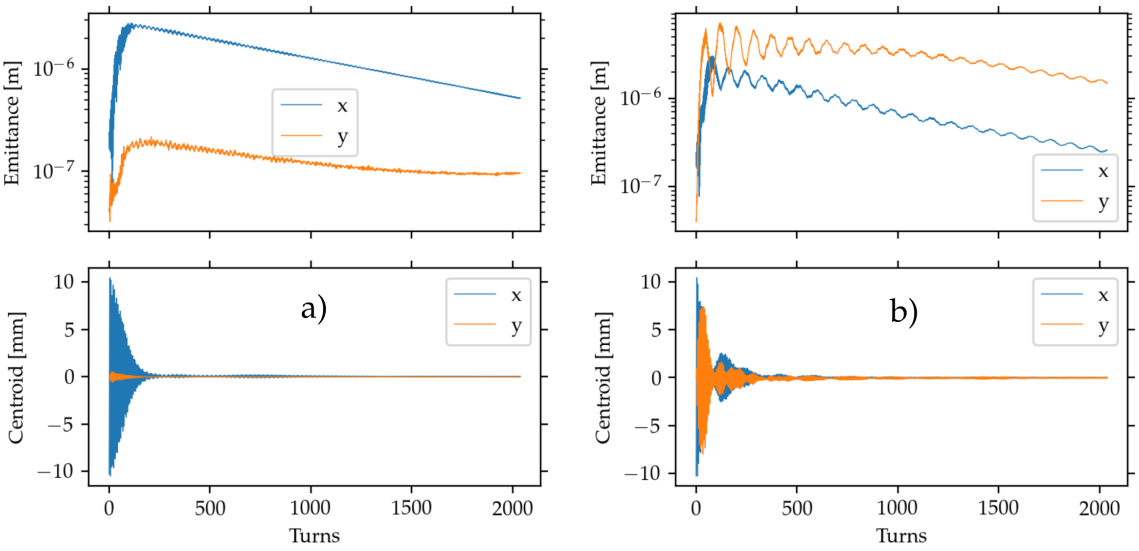

Figure 4.18: Beam emittance and centroid during the first 2048 turns after off-axis injection.(a) On the left the case where the resonance driving term $\kappa = 10^{-3}$ is shown. (b) On the right the same information is illustrated, but here the resonance driving term has been increased to $\kappa = 10^{-2}$.

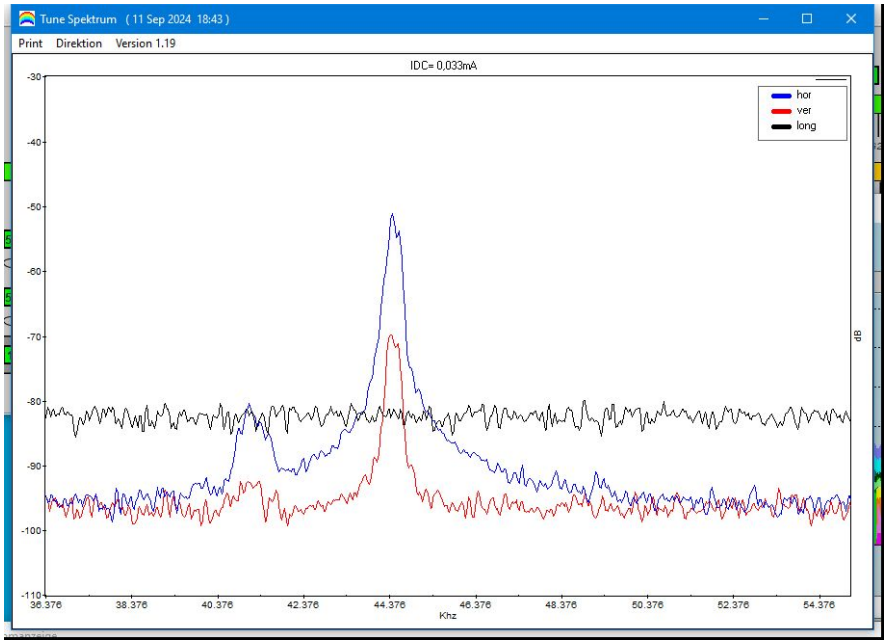

Figure 4.19: Snapshot of the tune measurement diagnostic at PETRA III control room. The blue and red curves show the measured horizontal and vertical betatron frequencies measured during the experiment $f_{\beta,x,y} = f_{\text{rev}} q_{x,y}$. The horizontal axis displays the measured frequency, whereas the vertical the attenuation of the measured signal from the beam. The resonance condition $q_x = q_y$ is fulfilled and round beams are generated.

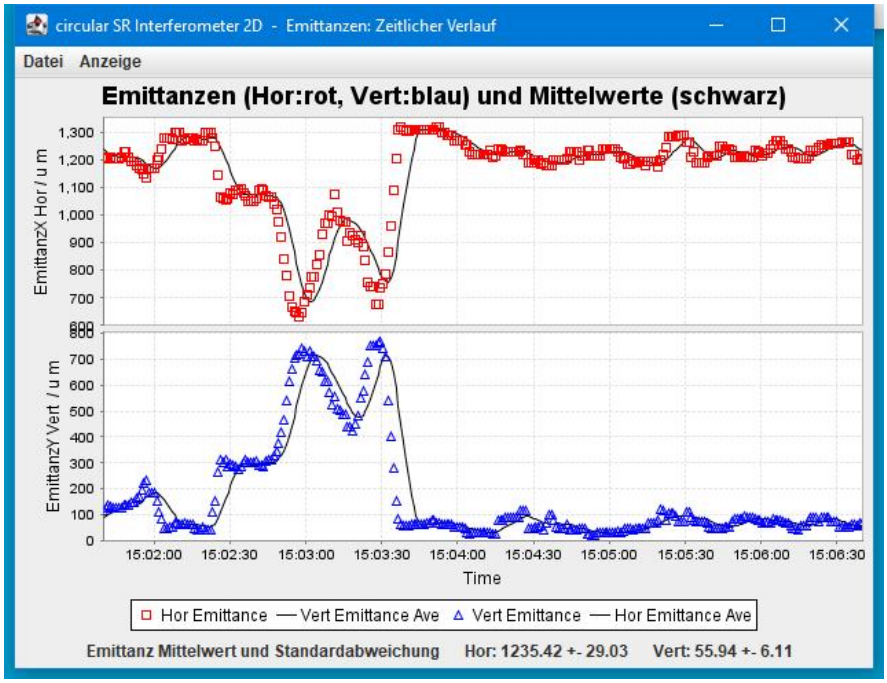

Figure 4.20: Snapshot of the emittance measurement diagnostic at PETRA III control room. The top panel and lower panels display the horizontal and vertical emittances, respectively, recorded during the experiment. Note that this is an exemplary shot of the round beam generation.

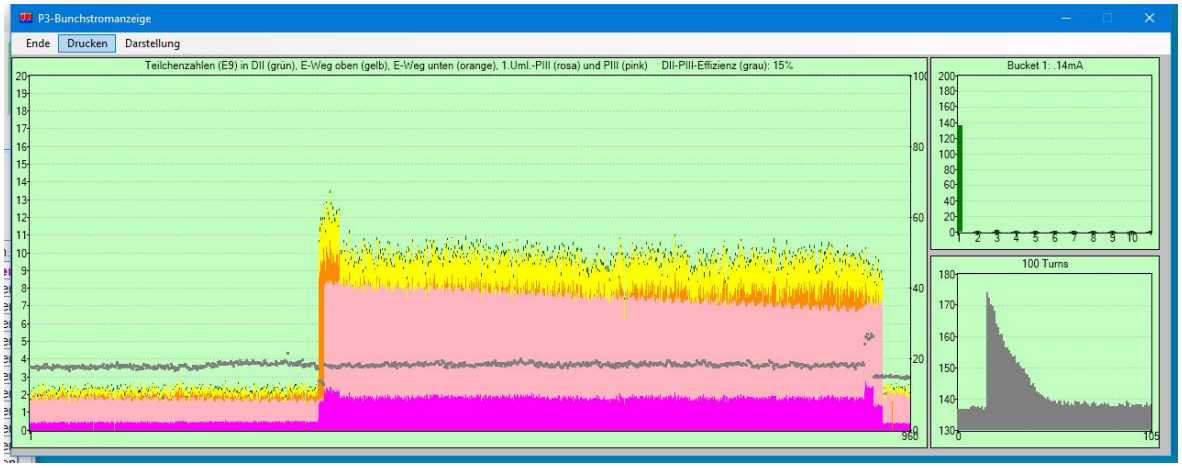

Figure 4.21: Snapshot of the injection efficiency diagnostic recorded during the round beam setup at PETRA III. The grey points in the left panel display the injection efficiency from the booster DESY II to PETRA III. The highest efficiency recorded was around 20%.

Experimental results

For experimental investigations at PETRA III, two machine development timeslots were granted. These took place the 29th of August and the 11th of September of 2024. On the first shift in August primarly the injection efficiency was investigated. The machine tunes were displaced to fullfil the resonant condition $q_x = q_y$ and thus round beams were generated. The machine was filled with 40 bunches in a uniform pattern with a total current of approximately $I_{\text{tot}} = 20\,\text{mA}$. The tune setup required a couple of iterations until the round beam condition was achieved. Setting the tunes near the coupling resonance was in practice not an issue. The experimental setup is better illustrated in figures 4.19 and 4.20. In figure 4.19 the tune measurement diagnostic in the control room is displayed. The pickup delivers a signal of $f_{\beta,x} = f_{\beta,y} \approx 44.376\,\text{kHz}$. This corresponds to tune values of $q_x = q_y = f_\beta / f_{\text{rev}} = 0.34$. The generation of round beams was diagnosed with the available tools and are illustrated in figure 4.20. Here an example is illustrated of the round beam generation, where $\epsilon_x = \epsilon_y = 800\,\text{nm rad}$. The generation of round beams appeared to be relatively simple, with the application in the control system to rematch the tunes. On the other hand, the injection efficiency appeared to reach values of $< 5\%$. A tune scan was performed (not systematically) along the coupling resonance condition line $q_x = q_y$, to investigate if the injection efficiency could be increased. This was achieved at $f_{\beta,x} = f_{\beta,y} \approx 45.6\,\text{kHz}$ corresponding to tune values of $q_x = q_y = 0.35$. The maximum injection efficiency reached the 20% mark and it is illustrated in figure 4.21. This value is insufficient for optimal operation at the coupling resonance for the generation of round beams. Reported experimental results demonstrate that higher injection efficiencies are possible. Still, the maximum value reported for injection efficiency by operating the machine at the coupling resonance lies around 70% at SPEAR in California, USA [105]. To improve the injection efficiency at the coupling resonance a dedicated effort has to be launched.

During the second beamtime, the program included an optimization campaign for injection efficiency. However, this was not possible due to time constraints and the level of

[2]LOCO-fit model has been provided by J. Keil.

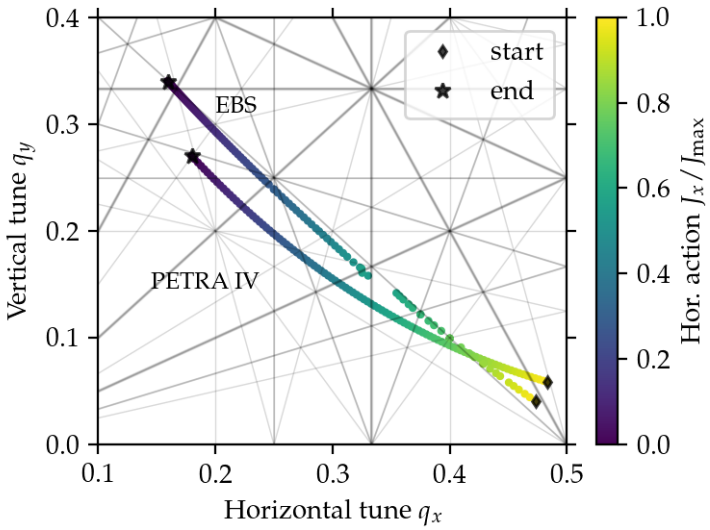

Figure 4.22: Tune excursion comparison of off-axis injected particles in the future PETRA IV storage ring and the state-of-the-art fourth-generation light source at ESRF. Both dynamic apertures are limited by detuning with amplitude, when the horizontal half-order resonance and the vertical integer resonance are approached. $J_{max} = 2.5\,\mu m$ for the ESRF-EBS and $J_{max} = 0.75\,\mu m$ for PETRA IV.

expertise required for machine operation. Additionally, the setup was not fully comparable, as the key component essential for achieving high injection efficiency—the strong detuning with amplitude expected in PETRA IV—was not guaranteed. Consequently, the same experiment was conducted at a fourth-generation light source with similar characteristics.

4.3.3. ESRF-EBS experiment

ESRF-EBS simulation

The same experiment has been pursued at the ESRF-EBS. For this study, one machine development timeslot was granted on the 16th of September of 2024. Since the PETRA IV storage ring is more similar to the ESRF-EBS than to PETRA III, the off-axis injection experiment will deliver more insights into operational considerations. This is exemplified in figure 4.22, where the tunes excursion of off-axis injected particles are displayed. The amplitude detuning coefficients are dominated by octupole corrections and the sextupoles setup. The values obtained by simulation with $(Q_x, Q_y) = (76.16, 27.34)$ and $(\xi_x, \xi_y) = (8.6, 5.7)$ read $(\kappa_x, \kappa_y) = (0.101, -0.115)\ \mu m^{-1}$. Note that the detuning coefficients of PETRA IV are of the same order of magnitude as those of the EBS, with values approximately three times higher. Additionally, the maximum action achieved by PETRA IV is about three times lower than that of the EBS, making both systems well-suited for comparison in terms of detuning with amplitude.

To continue, the same simulation exercise has been repeated with the ESRF-EBS lattice. A sketch of the dynamic aperture and the injected beam are illustrated in figure 4.23. The expected injection efficiency is in excess of 95%. This is a direct result of the injected beam that fits inside the dynamic aperture illustrated as a black curve. At ESRF the injected beam is manipulated such, that the transversal emittances are partially swaped. This directly reduces

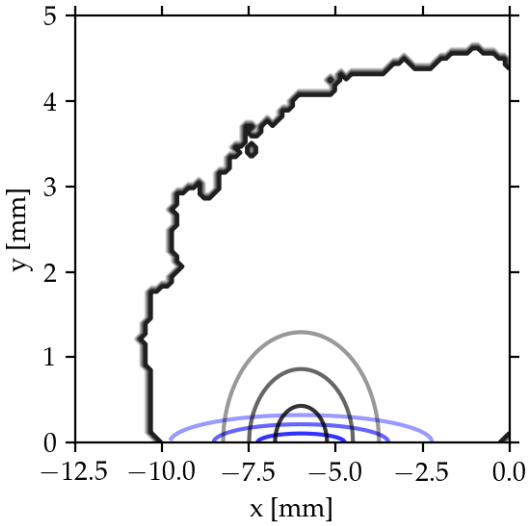

Figure 4.23: Dynamic aperture at injection point of the ESRF-EBS calculated with `Xsuite` [101]. The three rms beam sizes of the injected beam are illustrated as half ellipses in blue. The transversal rms emittances of the injected beam are $(\epsilon_x, \epsilon_y) = (85, 5)$ nm rad. In black, the manipulated beam for injection efficiency enhancement is depicted [106]. The rms emittances are $(\epsilon_x, \epsilon_y) = (30, 80)$ nm rad. The optical functions at injection read $(\beta_x, \beta_y) = (18.5, 2.5)$ m and vanishing $\alpha_{x,y} = 0$.

the horizontal size of the injected beam at the expense of a higher beam size in the vertical plane. The injected beam size of the rotated beam is illustrated as black ellipses in figure 4.23. Although in simulation the expected injection efficiency is high, in operations the efficiency is reduced to less than 80%. The measured dynamic aperture is 20% lower than expected [14].

Experimental results

The machine was set near the coupling resonance by adjusting the quadrupole strengths of the first two families in the arc cells. A few iterations are enough to reach the round beam condition and this is illustrated in figure 4.24. In figure 4.24 a snapshot of the control room is shown, where the machine setup is summarized. The tunes were set to $q_x = q_y \approx 0.25$. The emittances converged to $\epsilon_y/\epsilon_x = 79.5/87.7$, which represent a 90% emittance ratio. The vertical emittance measurement becomes inaccurate for values higher than 40 pm rad, since this range is above the operation expected values[3]. With this setting beam has been injected. The typical injection efficiency for a machine operated near the coupling resonance decreases to approximately 15%. This is illustrated in figure 4.25, where the green curve represents the transmission efficiency from booster to the storage ring. On the same shift the maximum achieved injection efficiency with nominal tunes was in the range of 50% to 60%. Note that these values are a direct consequence of the relatively high injected beam emittance and possibly unknown components in the single-particle non-linear dynamics, that limit the dynamic aperture.

[3]private communication with beam diagnostics expert F. Ewald

Figure 4.24: Snapshot from the ESRF-EBS control room. The application shows a summary of the machine and beam setup.

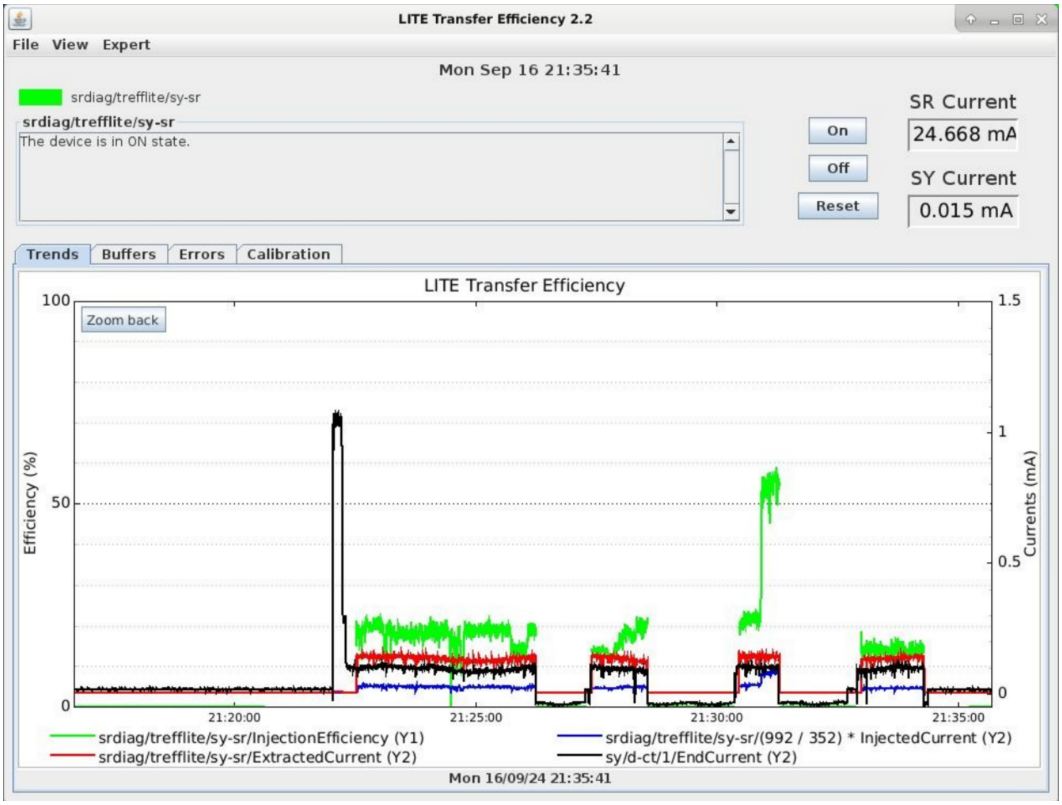

Figure 4.25: Snapshot from the ESRF-EBS control room showing the measured injection efficiency in green. The values at 15% are when the machine was operated at the coupling resonance $q_x = q_y$.

5

Quasi-stable resonance islands

In the previous chapter a thorough discussion of the generation of round beams has been presented. The beam dynamics performance is favorable for many features brought by the round beam operation, especially the lifetime and emittance preservation enhancements. Off-axis injection experimental results have been reported and delivered suboptimal results, which will be later discussed. In this chapter we would like to focus on other interesting result. Simulations have shown, that the generation of resonance islands as illustrated in figure 4.16, is to be expected. The observation in simulation of these islands is surprising and unexpected, since the design of the hybrid multi-bend achromat has especifically strived for cancellation of resonance driving terms by introducing a π-phase-advance between sextupoles [23, 77].

In this chapter we would like to review briefly the conditions known so far for the generation of transverse resonance island buckets (TRIBs) and how they differ from the current simulation results. We then focus on experimental campaigns at ESRF to characterize these islands.

5.1. Transverse resonance island buckets

To continue the discussion of the transverse resonance island buckets, we would like to pickup the concepts presented in Chapter 2 and extend them to include some Hamiltonian mechanics. As we have seen, the motion in an electron storage ring is regular and resembles harmonic oscillations in normalized phase-space. Hence, the motion is linear and the EQoM is governed by the Hamiltonian $\mathcal{H} = -\mu_x J_x$ with a constant phase-advance $\mu_x = 2\pi q_{x,0}$. Here $q_{x,0}$ refers to the fractional part of the value described by equation 2.4. In general though, the Hamiltonian of a particle accelerator can be expressed as

$$H = \bar{h}(J_x, J_y) + h^{(r)}(J_x, J_y, \phi_x, \phi_y), \tag{5.1}$$

where the first term represents the (averaged) integrable part and the second term the resonant part of the transverse motion.

In principle, a Hamiltonian for a particle accelerator can be *a-priori* derived with Lie-algebraic perturbation techniques to arbitrary order, if the settings of the magnets are known [43, 44]. However, to describe the dynamics in fourth-generation electron storage

rings, it suffices to consider

$$\bar{h} = -2\pi \sum_{i\in[x,y]} \left(q_i J_i + \frac{\kappa_i}{2} J_i^2 + \frac{\kappa_i^{(2)}}{3} J_i^3 + \frac{\kappa_i^{(3)}}{4} J_i^4 \right) - 2\pi \kappa_{xy} J_x J_y. \tag{5.2}$$

Note that solving for the angle variable ϕ_x leads to

$$\phi_x =: q_x = \frac{\partial H}{\partial J_x},$$

and yields the results presented in equation 3.3. The amplitude detuning coefficients have been calculated and presented for PETRA IV in Table 3.3. In practice, higher order amplitude detuning coefficients are approximately negligible. For PETRA IV $\kappa_x^{(2)}$, $\kappa_{x,y}^{(3)}$ and $\kappa_{x,y}^{(4)}$ do not play an important role in the dynamics. However it appears that $\kappa_{x,y}$, $\kappa_y^{(2)}$ should still be considered. Furthermore, the resonant part $h^{(r)}$ can be neglected at low amplitudes and when working points are safely far from low order resonances. Resonant Hamiltonians are not exploited in synchrotron radiation light sources, but for one notable exception: at the Berliner Elektronenspeicherring-Gesellschaft für Synchrotronstrahlung (BESSY) in Berlin triple stable orbits [47, 48, 53] are generated by approaching the third order resonance $3q_x = 1$.

In recent theoretical studies the effective Hamiltonian governing the dynamics near this resonance has been identified as [107, 108]

$$\bar{h} = 6\pi \Delta_x J_x + 3\pi \kappa_x J_x^2, \tag{5.3}$$

with the resonant part

$$h^{(r)} = \frac{S}{\sqrt{2}} J_x^{3/2} \sin(3\phi_x + 3\psi_S), \tag{5.4}$$

based on the Hamiltonina proposed in [109]. Here $\Delta_x = q_{x,0} - q_{\text{res}}$ with $q_{\text{res}} \in [1/3, 2/3]$ is the nearest third order resonance. The resonant driving term (RDT) amplitude and phase read

$$S = \Big| \sum_n^N S_n e^{i3\psi_n} \Big|, \qquad 3\psi_S = \arctan\left(\frac{\sum_n^N S_n \sin 3\psi_n}{\sum_n^N S_n \cos 3\psi_n} \right) \tag{5.5}$$

with

$$S_n = \frac{1}{2} \int \beta_x^{3/2} k_2 \mathrm{d}s, \tag{5.6}$$

where ψ_n is the phase-advance to the n-th sextupole. The dummy index n runs over an ordered list of the sextupoles available in the lattice. For PETRA IV considering the nominal working points $(Q_x, Q_y) = (135.18, 86.27)$, chromaticities $(\xi_x, \xi_y) = (8.1, 7.3)$ and with the octupole setup generating the detuning coefficients listed in Table 3.3, yields an RDT with $(S, \mu_S) = (4.33\text{m}^{-1/2}, -0.95°)$.

An important condition for equations 5.3 and 5.4 to be valid, is the proximity of the horizontal working point to the resonance. This constraints $|\Delta_x| < \frac{1}{6\pi}$. For the simulation we have performed $\Delta_x = 0.15\bar{3} \gg \frac{1}{6\pi}$.

Furthermore stable and unstable fixed points can be deduced from equations 5.3 and 5.4. These read

$$J_{x,\pm}^{1/2} = \frac{1}{8\sqrt{2}\pi}\frac{S}{\kappa_x}\left(1 \pm \sqrt{1 - 128\pi^2\frac{\Delta_x\kappa_x}{S^2}}\right). \tag{5.7}$$

The effective Hamiltonian can reproduce quite well the dynamics induced near the third order resonance and has already been systematically characterized experimentally at Cornell, USA [107]. Nonetheless, when the working point is found to be far from the resonance ($|\Delta_x| > \frac{1}{6\pi}$), the description appears to be inaccurate. This is better illustrated with following example. The position of the fixed points at observation point with $(\beta_x, \alpha_x) = (46\text{m}, 0)$ as shown in figure 4.16 as predicted by equation 5.7 read $(J_+, J_-) = (394, 393)$nm. These values are not far off from the simulation results, which have an approximate $J_x = 375\,$nm, nevertheless the prediction given by equation 5.7 is an overestimation.

To investigate further the existence of the resonance islands and characterize their properties an experimental campaign was launched at the ESRF. Technical details of this state-of-the-art facility and its electron storage ring can be found elsewhere [14, 79]. Relevant parameters are summarized in Table 5.1. We describe next the simulation and experimental results.

Table 5.1: Storage ring and beam parameters for experimental investigations at ESRF.

Parameter	Symbol	Value
Circumference	C	844 m
Beam energy	E	6 GeV
Fractional tunes	q_x/q_y	0.24/0.24
Chromaticities	ξ_x/ξ_y	9/9
Equilibrium emittance	ϵ_0	133 pm rad
Damping times [ms]	(τ_x, τ_y, τ_z)	(8.6, 13.2, 8.9)
Eq. momentum spread	σ_p	0.95×10^{-3}

5.2. Simulation results

First, to corrobate the results observed for the PETRA IV lattice, simulations are performed with `pyAT` [110] with the EBS electron synchrotron. A model of the storage ring that includes the magnetic field and misalignment errors has been utilized[1]. With this model particles have been tracked element-by-element only considering the transversal oscillations (4D tracking, longitudinal coordinates frozen). The tunes are matched to $q_x = q_y = 0.21$ and the chromaticities are kept at the nominal values. Particles are launched with different horizontal initial actions J_x and from the simulated oscillations the fractional tune values are recovered. The results are illustrated in figure 5.1, where the strength of the octupoles have been scaled with four different values. The effect on the amplitude detuning coefficients is evident. By turning the octupoles off, namely with relative strength equal zero, the tune with amplitude crosses more promtly the third integer resonance, since the amplitude detuning coefficient increases.

[1]LOCO-fit model has been provided by S. Liuzzo and N. Carmignani.

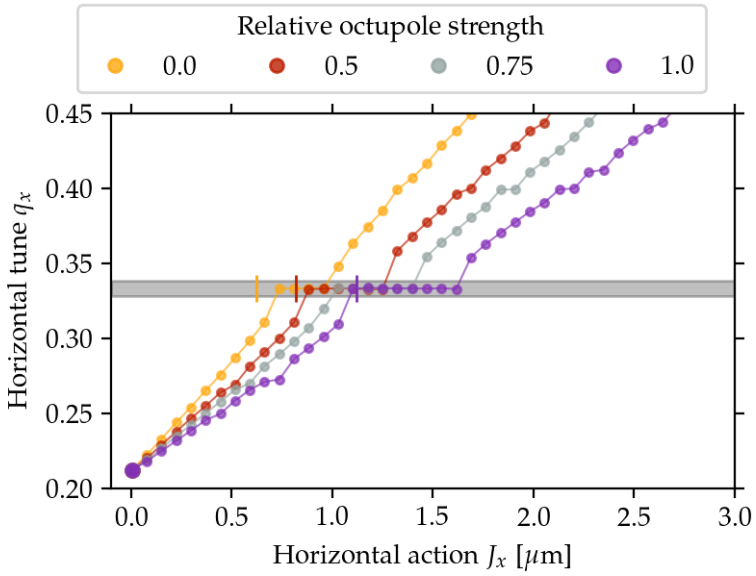

Figure 5.1: Simulated tune dependence with increasing horizontal action at the ESRF-EBS. The tunes have been matched to the coupling resonance $q_x = q_y = 0.21$. Different colors indicate the strength of the octupoles that have been collectively scaled. This has a direct impact on the amplitude detuning coefficient. The grey band accentuates the resonance band where particles get trapped inside a resonance island. The vertical lines show the J_+ prediction from equation 5.7. The detuning coefficients go from $\kappa_x \in [0.1117(2), 0.152(2), 0.201(9)]\mu\text{m}^{-1}$ for the relative octupole strengths of 1, 0.5 and 0, correspondingly. The resonance driving term reads $(S, \psi_S) = (29\text{m}^{-1/2}, 39.5\bar{3}°)$.

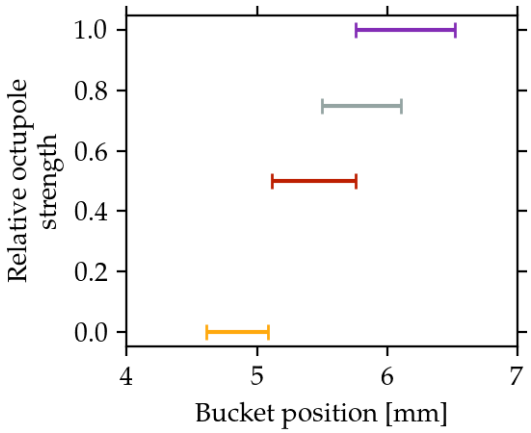

Figure 5.2: Expected bucket positions and widths of the resonance islands at the ESRF-EBS. The tunes have been matched to the coupling resonance $q_x = q_y = 0.21$. The observation point is the injection straigth with $(\beta_x, \alpha_x) = (18.5\text{m}, 0)$. The octupole strength diminishes the detuning coefficient and thus displaces the resonance buckets.

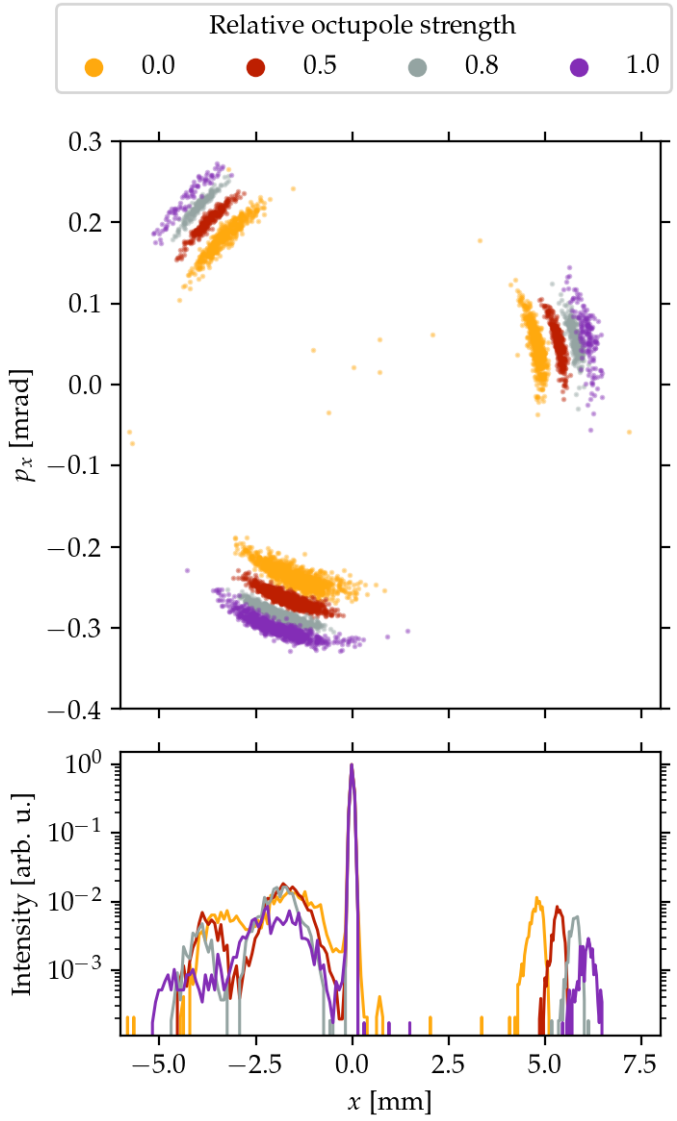

Figure 5.3: Top panel: Particles trapped in resonance islands after 10^4 turns starting from an off-axis injection event. The simulation has been performed with the ESRF-EBS with tunes near the coupling resonance $q_x = q_y = 0.21$. The lower panel illustrates the normalized amount of particles in each bucket. Note that the particles in the core are not shown in the upper panel, only particles in the islands. The observation point is the injection straigth with $(\beta_x, \alpha_x) = (18.5\text{m}, 0)$. The information for four different octupole setups is shown and signalized with different colors.

Notice that the horizontal tune is locked on an action region to the third order resonance. This is due to particles been trapped in resonance islands. The positions of the resonance buckets and their widths are depicted in figure 5.2.

Additonally, a simulation of the off-axis injection has been performed for this setup. For this simulation 10^4 particles have been initialized as a bunch similar to an injected electron bunch coming from the booster. The particles are then tracked for 10^4 turns element-by-element including the effects of synchrotron radiation and quantum excitation. The results are illustrated in figure 5.3. The amount of trapped particles in the buckets ranges from 10% to 23% capture efficiency. This is also illustrated on the lower panel of figure 5.3. The normalized intensity is dominated by particles in the core.

Finally, for this preparatory set of simulations a tune scan has been performed to determine the range in which the resonance islands are expected to be generated. The simulations show that resonance islands are generated within an approximate tune range of $q_x \in [0.18, 0.24]$. The condition $q_x = q_y$ appears not to be related to the generation of the islands. With these results we proceed with the experiment looking for the islands at ESRF-EBS.

5.3. Experiments at ESRF

Multiple experimental campaigns have been pursued at the ESRF-EBS storage ring in Grenoble, France to corroborate the existence of the resonance islands and characterize their properties. Initially, preliminary studies were performed to verify the existence of the islands. This consisted on filling the machine and kicking the beam with different amplitudes in hope to fill the islands with some beam. Following this procedure a movable collimator jaw would be closed and current loss was expected from collision with trapped particles in the islands. These studies led to null results. Possible explanations included an overestimation of the lifetime of particles trapped in the island. The collimator jaw is driven by a precise but slow motor, which can take anywhere from a few tens of seconds to a minute to fully close. Simulations with PETRA IV and ESRF-EBS have only been performed with a few hundreds of thousands of turns, corresponding to few hundreds of milliseconds.

Henceforth a double kick technique was pursued, which consisted of kicking the beam consecutively more than once with a pause between kicks of 250 ms. The expectation was, that by kicking the beam with sufficient strength, particles would reach the islands and some beam would be captured. Particles not being captured would damp to the core. The consecutive kick would then result in particle loss of captured particles in the islands, since the kick strength would lead them to leave the edge of the dynamic aperture. Simultaneously, particles in the core would refill the islands and hence particle losses should be measurable and proportional to the capture efficiency and number of consecutive kicks. Observations of current loss due to trapping in resonance islands were made in the shift of September 9th, 2024. Experiments conducted on December 3rd, 2024 to reproduce the previous observations lead to null results.

Finally, an attempt to characterize and either corroborate or defy the existence of the islands observed in simulation was performed on January 27th, 2025. In this shift we conclusively gathered enough experimental data to corroborate the existence of quasi-stable resonance islands in fourth-generation light sources. Next we describe the method used to diagnose reliably the generation of the islands and the results of the last experimental shift.

5.3.1. Experimental setup and method

Experiments were conducted at ESRF during a machine development timeslot with 6 GeV electron beams with $I_{\text{tot}} = 1$ to 5 mA. The storage ring was filled with a bunch train occupying one-third of the available rf-buckets in a uniform filling pattern. The tunes were matched to $q_x = q_y = 0.24$ and the chromaticity was left at nominal values. The octupole strengths were scaled to half of their nominal strength to bring the islands closer to the core.

To infer the beam dynamics, the electron beam is kicked using four magnet kickers and its free oscillations are recorded with the 320 available beam position monitors (BPMs). The BPMs are synchronized and set to turn-by-turn fast acquisition mode. The BPMs are standard capacitive button pickups, whose sum-signal is proportional to the beam current. A step to retrieve the beam centroid position from the difference signal is implemented at a pre-process level. Data delivered from the acquisition system is beam centroid position and sum signal.

Further, the kickers pulse follow a quarter-sine-wave and has a rise time of 70 μs, corresponding to approximately 25 revolutions of the electron beam. The ramp amplitude can be set independently and thus the kicker pulses are pre-calculated, such that the beam reaches arbitrary points in phase-space. The effect of each single kicker and the combined effect to reach arbitrary points in phase-space is illustrated in figure 5.4. To measure the lifetime the beam is kicked with kicker **K3** (red triangle in figure 5.4) to fill the islands with beam. The beam is kicked until beam loss is observed, thereby ensuring that the beam reached the islands. Additionally, data acquisiton campaigns where the phase-space is scanned over seven angles in the range $\phi_x \in [-\pi/2, \pi/2]$ with steps of $\pi/6$ rad are performed. The amplitude of the kicker pulses is scaled with a global parameter. This parameter controlling the amplitude is scanned in ten steps from 0 to 1, with one being the strength necessary to reach the islands in simulation.

5.3.2. Experimental results

An exemplary signal recorded at one BPM during the experiment is shown in figure 5.5. Here the ramp-up of the kickers is distinguishable and the free oscillations of the beam that follow. The turn-by-turn data was fitted to a function of the form (see e.g. [111])

$$\langle x \rangle = A_0 \exp(-Dt) \sin(2\pi q_x t + \phi_0) + x_0, \tag{5.8}$$

to recover the tunes and initial amplitudes. The beam centroid oscillation signal decays fast due to the strong decoherence triggered by high chromaticity, non-linear dynamics and less dominant in our experiment, synchrotron radiation damping [111]. The tune recovered by the fit is compatible with the peak of the discrete Fourier transform (DFT). As the kicker strengths were increased by making used of a global scaling parameter, the horizontal tunes increased as well. Sample data of the amplitude detuning observed at one BPM is illustrated in figure 5.6 on the left panel. When the amplitude of motion is sufficient, particles reach the third order resonance and are trapped in the islands. This process has a distinct trace, which is recognizable in the recorded data of all BPMs. Three long stading traces are observed as shown in the right panel of figure 5.6. These are determined by the amount of charge captured in the resonance islands and the position of the buckets. Notice that the traces do not decay due to decoherence, nor due to synchrotron radiation damping during the first 10^4 turns.

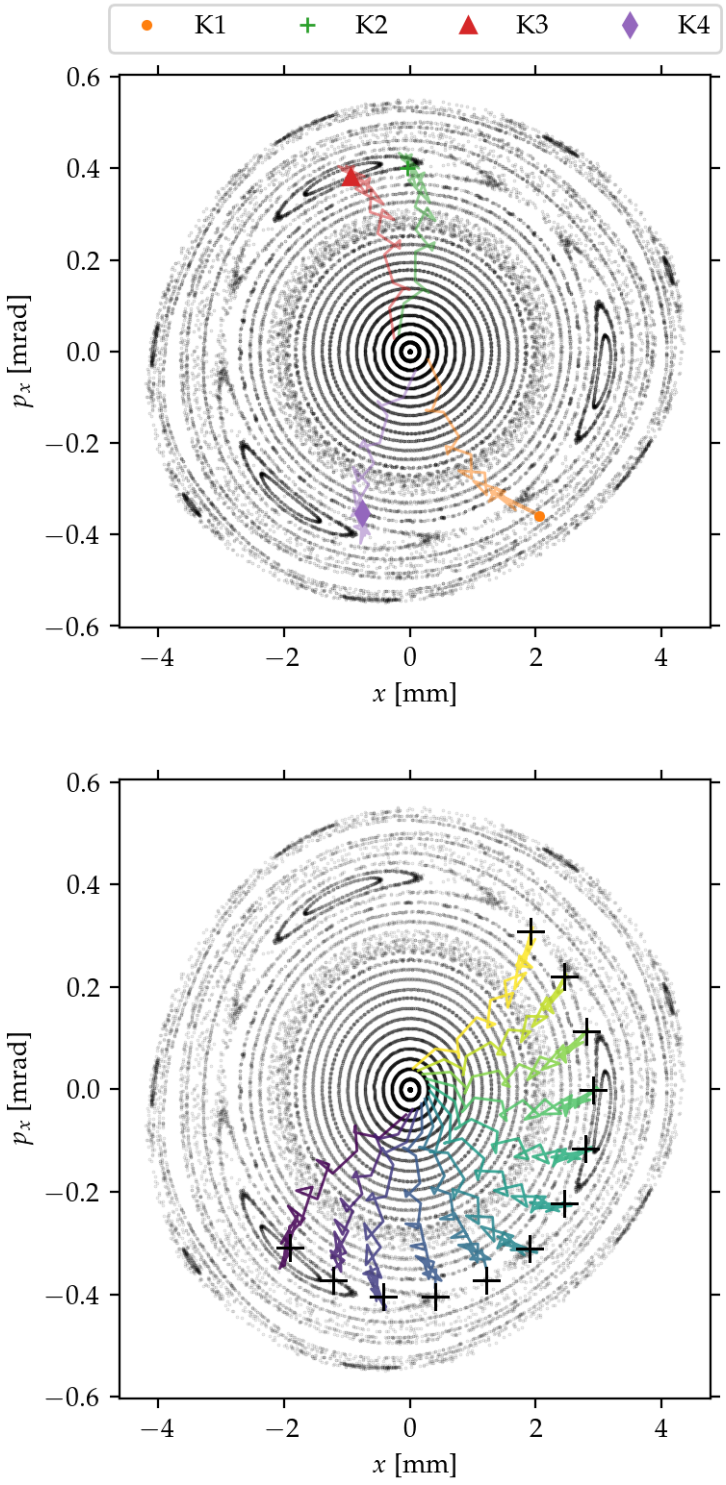

Figure 5.4: Top: Simulated effect on the beam centroid with single kickers ramped-up in 25 turns. The four different kickers available are indicated with different colors and markers. Bottom: Illustration of the pre-calculated kicker ramp effect on the beam centroid from simulation. The four kickers are used to place the beam in arbitrary amplitudes and phases by varying the kicker strengths. Each color represents a setting for the kickers. The curve starting from the center represents the centroid position over the kicker ramp with a duration of 25 turns. For the determination of the kicker strengths a simplex minimizer was utilized. The black crosses indicate the chosen points in phase-space for the sampling and are used as objectives in the minimizing procedure. In the background the simulated phase-space portrait is depicted to aid the identification of the islands. The observation point is the first insertion device straight (ID05) after injection with $(\beta_x, \alpha_x) = (7.14\text{m}, 0)$.

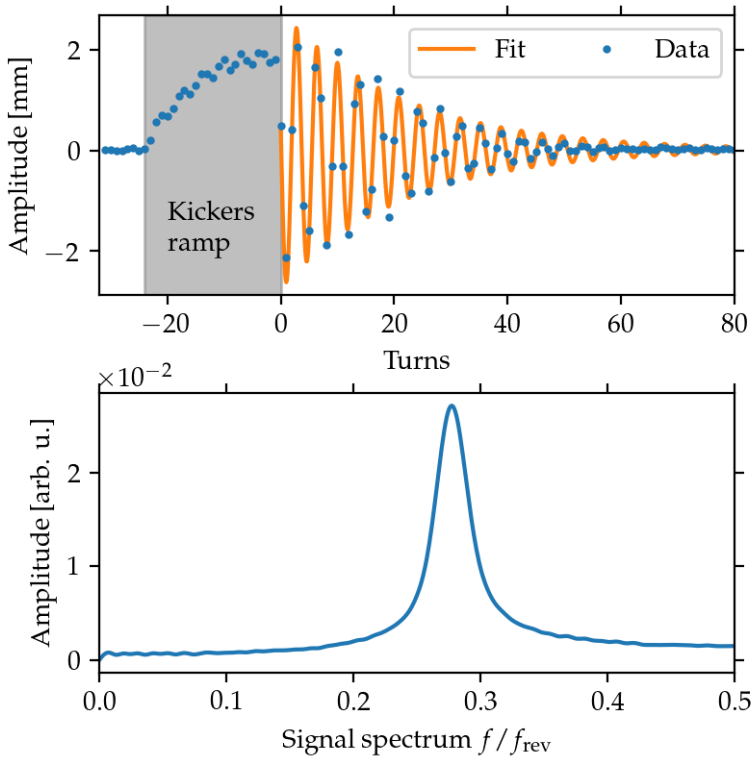

Figure 5.5: Top panel: Exemplary turn-by-turn recorded data from one BPM. The kickers ramp duration is highlighted with a grey shaded area. The solid line illustrates a fit result to the free beam oscillations with an exponentially decaying sine-wave. On the lower panel the DFT of the free oscillation centroid signal (after the shaded grey area) is shown.

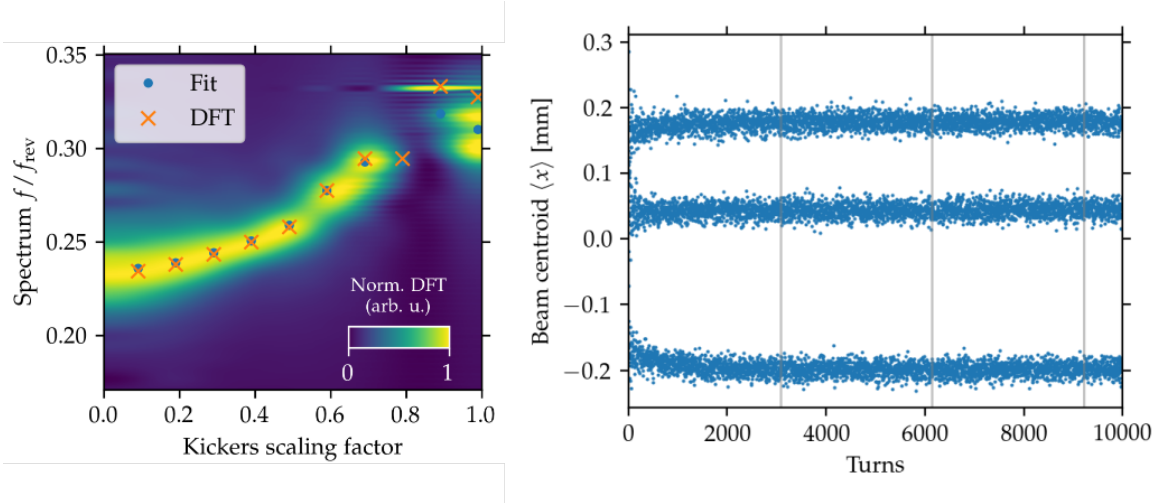

Figure 5.6: The left panel shows the DFT of exemplary recorded signals at one BPM as a function of the kicker strengths. The blue dots indicate the tune values extracted from the fit as shown in figure 5.5. The orange crosses indicate the maximum of the spectrum of the first 128 turns after the kick. Notice that when the amplitude scaling parameter reaches unity, the spectrum sharply peaks at the third order resonance. On the right panel an exemplary shot with 10^4 recorded turns is shown. This is the case where the resonance buckets are filled with electrons. The vertical gray lines indicate three synchrotron radiation damping times.

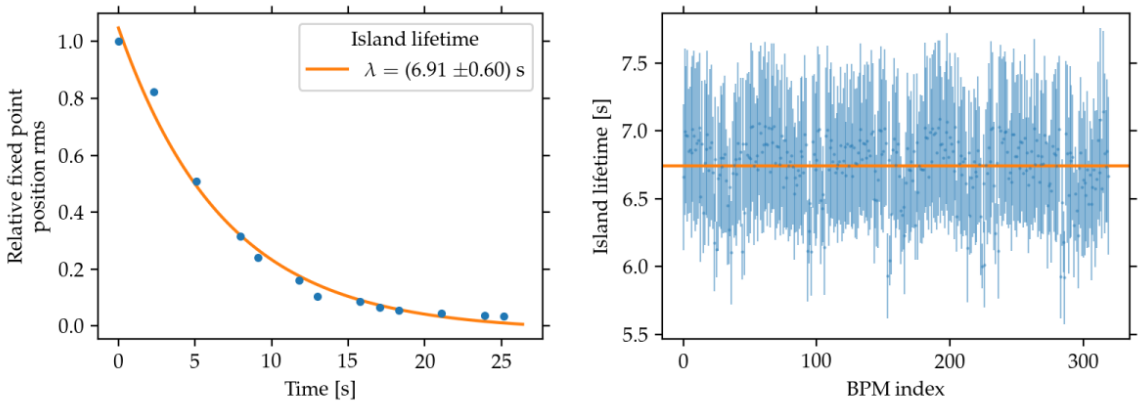

Figure 5.7: Island lifetime measurement. On the left panel exemplary data of the relative rms fixed point position is displayed as a function of time. The blue dots represent the measured data and the orange solid line is an exponential decay fit with a lifetime indicated in the figure. On the right the island lifetime recovered from each of the 320 BPMs is shown. The orange horizontal line indicates the mean value.

Trapped particles lifetime

To determine the islands lifetime, the beam was kicked with one single kicker to fill the islands and turn-by-turn data was recorded over a course of approximately 30 s. Since the separation of the three traces in the recorded data is proportional to the number of particles in the islands, the three traces will converge to the center as particles escape the buckets. Simulation shows that particles leaving the bucket will simply decay into the core. Since the position of the islands rotate along the machine following the phase-advance ψ, the measured trace at each BPM is different. The rms of the fixed point is proportional to the amount of particles captured in the island, thus it is used as a proxy to measure the capture lifetime. The rms position of the fixed points observed at one BPM is illustrated in figure 5.7. An exponential decay was fitted to the signal to determine the lifetime as it is shown in the example. This was repeated for each BPM and the results are illustrated in the right panel of figure 5.7. The measured lifetime reads

$$\lambda = 6.74\text{s} \pm (0.23_{\text{stat.}} + 0.03_{\text{sys.}})\text{s}.$$

Simulations were performed to determine the lifetime of the captured particles with `pyAT` [110] by tracking an ensemble of 10^4 particles initialized inside the bucket. The particles were tracked for 2×10^5 turns element-by-element including the effects of synchrotron radiation and quantum excitation. The simulated particle rate leaving the bucket leads to a trapping lifetime of 63 s and is an order of magnitude higher than the measurement.

Amplitude detuning

With the recorded data it is possible to estimate the amplitude detuning coefficient κ_x. The amplitude from the fit described by equation 5.8 is weighted with the inverse of the squared-root of the β-function at each BPM position and then divided by the squared-root of two. The square of this value is then used to estimate the horizontal action J_x. The tune is recovered both from the fit and the DFT.

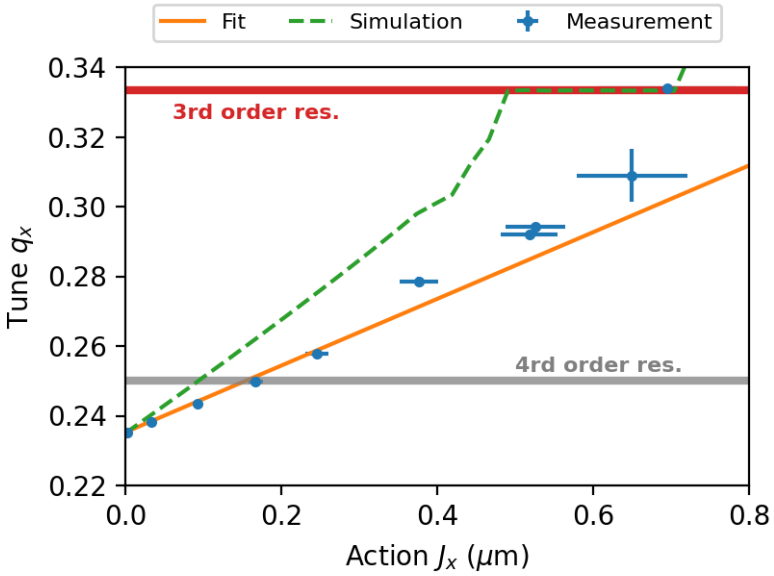

Figure 5.8: Exemplary data set illustrating the measured tune as a function of the estimated horizontal action.

The full data set is used and the amplitude detuning coefficient reads

$$\kappa_x = 100\text{mm}^{-1} \pm (9_{\text{stat.}} + 2_{\text{sys.}})\text{mm}^{-1}.$$

An exemplary set of measurements is illustrated in figure 5.8. The simulation with the perfect lattice with the same octupole settings yields $\kappa_x = (162 \pm 2)$ mm^{-1} and is higher than the experimental value. This discrepancy can be understood from following considerations: the estimation of the measured action with the fit function exhibits a high sensitivity on the amount of points utilized. Thus, this can lead to an over-estimation of the initial action and therefore the amplitude detuning coefficient is lower than expected. Some systematic discrepancies are evident for high-amplitude oscillations in figure 5.8. These are a result of non-linear sensitivity at high-amplitude of the BPMs[2]. Hence, a dedicated measurement campaign should be pursued. More data needs to be recorded in order to generate sufficient statistics. This information is necessary to properly estimate the amount of data to be used in the fit, aided with conventional tests such as χ^2-test to determine fit parameters. Previous measurements show a better agreement with simulation results [112]. In [112] a dedicated measurement to characterize the non-linear dynamics is reported.

Phase-space reconstruction

To finish this chapter we would like to show some reconstructed centroid motion in phase-space with the two BPM technique. With the transfer matrix formalism (see e.g. [29]) it is easy to show that given two BPM position readings x_1, x_2, the momentum of the particle at the first BPM is given by

$$p_x = \frac{x_2 - r_{11}x_1}{r_{12}}, \tag{5.9}$$

[2]private communication with BPM expert Kees Scheidt

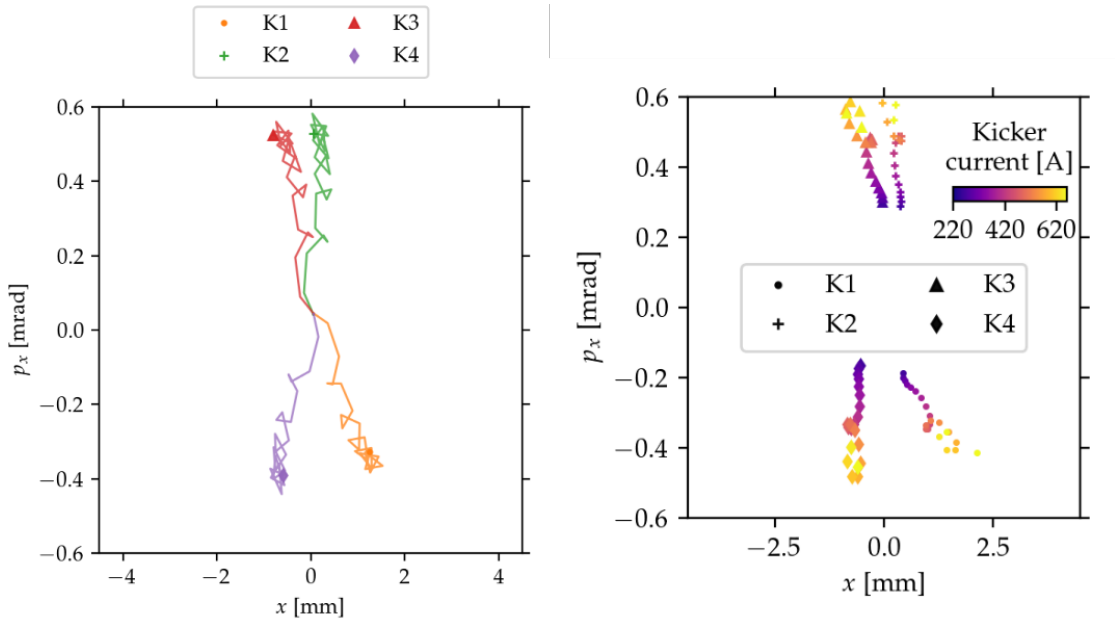

Figure 5.9: Reconstruction of the single kicker effect on the beam centroid with experimental data of two adjacent BPMs. On the left the beam position in phase-space over the 25 turn ramp-up of four different kickers is depicted. The final position of the beam centroid is illustrated on the right for different kicker currents for the four available kickers. In the experiment the kicker current was set from 220 A to 650 A. The beam centroid has been traced down to the first insertion device straight (ID05) after injection with $(\beta_x, \alpha_x) = (5.37\text{m}, 0)$. The optical functions are recovered from a model including the misalignment and field errors.

where the transfer matrix elements r_{11} and r_{12} are given by

$$r_{11} = \sqrt{\frac{\beta_2}{\beta_1}}\left(\cos(\Delta\psi) + \alpha_1 \sin(\Delta\psi)\right) \tag{5.10}$$

$$r_{12} = \sqrt{\beta_2\beta_1}\sin(\Delta\psi) \tag{5.11}$$

where β_1, β_2 are the β-functions at the first and second BPM respectively. $\Delta\psi$ is the phase-advance between these two points and α_1 represents the optical function at the first BPM. With these equations and by taking advantage of the very well corrected linear optics at ESRF we reconstruct the phase-space trace of the beam centroid during the ramp-up of the kickers. In figure 5.9 the effect of single kickers on the beam centroid is illustrated. The four different kickers are indicated in different colors and the trace indicates the 25 turns of the kicker pulse ramp-up. The reconstructed beam excursion in phase-space is compatible with simulations results shown in figure 5.4 top panel. Additionally the data of the phase-space "painting" with the four available kickers was performed as illustrated in figure 5.4 in the lower panel. The recontructed traces of the beam centroid with experimental data is shown in figure 5.10 and agree well with the simulation results. Note that the data recorded for angles $5\pi/6$ and π display beam capture in resonance islands. All the other probed angles did not reach the third order resonance. Further investigation of these results is ongoing and a publication will be pursued.

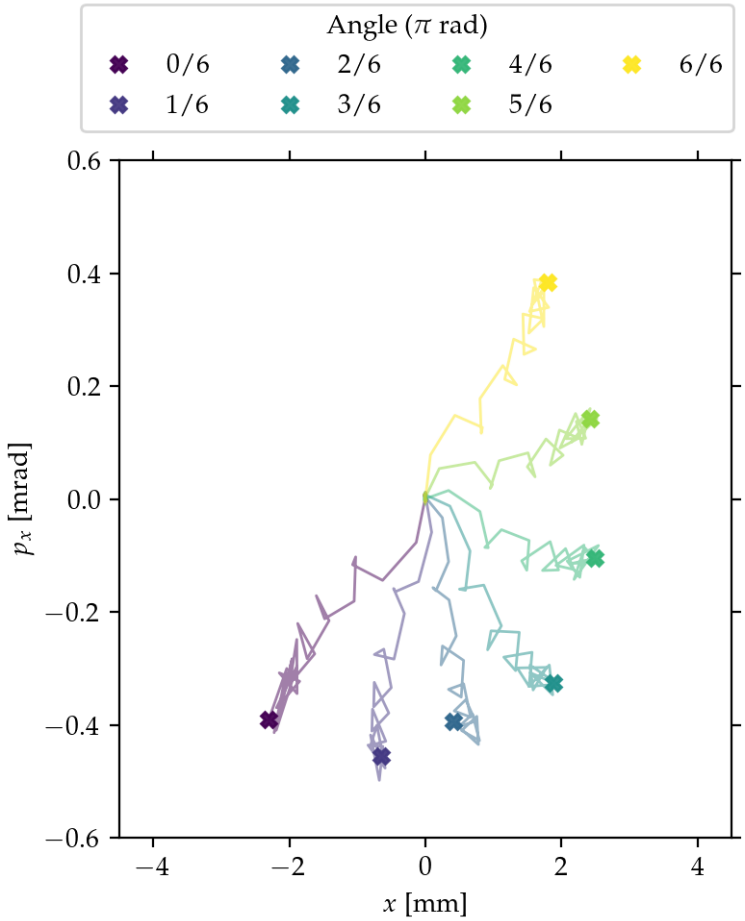

Figure 5.10: Reconstructed centroid trace during the kicker ramp-up from turn-by-turn data for the phase-space scan experiment. The beam centroid has been traced down to the first insertion device straight (ID05) after injection with $(\beta_x, \alpha_x) = (5.37\text{m}, 0)$. The optical functions are recovered from a model including the misalignment and field errors.

6

Resonant slow extraction from DESY IV

To conclude the investigations, another parametric resonance in the PETRA IV injection chain is exploited. The motivation of these studies originate from the lack of integration of the test beam facility at DESY [94] in the PETRA IV project. This unique facility offers multi-GeV electron-positron beams to users, primarly to the high energy physics community for the test of detector technologies. The generation mechanism of these beams runs parasitically to the DESY II booster operation. This is done by introducing a 5 µm carbon wire in the way of the circulating electron beam prepared for PETRA III. With the planned upgrade of the booster ring DESY IV, an alternative extraction mechanism to deliver beams to the test facility has been proposed [24]. This comprises a novel resonant slow extraction approach, that brings the horizontal working point of the machine near the third order resonance $3q_x = 1$ to generate a known phase-space structure. By exploiting the equipotential lines of the motion induced, the resonant slow extraction has been evaluated for the two candidate lattices presented in Chapter 3.

Moreover, resonant slow extraction techniques from synchrotrons are widely employed to deliver a variety of beams, typically for fixed-target experiments. These methods could potentially expand and exploit the full capabilities of an electron test beam facility. Additionally, by equiping the extraction setup with all the feedback and feedforward control systems available, the extracted beam can be tailored exactly to the needs of multiple potential users. Intensity regulated beams can have a dynamic range of many orders of magnitude, typically from 10^4 to 10^{10} particles per extraction cycle with extraction lengths ranging from tens of milliseconds up to hundreds of seconds. The flexibility offered is tailored to the users needs.

Resonant slow extraction schemes make use of an active and controlled reduction of the DA by operating the machine near a parametric resonance. As a result, particles can be driven into unstable motion in a controlled manner, facilitating their easy ejection into an extraction channel [49, 50, 51, 52]. In recent variations of the slow extraction method the third order resonance has been established as the standard working point for synchrotron facilities. This is mostly due to the well established theoretical description of the dynamics given by the Kobayashi Hamiltonian [113].

The Kobayashi Hamiltonian has the form

$$H_{\text{Kobayashi}} = \bar{h} + h^{(r)}, \tag{6.1}$$

and represents a special case of the Hamiltonian previously discussed in Section 5.1. In

equation 6.1 $h^{(r)}$ is given by equation 5.4 and $\bar{h}$ is described by equation 5.3 in the limit of $\kappa_x \to 0$.

This reads

$$H_{\text{Kobayashi}} = 6\pi\Delta_x J_x + \frac{S}{\sqrt{2}} J_x^{3/2} \sin(3\phi_x + 3\psi_S). \tag{6.2}$$

Thus, the resonance drivers are sextupoles and induce the resonance driving term S described by equation 5.5. The control of the amplitude and phase (S, ψ_S) can be achieved by making use of the sextupoles dedicated for chromaticity correction. Alternatively dedicated sextupole families can be installed at dispersion-free regions, thereby facilitating direct control of S without influencing the chromaticity settings. For example, given an objective RDT amplitude S with phase ψ_S, then the strength of the two harmonic sextupoles S_1, S_2 read

$$\begin{pmatrix} S_1 \\ S_2 \end{pmatrix} = \frac{S}{\sqrt{1 + \tan^2 3\psi_S} \cdot \sin 3(\psi_1 - \psi_2)} \begin{pmatrix} \sin 3\psi_2 - \tan 3\psi_S \cdot \cos 3\psi_2 \\ \tan 3\psi_S \cdot \cos 3\psi_1 - \sin 3\psi_1 \end{pmatrix}. \tag{6.3}$$

In equation 6.3 ψ_1, ψ_2 represent the phase advances at the position of the harmonic sextupoles and the normalized sextupole strengths are given by

$$S_{1,2} = \frac{k'_{1,2} L}{2} \beta_x^{3/2}, \tag{6.4}$$

where k' are the sextupole strengths and β_x are the optical functions at the position of the harmonic sextupoles as well.

Furthermore, the rate at which particles are extracted depends on how the beam is brought to meet the resonance condition. In recent decades, major improvements have been made in the capability to control the extracted particle rate, largely due to applications in light ion therapy [114, 115] for tumor irradiation. Therefore, an extensive set of tools has been made available for the radio frequency knock-out (RF-KO) scheme [116] to precisely control the rate of slowly extracted ions, predominantly protons, $^4He^{2+}$-ions and $^{12}C^{6+}$-ions. This is achieved by shaping the excitation waveform used for extraction and active control of the excitation strength with feedback and feedforward loops [117, 118, 119, 120, 121, 122, 123, 124]. In RF-KO extraction the betatron motion is actively stimulated, while the optics settings are left constant. Similar to the scheme described in Chapter 4 in Subsection 4.1.2, the beam emittance is blown-up in a controlled manner.

Slow resonant extraction schemes are widely used in facilities mainly focused on the preparation of hadron beams, but is rarely available at electron synchrotrons. The only facility offering a resonant slowly extracted electron beam is Elektronen-Stretcher-Anlage (ELSA) at Bonn [125]. For this reason, the inherent properties of low-emittance electron machines have been seldom discussed in the context of resonant slow extraction. One of the main differentiators between hadron and low emittance electron synchrotrons is the strength of the detuning coefficient κ_x. A common assuption is that κ_x is negligible such that the Kobayashi Hamiltonian governs the dynamics. This would be a valid assumption for third-generation synchrotron light sources.

Therefore the possibility of slowly extracting a high-quality electron beam from the low-emittance booster ring DESY IV is explored. To set up the slow extraction optics a non-negligible κ_x is considered, and thus stable transverse resonance island buckets (TRIBs)

are generated. By slowly pushing particles to the external islands it is demonstrated that an extraction efficiency in excess of 92% with a 100 µm thick effective septum blade can be achieved. This uncommon optics setup is motivated by the fact that in the low emittance lattices of DESY IV the usual resonant slow extraction optics was not attainable without turning off the chromatic sextupoles. Due to the expected equilibrium rms momentum spread, the correction of chromatic tune spread is necessary to avoid the crossing of low order integer resonances (see Table 3.5). This is a common characteristic of modern low emittance booster rings, fourth-generation light sources and very large hadron machines.

While the design of resonant slow extraction schemes have been extensively discussed in previous studies (e.g. [126, 127, 128, 129]) making use of the established theoretical tools, slow extraction with TRIBs optics has been only very recently considered [24, 130, 131]. The generation of TRIBs is a relatively new scheme that has been exploited at BESSY II in Berlin [47], as previously mentioned. This precursor led to succesful efforts to establish a reliable theoretical framework [107, 108], which has been systematically characterized in experiments at the Cornell Electron Storage Ring (CESR) located in New York, USA [107, 132]. Moreover, within the resonant slow extraction community the generation of TRIBs has been utilized but is referred conceptually as separatrix folding. The use of octupoles is introduced to generate a non-negligible amplitude detuning coefficient κ_x and the direct application is the minimization of activation of components in the extraction channel [133, 134]. The study of TRIBs near a fourth order resonance have been intensively studied in the last couple of decades for the purpose of splitting hadron beams [45, 46], but find no application in the context of slow extraction.

An extensive discussion of the different realizations of resonant slow extraction assuming the Kobayashi Hamiltonian governs the dynamics, can be found e.g. in [126, 127, 128, 129]. Here the discussion is confined to the design of a slow extraction with the RF-KO scheme combined with TRIBs generation. In the following sections the results presented in [24] are summarized.

6.1. Optics setup and slow extraction

To setup the slow extraction optics the horizontal working point is brought near the third order resonance $3q_x = 1$. Under this premise the Hamiltonian that effectively describes the particle dynamics has been introduced in Chapter 5 and is described by equations 5.3 and 5.4. For the design of the extraction optics a pair of harmonic sextupoles are installed in a dispersion free section to allow for full control of the resonance driving term described by equation 5.5. Then the strength of the harmonic sextupoles is given by equation 6.3. With this addition it is possible to generate transverse resonance island buckets, which are illustrated in figure 6.1 in the six-fold symmetric lattice. For the eight-fold symmetric lattice the introduction of an octupole is imprecendible to generate the islands. The octupole serves as a degree of freedom to level the amplitude detuning coefficent κ_x to arbitrary values. In this case, the position of the unstable and stable fixed points predicted by equation 5.7 do not agree with the results obtained by tracking.

As mentioned before, the transverse resonance islands can be generated without the introduction of dedicated harmonic sextupoles, but the design philosophy followed a minimal intervention spirit of the injector chain. Harmonic sextupoles serve as separated elements in

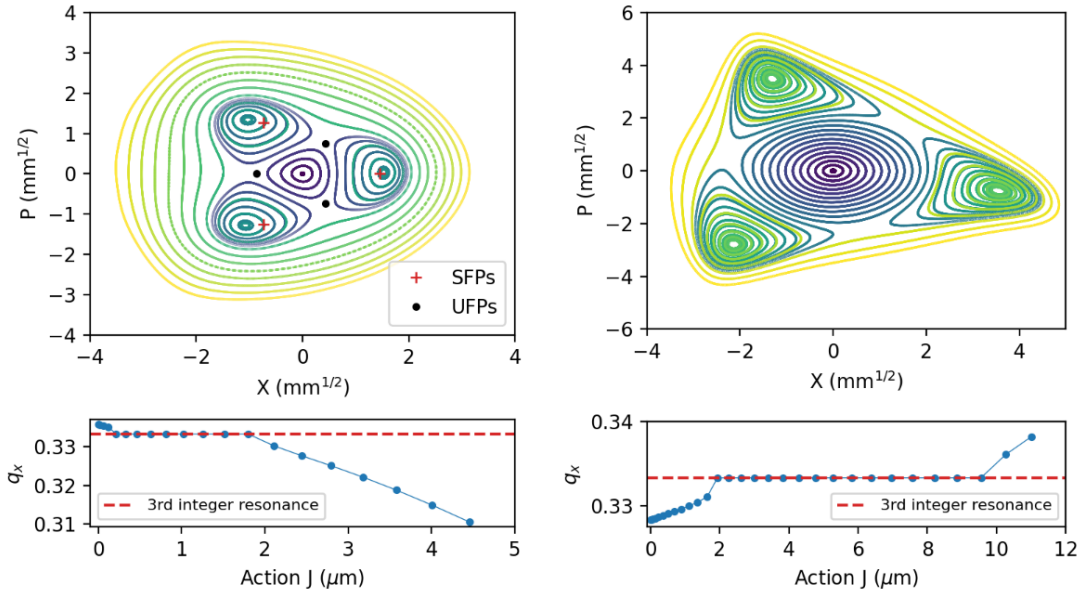

Figure 6.1: Phase space portrait of the optics setup for resonant slow extraction. On the left the results for the former six-fold symmetric DESY IV lattice is shown (see figure 3.11). The lower panel shows the horizontal tune as a function of action. The stable/unstable fixed points (S/UFPs) from equation 5.7 are indicated as red/black crosses/points. On the right the same information is illustrated but simulations are performed with the eight-fold symmetric DESY IV lattice (see figure 3.12). Both pictures are taken from [24].

the booster, that aid the separation of the operation of the booster ring between preparation of bunches for PETRA IV and serving the test beam facility with slowly extracted beams. For the latter the operation relies on powering the harmonic sextupoles with a longer cycle, where it is expected, that a flattop is included when the extraction takes place. Additionally, this simplifies the control of the amplitude and phase of the resonant driving term.

To find an optimal working point for the slow extraction a parameter scan has been performed such that the tune q_x and the resonance driving term S (see equation 5.5) are varied. Simulations show that by varying these two parameters the amplitude detuning coefficient κ_x changes as well. The dependence of κ_x on S can be described by a polynomial of second order [135] for fixed q_x. Essentially, the criterium to find the optimal parameters (q_x, S, κ_x) relied on an *ad-hoc* consideration: the central bucket should be wide enough to allow space for a 20 nm rad 6 GeV to be stored. The position of the high amplitude resonant buckets are used as a guideline that determines the optimal distance to the electronstatic septum.

After optimal optics is recognized, then the extraction scheme is simulated as follows: an ensemble composed of 10^5 particles is initialized with the equilibrium parameters described in table 3.5 in the central bucket. Then an excitation signal is utilized to drive the betatron oscillations to slowly bring particles to the edge of the central bucket. The excitation signal for this numerical simulation is an amplitude modulated double sine-wave of the form

$$V(t) = A(t)S(t), \tag{6.5}$$

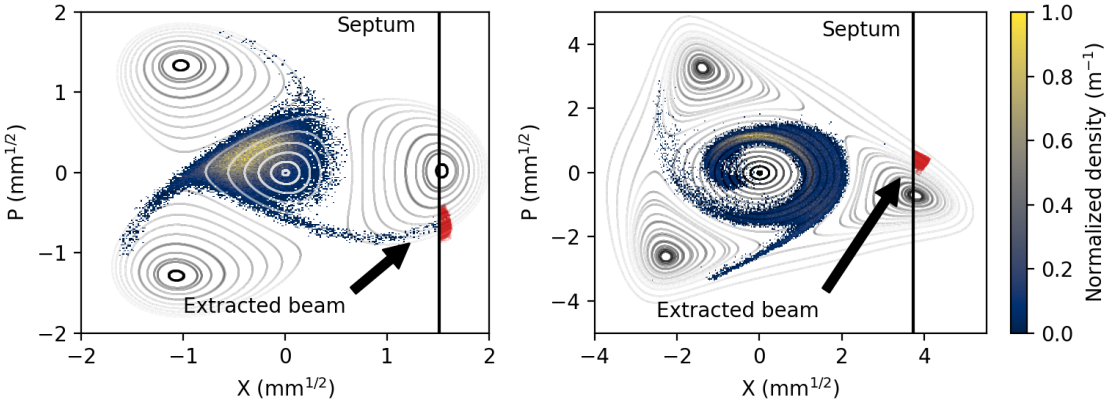

Figure 6.2: Particle distribution snapshot during slow extraction process. The betatronic motion of particles is stimulated resonantly with an external exciter. Particles that reach the edge of the central bucket follow the equipotential lines around the external buckets until they reach the septum. Left panel shows the extraction procedure in the six-fold symmetric lattice, whereas on the right the eight-fold symmetric lattice is depicted. Equipotential lines are plotted in the background to guide the eye. Particles whose amplitude reach the septum position are considered extracted and signalized in red right of the septum. Picture is taken from [24].

with

$$S(t) = A_1 \sin(2\pi Q_1 f_{\text{rev}} t) + A_2 \sin(2\pi Q_2 f_{\text{rev}} t), \tag{6.6}$$

$$A(t) = U_1 \exp\left(\frac{t}{\tau_1}\right) + U_2 \exp\left(\frac{t}{\tau_2}\right). \tag{6.7}$$

Q_1 represents a tune value that controls the diffusion rate of the stored beam, while Q_2 can be associated with a tune that controls the escape rate from the central bucket. The amplitude curve is introduced to counteract the decaying nature of diffusive phenomena, where $\tau_{1,2}$ are the expected timescales of the competing processes. The parameters $(Q_{1,2}, A_{1,2}, U_{1,2}, \tau_{1,2})$ have been found *ad-hoc* with the objective to generate a flat extraction rate profile. No sophisticated method has been utilized to determine optimal parameters, since there are no specifications for the extracted beam quality. The study is concentrated in establishing and exploring the concept for future low emittance booster rings.

Simulations have been performed with the effects of synchrotron radiation and quantum excitation in `Xsuite`. To simulate the effect of the extraction septum an aperture limitation has been introduced. Particles whose amplitude exceeds the horizontal position of the septum would be directed to the extraction channel, thus further tracking is not necessary. A snapshot of the slow extraction process is illustrated in figure 6.2.

Moreover, an important quantity in this context that is indicative for guaranting an enhanced extraction efficiency from the optics perspective is the so called spiral step Δx_{spiral}. The spiral step represents the increase or decrease in oscillation amplitude after three consecutive turns of a particle

$$\Delta x_{\text{spiral}} = x_{n+3} - x_n. \tag{6.8}$$

For an efficient extraction, the spiral step should be maximized at the position of the septum blade that redirects the particles towards the extraction channel. In the conventional resonance

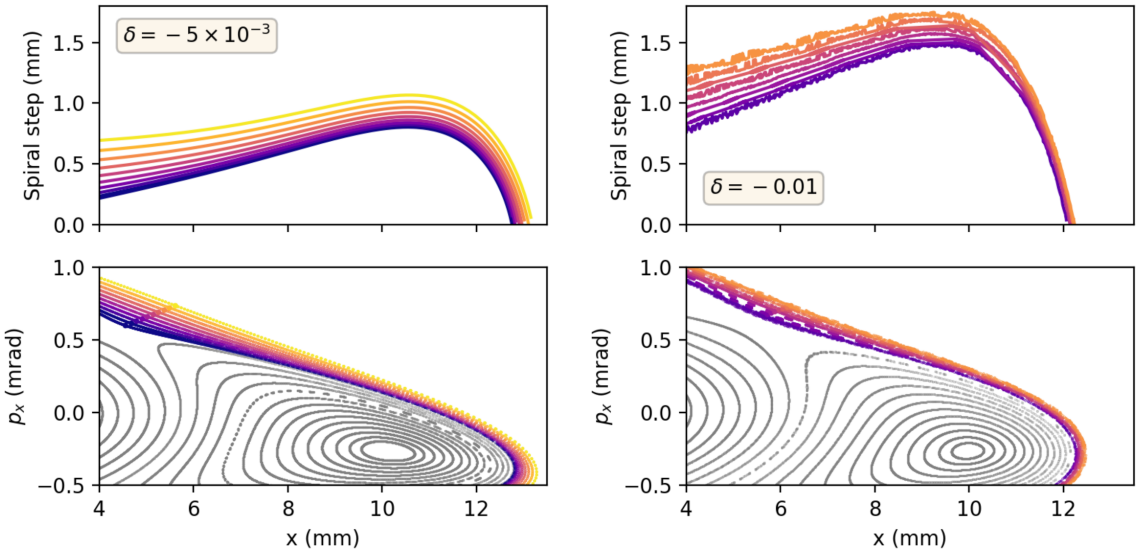

Figure 6.3: Spiral step of particles leaving the central bucket for two different tune settings in the eight-fold symmetric DESY IV lattice. δ represents the horizontal tune distance to the resonance $\Delta_x = q_{x,0} - q_{\text{res}}$ in equation 5.3. Picture is taken from [24].

extraction, where the Kobayashi Hamiltonian governs the dynamics, the spiral step can be in the order of a few centimeters. This is due to the fact that extracted particles follow unbounded motion and therefore their spiral step increases very fast. For the optics that we are considering the motion is still bounded, as particles are trapped by the resonance islands and synchrotron radiation damps the motion towards fixed points. Thus, an overall spiral step reduction is to be expected. The spiral step for two different extraction optics is illustrated in figure 6.3. Typical electrostatic septa have a thickness between 30 and 100 µm. Therefore a spiral step of 1 mm is enough to ensure that particles jump over the septum blade.

6.2. Extracted electron beam and extraction efficiency

Important figures of merit to evaluate the quality of the extraction scheme comprise typically the extraction efficiency and extracted beam parameters. In figure 6.4 an exemplary extracted electron beam is illustrated on the right. On the left an extracted particle count, also known as spill with a duration of 100 ms is shown. The intensity of the extracted particle rate as well as the duration of beam delivery can be extended by modifying the excitation signal described by equation 6.5. The extracted particle count is recovered from simulation results, by computing the relative extracted rate and then by multiplying the number of particles expected in the bunch. The number of particles per bunch in this case is assumed to be $N_p = 6.24 \times 10^7$. Usually flat spills are preferred for numerous applications, but at this stage in the concept study this has not been specified.

On the right side of figure 6.4 the rms emittance is 13 nm rad and has an overall tilt of 200 µrad, which is beneficial for the extraction efficiency. To evaluate the extraction efficiency tentative specifications have been made regarding the extraction channel, the electrostatic and magnetostatic septa. First, it is assumed that the available length of the extraction segment

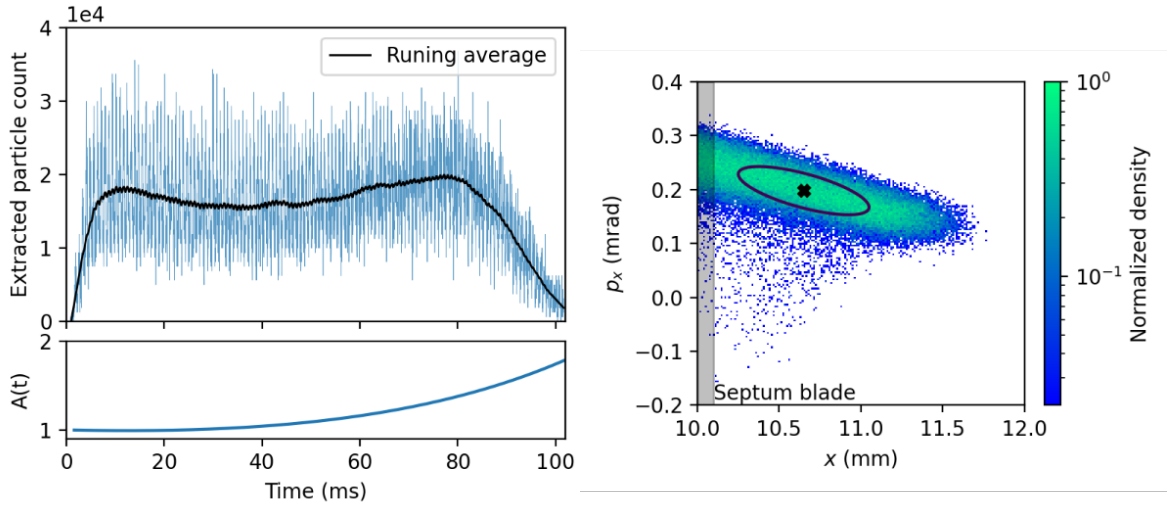

Figure 6.4: Exemplary extracted beam from the eight-fold symmetric DESY 4 lattice. On the left particle counts of electrons, that reach the electro-static septum are shown over an extraction of 100 ms. On the bottom panel the amplitude curve utilized for betatronic stimulation is depicted (see equation 6.7). On the right the extracted distribution at the septum position is illustrated. Both pictures are taken from [24]. The ellipse encompasses an emittance of 13 nm rad.

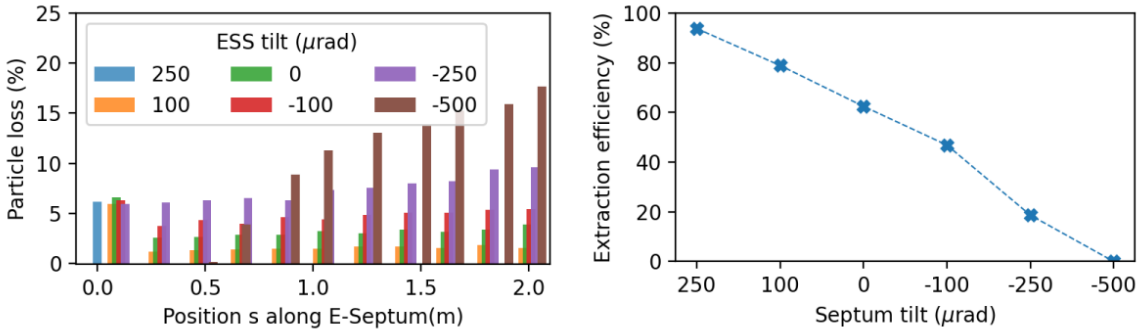

Figure 6.5: Particle losses incurred along a 2 m electrostatic septum. Left panel illustrates the loss map for different misalignment tilts along the septum. On the right the total losses are summarized and translated to extraction efficiency. In both cases cases the septum thickness is 100 μm. Picture on the left is taken from [24].

is 5 m and limit the electrostatic septum length to 2 m. Secondly, the magnetic septum is composed of a thin Lambertson septum with a thickness of 4 mm and it is placed 1.5 m downstream. These preliminary assumptions allow for the design of an extraction channel, but should be further optimized in the future. From these assumptions the first kick necessary given by the electrostatic septum can be determined. This is given by [136]

$$\theta_{\text{septa}} = \frac{qUL}{\beta_r p_0 c d}, \tag{6.9}$$

where U is the voltage and d the distance between the electrode plates, L is the effective length of the septum, $\beta_r = v/c$ and p_0 is the particle momentum. Next we allow for instance the specifications for the J-PARC septum [137], which can deliver U =104 kV and the beam size shown in figure 6.4, such that we can tentatively specify d =1 cm. Therefore $\theta_{\text{septa}} = 3.4\bar{6}$mrad, which allow for a downstream separation of 5.19 mm.

With these considerations tracking simulations have been performed to evaluate the beam loss due to collision with the septum. The results are summarized in figure 6.5. It is clearly visible that the closed orbit has to be tilted by an angle −250 µrad at the extraction straight to reduce completely the losses. Then, the only source of losses happens due to head-on collisions of electrons at the beginning of the septum with the septum's blade. This is depicted in figure 6.4, where particles shaded by the septum blade are considered lost. If the losses along the septum are reduced by shifting the closed orbit, then the extraction efficiency is determined by the effective septum blade thickness. Accordingly, different possible septum thicknesses are assessed and the results are summarized in table 6.1. The results displayed in table 6.1 consider only the most optimized case in favor of extraction efficiency in the DESY eight-fold lattice.

Table 6.1: Extraction efficiency for different blade thicknesses at septum start. The results are shown for the most optimized optics for extraction with the eight-fold symmetric lattice of DESY IV. The septum thicknesses considered are typical specifications for different existing septa found in different laboratories [136].

Septum thickness (µm)	Extraction efficiency (%)
100	92
50	97
30	98

6.3. Final remarks

At this stage of the PETRA IV project, there are competing designs for the injector chain, which have also been discussed in Chapter 3. If the baseline option of constructing DESY IV is pursued, then there are many potential advantages of the implementation of a resonant extraction scheme. First, the extraction efficiency has been shown to be in excess of 90% with electrostatic septum specifications of existing devices in other facilities. This could potentially expand and exploit the full capabilities of a test beam facility. A more thorough presentation and discussion of the design of the resonant slow extraction from a low emittance booster ring is reported in [24].

7

Summary, discussion and conclusions

7.1. Summary

This thesis opens with a brief introduction on fourth-generation synchrotron light sources, discusses the status of the accelerator technologies and elaborates on the connection of the diffraction limit and peak brightness of X-ray photon beams. This is followed by a detailed motivation of the studies. A list of contributions to scientific journals related to the work performed during this thesis is included. Following the introductory section, a dedicated chapter is presented to cover essential concepts of accelerator physics. Some of these concepts are illustrated using the primary building block of PETRA IV, the hybrid six-bend achromat.

Special emphasis is placed on two collective effects, as their influence primarily motivates the studies conducted in this thesis. The first is the reduction of beam lifetime due to Touschek scattering, which results in particle loss. The theoretical framework established by A. Piwinski is thoroughly analyzed, leading to the first key result aimed at mitigating this detrimental effect: the equalization of equilibrium beam emittances. This approach effectively reduces charge density within electron bunches, with theoretical predictions indicating a potential doubling of beam lifetime. Subsequently, the theoretical aspects of intra-beam scattering are reviewed and exemplified using the H6BA lattice. Although equilibrium emittances are not explicitly calculated at this stage, theoretical considerations suggest that equalizing the emittances of electron bunches contributes to reducing emittance growth rates, further enhancing beam quality preservation. A short discussion on the influence of impedance and space-charge can be found at the end of the chapter.

Once the theoretical framework is established, the beam dynamics performance of the PETRA IV storage ring and its booster ring, DESY IV, is summarized. This includes a review of the collective work by the PETRA IV beam physics group, with individual contributions highlighted where applicable. A significant contribution in this context is the evaluation of the impact of the revised collimation strategy on beam dynamics. The results indicate no apparent detrimental side effects from the newly devised scheme[1]. Additionally, considerations regarding nonlinear dynamics, particularly off-axis injection efficiency, are discussed.

[1] by L. Malina

Further along, a more detailed description of a topic directly related to the motivation of the studies is provided. The work presented begins with the main research focus on mitigation techniques for the side effects of high-density electron beams expected at the future PETRA IV storage ring. As a result, the generation of round beams becomes a central area of investigation, as it represents an effective approach to reducing the adverse effects associated with high-density stored beams. Therefore the following chapter discusses extensively the generation schemes to produce round beams and their impact on the beam dynamics. Three schemes are thoroughly assessed and the results can be summarized as follows

- Vertical dispersion waves

  The introduction of vertical dispersion waves provides a straightforward approach. By using the available orbit correctors in the H6BA cell numerous configurations of closed vertical dispersion waves can be generated. Minimal effort is required in introducing closed waves in the arc cells with four orbit correctors. This configuration generates 1 pm rad of vertical emittance with a maximal corrector kick strength of 270 µrad. Therefore 20 cells are needed to generate 20 pm rad of vertical emittance. Alternatively, the introduction of three vertical chicanes in insertion-device-free straight sections is considered. With a bending kick angle of $\theta \approx 7$ mrad the target 20 pm rad vertical emittance can be generated. The functional dependency of the generated emittance on the bending angle θ is described by a power law of fifth order.
- AC dipole excitation

  The effect of external excitations are introduced in particle tracking simulations to evaluate the vertical emittance generation through emittance blow-up. Two excitation waves are assessed and the results can be compared to simple theoretical predictions presented in Chapter 2. The utilization of a single sine-wave with its frequency set to the betatron resonance leads to a system resembling a collection of harmonic oscillators with an eigenfrequency spread determined by chromatic detuning. Consequently the vertical emittance scales with the square of the amplitude of the sine-wave. The scheme is sensitive to vertical chromaticity and the system behaves differently, when the chromaticity is smaller than 5 units. An equilibrium state appears to be reached and simultaneously the centroid oscillation mode is excited, its amplitude is proportional to the inverse vertical chromaticity. Further, a limited band noise has also been utilized as an excitation signal. The system appears to not reach an equilibrium state in terms of emittance and also cannot be properly described as a diffusive phenomenon governed by the Fokker-Planck equation. Nonetheless one can establish that the vertical emittance scales as well with the squared of the amplitude of the signal. A centroid oscillation mode is also excited in this case.
- Emittance sharing mechanism

  The emittance sharing mechanism is triggered by setting the transversal tunes to fulfill $q_x - q_y = 0$. A non-vanishing resonance driving term associated with the combined integrated strength of the skew components in the lattice will always be present in a real machine due to misaligment imperfections. This method can be deployed directly and is the preferred mechanism, due to its operational simplicity and well-established theoretical framework.

The impact on electron beam parameters is then evaluated through numerical simulations[2]. The results confirm the expected Touschek lifetime enhancement predicted by theory, demonstrating an improvement by a factor of two. Furthermore, the equilibrium emittance is calculated using numerical methods that account for synchrotron radiation effects, quantum excitation diffusion, longitudinal and transverse short-range wakefields, and intra-beam scattering growth rates. Simulations indicate that the beam emittance remains below 20 pm rad, even for high single-bunch charges exceeding the operationally planned values (up to $I = 2.5\,\mathrm{mA}$).

With these promising results, the evaluation of off-axis injection dynamics near the coupling resonance follows. Simulation campaigns are pursued and demonstrate that no injection efficiency loss is expected at PETRA IV. It has been assumed that the strategies proposed to manipulate the beam emittance of the injected beam are available. There is a noticeable DA reduction, which results from setting the vertical working point closer to the integer resonance. No considerable LMA reduction or increment is expected.

After this set of simulations, experimental campaigns of off-axis injection with a machine set at the coupling resonance are pursued at PETRA III and at ESRF-EBS. For both machines simulations yield high injection efficiency in excess of 99%. In contrast, the experiments reveal that at both of the machines the injection efficiency decreased to less than 20%. This efficiency is unacceptable for operational purposes. Further, the formation of resonance islands in PETRA IV unfolds during off-axis injection simulations. Particles are observed to be trapped at least 0.7 s. Before considering potential applications or mitigation of the islands experimental campaigns are launched in collaboration with ESRF to investigate this finding. Several preliminary studies in the machine showed no evidence of the formation of the islands. A final campaign, where the phase-space is scanned by setting precalculated current ramps at the available four injection kickers and simultaneously recording the turn-by-turn data with all the BPMs deliver sufficient experimental data to conclude that quasi-stable resonance islands are generated. Their existence is both observed in tracking simulations and experiments. A key trace of the islands is observed when the beam is kicked to high enough amplitudes, such that the horizontal tune crosses the third order resonance. Particles are trapped in the islands and this is made evident by a long standing tripple trace in the recorded BPM data. The measured island capture lifetime is $\lambda = 6.74\mathrm{s} \pm (0.23_{\mathrm{stat.}} + 0.03_{\mathrm{sys.}})\mathrm{s}$. Further, results on an estimation of the amplitude detuning coefficient and the reconstruction of the phase-space trace during the experimental campaign are documented.

Finally, a summary of the design of a novel resonant slow extraction scheme from the future low emittance booster ring lattices considered for DESY IV is presented. The extraction optics setup is discussed and usual figures of merit to characterize the extraction scheme are reported. The emittance of the extracted beam for the exemplary extraction is 13 nm rad and is below the equilibrium emittance of the booster ring at 6 GeV. To estimate the extraction efficiency multiple simulations campaigns are launched, first to evaluate the loss of beam along the electrostatic septum and secondly to determine the loss due to head-on collision with the beginning of the septum. For the most optimized extraction setup with the eight-fold symmetric lattice, the extraction efficiency can go as low as 92%. The thickness of the septum considered for this case is compatible with specifications of existing devices in different laboratories offering slowly extracted beams.

[2]these calculations are performed in close collaboration with C. Li.

7.2. Discussion

7.2.1. Round beam generation

The results presented show three possible schemes to generate round beams. The implementation of dispersion waves is assessed and appears to be straightforward. The generation of the waves in the arc cells rely on the use of orbit correctors. This approach can potentially generate one pm rad for each cell utilized. The question remains open if operating orbit correctors for both purposes won't lead to saturation and therefore less flexibility in operation of the machine. Priority should be given to their primary purpose. The orbit correctors should be able to keep the beam orbit as flat as possible and flexibility might be required, depending on the misalignment and field errors in commissioning and re-commissioning of the machine. Further, orbit correctors might be required for special steering or closed bump generation at the center of the insertion devices straight sections for photon beamline users. If this option is at some point in the future preferred, the correctors maximal kick strength can be specified to be higher, which would have a direct impact on the design of the magnets and probably on the cell and girder designs. Additionally, dedicated insertion-device-free straights can be equipped with vertical chicanes and generate sufficient emittance. This alternative could be more attractive and can be explored in the future. The use of vertical dispersion waves might also be interesting for expanding the capabilities of the machine protection system. By implementing closed waves in free space at the long straight sections, one can eventually benefit from a dispersive collimation scheme.

Moreover, the use of AC dipole excitations is assessed in simulations. This scheme originally served to determine the specifications of a peripherial system attached to the feedback system foreseen for PETRA IV [100]. The system will be able to add signals that will be later merged with the correction from the feedback to influence the beam. This will add the capability of shaking the beam vertically, similar to the implementation at ESRF [55]. The results of the single sine-wave excitation can be described quite well with a simple theoretical model. The emittance scales with the square of the amplitude and is therefore directly proportional to the power of the excitation signal. For operational values of the chromaticity the predictions hold and as observed at ESRF [55], when the chromaticity is decreased, the shaker induces mostly coherent centroid oscillations. The scheme is assessed as well with a noise band drawn from a uniform random distribution. For this case the system appears to not reach an equilibrium state. This variation appears to be agnostic to the chromaticity setup, except at very low values ($\xi_y \approx 0$). Both the excitation signals increase the centroid oscillations, which could be later detrimental for photon beam users. For the case of PETRA IV operational considerations should be further assessed, for instance, how the stability of the tune will impact the scheme and what kind of control loops have to be implemented to keep the emittance constant.

As a third variation to generate round beams, the emittance sharing mechanism is triggered, when the working point of the machine is brought near the coupling resonance condition $q_x = q_y$. This leads to equalization of the emittances and different emittance ratios can be achieved by controlling the distance to the coupling resonance condition. In simulations, the computation of the resonance driving term can be directly obtained from tracking codes or deduced by means of the closest tune approach [61]. In-house and experience shared from other facilities reveal that reliable and precise methods exist to correct the RDT by making use

of skew quadrupoles and optics techniques. The displacement of the tunes is also a standard procedure. This leads to the conclusion, that the generation of round beams by making use of the coupling resonance is preferred. As an additional advantage, the brightness of the photon beams is not expected to decrease considerably. Furthermore it might help in the stabilization of the X-ray optics which are sensitive to mechanical vibrations. The challenge of this operation mode lies in achieving high efficiency of the off-axis injection scheme. The first direct consequence encountered by decreasing the vertical tune closer to the horizontal is the marginal reduction of the DA. The DA reduction can be understood by taking a closer look at the amplitude detuning coefficients which are preserved. The amplitude detuning coeffients are primarily influenced by the nonlinear elements, i.e. sextupole and octupoles. Therefore, as mentioned before, the action at which the vertical tune reaches the integer resonance reads

$$J_x = -\frac{\kappa_y + \sqrt{\kappa_y^2 - 4q_{y,0}\kappa_y^{(2)}}}{2\kappa_y^{(2)}} < \frac{0.5 - q_{x,0}}{\kappa_x} \tag{7.1}$$

and is smaller than the action at which the horizontal tune reaches the half-integer resonance. The detuning coefficients can be read from Table 3.3. The first easy step to take is to increase the tunes $q_x = q_y \approx 0.206$ to elevate the action at which both the half-integer and integer resonance meet the tunes. This working point can be deduced by solving for q in

$$-\frac{\kappa_y + \sqrt{\kappa_y^2 - 4q\kappa_y^{(2)}}}{2\kappa_y^{(2)}} = \frac{0.5 - q}{\kappa_x}, \tag{7.2}$$

which is the condition at which the integer and half-integer resonances are excited at the same action J_x. At this working point the DA should cross the resonances at J_x =0.755 µm, corresponding to $x_{\mathrm{inj}} = 8.3$ mm instead of the optimal 8.5 mm in the uncoupled case $(q_x, q_y) = (0.18, 0.27)$.

Future studies should concentrate on optimization campaigns to increase the nominal DA by optimizing nonlinear optics, thereby variating the amplitude detuning coefficients. The LMA is preserved according to tracking simulations and no further action is required in this regard with the current setup. This is mostly because the LMA is determined by the off-momentum nonlinear optics determined by the octupoles and sextupoles, which have not been considerably modified. Displacing the working point will preserve or have a moderate impact on the LMA, since this is limited in the same way as the DA. A good indicator for this is the chromatic detuning shown in figure 3.10, which summarizes the overall impact of the sextupoles and octupoles on the off-momentum optics. Varying the sextupoles and octupoles settings will have a direct impact on the global chromatic detuning and thus optimization campaigns have to involve careful balancing between DA and LMA alterations.

7.2.2. Round beam operation consequences on the beam dynamics performance

The operation of the machine with round beams appears to be beneficial or neutral to most of the aspects defining the beam dynamics performance. The main aspects that are enhanced and have been repeatedly discussed are the Touschek lifetime and the reduction of the emittance blow-up through mitigation of the intra-beam scattering growth-rates. These two aspects are

beneficial for photon users as brightness is preserved and the duty-cycle of the injector chain is reduced. It is estimated [23], that top-up injection events are required every half an hour, determined by the lifetime of the vacuum in brightness mode. In this case there would be no considerable lifetime increase, since the lifetime is not determined by the Touschek scattering losses. For the timing mode however, the top-up events would be required every 12 min instead of every 6 min. If the vacuum lifetime exceeds considerably the expected mark of 50 h [23], then the increment of Touschek lifetime in the round beam operation won't limit the beam lifetime. The expected lifetime in brightness mode is expected to increase from 50 h to 100 h and therefore top-up injection events would only be needed every hour. This optimistic scenario is advantegous for users, since injection events are known to perturb experiments due to the ramp-up of injection kickers. It would also considerably relax the duty cycle of the injector chain and make more attractive the implementation of a resonant slow extraction at DESY IV.

Another aspect to consider is the total lifetime in a system with competing processes

$$\frac{1}{\tau} = \sum_i \frac{1}{\tau_i}, \tag{7.3}$$

where τ represents the total lifetime of the beam and τ_i the different events that limit the lifetime, e.g. Touschek scattering τ_{LT} and vacuum lifetime $\tau_{\text{vac.}}$. Then, for example if $\tau_{\text{vac.}} \approx \tau_{LT} = 100\text{h}$ the total lifetime is reduced to $\tau = 50\text{h}$ and there is no considerable increment in the lifetime. Therefore one process has to predominantly dominate in order to avoid a detrimental combination that can impact negatively the overall lifetime.

Additionally a key feature that has been investigated in this thesis is the efficiency of off-axis injection at PETRA III and ESRF-EBS. Simulation of the process yields efficiencies in excess of 99% and appear to over-estimate the achievable values in experimental conditions. The optimization of the off-axis injection of PETRA III requires dedicated efforts that go beyond the scope of this thesis and involve investigations of the transfer line and injection optics. Many of these studies have taken a secondary role, since the performance of PETRA III is not affected by injection efficiencies in the range of 60% to 70%. A reduction by a factor of three would be unacceptable though. An experimental demonstration of off-axis injection near the coupling resonance reports injection efficiencies at the level of 70% at the Standford Positron Electron Accelerating Ring (SPEAR) in California, USA [105]. A 30% reduction from the nominal injection efficiency of about 100%. It is worth noting that in this study the measured emittance ratio only reached the 40% level, therefore no round beams were actually generated, although the tunes were set to the coupling resonance condition $q_x - q_y = 0$. On the other hand, the same study reports very low injection efficiencies ($< 10\%$), when the coupling ratio increases to unity by letting the resonance driving term be increased. Therefore one can assume that off-axis injection in third-generation light sources near the coupling resonance would lead to very poor injection efficiencies. This is due to the very low amplitude detuning coefficients present in the dynamics, that let the coupling resonance be triggered very promptly, thereby leading to particle loss.

A machine with more comparable nonlinear optics is found at ESRF and experiments conducted demonstrate a reduced injection efficiency. The nominal injection efficiency at ESRF is similar to the values reported for PETRA III (60% to 70%). There are many aspects that contribute to this. For instance, the measured DA of the EBS has been reported to be approximately 25% lower than expected from simulations. Simulations yield a DA of 9 mm to

10 mm at injection (β =18.5 m, $\alpha_x = 0$), whereas the measured value is estimated to lie around 7.5 mm [14]. A possible explanation of this reduction can lie in the nonlinear dynamics. A recent measurement of the detuning coefficients at ESRF-EBS [112] reported a good agreement between model and measurement of the horizontal detuning coefficient κ_x. On the other hand, it is found that the vertical detuning coefficient κ_y is a factor two lower in the model than in the measurement.

Tracking simulations performed in Subsection 4.3.3 with the EBS lattice show that the amplitude detuning is dominated by the linear coefficients and read $(\kappa_x, \kappa_y) = (0.101, -0.115)\ \mu\text{m}^{-1}$. If the finding reported in [112] is applied to simulation results, then the action J_x at which the vertical tune q_y reaches the integer resonance is reduced from 2.95 µm to 1.48 µm. This translates in a reduction of the DA from 10.5 mm to 7.5 mm and it would be compatible with the DA measurement reported in [14]. It is worth noting that the vertical tune measurement is prone to higher uncertainties due to the low amplitudes of the oscillations. Therefore if this interpretation holds, then by shifting the working point from nominal values $(q_x, q_y) = (0.16, 0.34)$ to the coupling resonance $(0.24, 0.24)$ as in the experiment, the vertical tune reaches the integer resonance more promptly and limits the DA at 6.2 mm. A closer look to the simulation results shown in figure 4.23 reveal that the injected beam centroid would lie very close to the edge of the DA in the experiment. Thus, the reduced injection efficiency can be understood from these considerations. Similar strategies as suggested for the PETRA IV case can be pursued to corroborate that the efficiency of off-axis injection can be restored to operational values.

7.2.3. Quasi-stable resonance islands

An intriguing result brought by these studies is the observation of quasi-stable resonance islands. The design of the H6BA strives for full cancellation of the resonance driving terms by optimal placing of the sextupoles with a π-phase-advance between them. For example, the cancellation of the resonance driving term S is evident. By making use of equation 5.5 and assuming the integrated sextupole strengths S_n are identical in each cell, then the generated RDT at each cell reads

$$S_{\text{cell}} = S_n(e^{i3\psi_n} + e^{i3\psi_{n+1}}) = S_n(e^{i3\psi_n} + e^{i3(\psi_n+\pi)}) = 0.$$

In the designed machine the conditions $S_n \approx S_{n+1}$ and $\psi_{n+1} \approx \psi_n + \pi$ hold only approximately and therefore a weak RDT is found to be (S, ψ_S)=(4.33 $\text{m}^{1/2}$, -0,95°) at the nominal working point $(q_x, q_y) = (0.18, 0.27)$ of PETRA IV. This can partially explain the generation of resonance islands.

In the last couple of decades there has been a collective effort to characterize the dynamics in electron storage rings near the third order resonance $3q_x = 1$ and the appropiate references have been mentioned [47, 107, 132, 138]. The theory has been reviewed briefly in Section 5.1. One important aspect that has to be discussed is the validity of this theoretical description. For instance, from the Kobayashi Hamiltonian perspective the derivation follows a usual stroboscopic approach, where the dynamics are sampled every three turns. Thus, this approach makes use of approximations that are only valid when the working point is found near the third order resonance. Therefore the extension to the Hamiltonian described by equations 5.3 and 5.4 can be assumed to be restricted as well to $|3q_x - 1| < 1/(6\pi)$. It is also worth noting that the available literature [47, 107, 132, 138] making use of this theoretical

framework describes systems near the condition $|3q_x - 1| < \Delta_x$ with Δ_x typically in the range of 10^{-3}.

The setup of the simulations at PETRA IV and experiments at the ESRF-EBS reach the highest order of magnitude possible for $\Delta_x \approx 10^{-1}$. Tentatively, the position of the fixed points have been evaluated with equation 5.7 and some agreement is found for both PETRA IV and the ESRF-EBS. The action at which the fixed points are found still cannot be accurately recovered from these theoretical predictions. Therefore it can be concluded that the theory has to be extended, such that the treatment has a broader range of validity. This could be done by introducing an amplitude dependent RDT, which considers the variation of the optical functions at the closed orbit of the resonance islands. On the other hand, another nonlinear component could be responsible for the shift of the position of the fixed points. The first nonlinear component that could generate an amplitude dependent RDT for the third order resonance is the decapole. It remains as conjecture, if the combination of nonlinear components present in the lattice can generate a sufficiently large integrated decapole component in the dynamics or if fringe fields in the magnetic elements posses as high enough decapole component to account for this.

Finally, the robust diagnostic tools at ESRF-EBS lead to experimental observations that are compatible with the generation of the resonance islands. The lifetime of the captured electrons is found to be one order of magnitude lower than the prediction from tracking simulations. In this simulation campaign 10^4 particles are initialized with the covariance matrix of particles trapped in the islands from previous numerical experiments. Due to the high computational effort only 10^5 turns are tracked and from this information the lifetime is recovered. The simulation yields a constant escape rate of particles, where no exponential decay is visible. This effort can be extended to longer tracking times and higher particle numbers to determine, if this could be the source of the discrepancy. No convergence tests have been performed so far.

Additionally, the condition to reduce the resonance driving term can be imposed more strictly to investigate the influence of S on the islands. This might offer a mechanism to reduce or increase the area of the resonance islands and therefore control the capture efficiency and lifetime. Future studies have to be performed to investigate the capture and escape dynamics more in detail. This in order to exploit the full potential of the resonance islands in fourth-generation light sources.

7.2.4. Resonant slow extraction from DESY IV

The resonant slow extraction has been considered and this is the first time such a scheme is discussed in the context of low emittance electron booster rings. For the past design of DESY IV with the six-fold symmetry, the generation of resonance islands with the established theoretical framework is straightforward. Since this design has been ruled out it won't be further discussed. An extended discussion of the slow extraction design on this lattice can be found in [24]. For the current design of DESY IV with the eight-fold symmetry the theory had some shortcomings. First, the generation of the islands is not possible without partial correction of the amplitude detuning coefficient κ_x. In this study the working point was brought near the third order resonance $3q_x = 1$ and the range of validity of the Hamiltonian described by equations 5.3 and 5.4 is put to test. It is later established, that in this case the

tune dependence on amplitude can be satisfactorily described by

$$q_x = q_{x,0} + \kappa_x J_x + \kappa_x^{(2)} J_x^2, \tag{7.4}$$

with $(\kappa_x, \kappa_x^{(2)}) = (3.97\ \mathrm{mm}^{-1}, 20.7\ \mathrm{mm}^{-2})$ and thus dominated as well from the second order detuning coefficient. This is another case where the established theory fails to accurately describe the transversal dynamics. Nonetheless the design study continued by applying the RF-KO slow extraction method. Exemplary extracted particle beams have been computed with help of extensive tracking simulations. The extracted beam preserves to a good extent the beam quality, where the beam emittance is reduced from 20 nm rad to 13 nm rad, although the distribution becomes skewed as is typical from slow extraction processes. Despite the fact that the extracted beam quality has been thus far not important, it might become increasingly relevant if irradiation of delicate samples is pursued in the future. The extraction rate can be controlled with a simple double sine-wave. In future studies extension to and optimization of more sophisticated excitation signals should be considered. The slow extraction signal should be paired to feedback loops to evaluate the achievable dynamic range of the scheme.

Moreover, the extraction efficiency is derived from tentative specifications and considerations of the extraction channel and its devices. It is found, that the extraction efficiency can reach values in excess of 92% with specifications of broadly available slow extraction electrostatic septa. State-of-the-art devices exist with effective septum blades of 30 µm thickness. These are housed at JPARC and are achieved at a 1.5 m-long electrostatic septum for the slow extraction of 30 GeV proton beams [137]. Similar specifications are achieved for an ultra-thin electrostatic septum at FNAL [139]. With such a device the extraction efficiency can be increased to 98%. These results paint an optimistic picture and lay a basis as conceptual work for further implementation and realization of a slow extraction from low emittance booster rings. It might be advisable to evaluate if the introduction of such advanced beam manipulations are necessary for the final implementation of resonant slow extraction. If the dynamics can be reduced to a description compatible with the Kobayashi Hamiltonian more established tools can be utilized. For the design of DESY IV the necessity of the extension of the methods is motivated by the high chromatic spread, that is typical at future low emittance booster rings.

7.3. Conclusions and outlook

After conducting these studies, we can now draw some conclusions. The first concerns the operation of PETRA IV at the coupling resonance. This advanced mode appears to enhance overall machine performance, provided that injection efficiency remains within acceptable limits. Future studies should evaluate this by characterizing the nonlinear dynamics of fourth-generation light sources based on hybrid multi-bend achromat cells.

If injection efficiency proves too low for operation, a mitigation scheme could be implemented. One approach is to adjust the working point during injection events—ramping it to a more favorable value and restoring it after charge top-up. To maintain the emittance ratio, an AC dipole or a vertical dispersion wave could be used to counteract flat beam effects if they are deemed intolerable for photon users. Applying such a scheme introduces additional considerations, notably orbit stability. While injection-related disturbances are generally unavoidable, efforts should focus on minimizing their impact on photon users.

Additionally, the operation of the machine near the coupling resonance is expected to increase the single- and coupled-bunch (in-)stability thresholds set by wakefields generated due to impedance. An experimental study is ongoing to determine the achievable benefits at ESRF and the results are promising. Preliminary results show that the transverse mode coupling instability can be reduced and thus the single-bunch threshold at $\xi_y = 0$ is increased by 10%. Further, simulations with PETRA IV[3] show that the coupled bunch instability growth rates are mitigated, when the machine is operated at the coupling resonance. Theoretical bases have been layed out in [74], but future studies should extend the known results. With these expected enhancements, single-bunch charges can be increased and thus users can profit from advanced timing modes. Operation at the coupling resonance is an efficient strategy to enhance many aspects of the beam dynamics performance of fourth-generation light sources.

Moreover, the exploitation of resonance islands has potential for advanced operational modes. Possible advanced operation modes that make use of the buckets have to be further assessed, but this thesis lays the initial steps for further discussions in this direction. Future experimental campaigns have been already planned and the experimental data will be submitted to a peer-reviewed journal.

Furthermore, the slow resonant extraction concept study is another example, where the utilization of resonant phenomena can extend the capabilities of the facility. Recent discussions have been centered around the possibility of combining the use of crystal channeling with slow extraction schemes. Fundamental work has been performed at CERN for enhancement of collimation and machine protection with the implementation of crystals [140]. Recent studies have also assessed the possibility of combining the resonant extraction with crystal channeling schemes [130, 131]. This topic has remained experimentally unexplored for electron machines until very recently [141]. A study is ongoing to evaluate also the combination of these two techniques at DESY IV. The main goal would be to relax the specifications of the electrostatic septum or to fully replace the device with bent crystals. Looking forward, future studies can consider even a slow extraction scheme from the main storage ring with use of the resonant islands and the crystal channeling technique.

In this thesis two resonances are predominantly studied: the coupling and the third integer resonance. With the theoretical tools available some shortcomings are encountered and highlight the need for further refinement and development of the models for the precise description of the third order resonance. With proliferation of low emittance electron synchrotrons and storage rings this task should take higher priority in the future. To conclude, the work performed along this thesis reveals and serves as evidence, that the potential of synchrotron radiation facilities can be extended with extensive and intensive use of resonant phenomena.

[3] performed by C. Li.

Bibliography

[1] E. Lohrmann and P. Soeding, *Von schnellen Teilchen und hellem Licht: 50 Jahre Deutsches Elektronen-Synchrotron DESY; 1. Auflage*. Weinheim: Wiley-VCH, 2009.

[2] "Lightsources.org web page." `https://lightsources.org/about-2/`. Accessed: 2024-12-11.

[3] The Royal Swedish Academy of Sciences, "Scientific Background on the Nobel Prize in Chemistry 2009: STRUCTURE AND FUNCTION OF THE RIBOSOME." `https://www.nobelprize.org/uploads/2018/06/advanced-chemistryprize2009.pdf`, Oct 2009.

[4] F. R. Elder, A. M. Gurewitsch, R. V. Langmuir, and H. C. Pollock, "Radiation from electrons in a synchrotron," *Phys. Rev.*, vol. 71, pp. 829–830, Jun 1947.

[5] R. Chasman, G. K. Green, and E. M. Rowe, "Preliminary Design of a Dedicated Synchrotron Radiation Facility," *IEEE Transactions on Nuclear Science*, vol. NS-22, Jun 1975.

[6] "Encyclopedia of Synchrotron Radiation Facilities, RIKEN Spring-8 Center," 2020.

[7] Z. Zhao, *Storage Ring Light Sources*, pp. 57–76. World Scientific, 01 2011.

[8] D. Einfeld, J. Schaper, and M. Plesko, "Design of a diffraction limited light source (DIFL)," in *Proceedings Particle Accelerator Conference*, vol. 1, pp. 177–179 vol.1, 1995.

[9] D. Einfeld, M. Plesko, and J. Schaper, "First multi-bend achromat lattice consideration," *Journal of Synchrotron Radiation*, vol. 21, pp. 856–861, Sep 2014.

[10] K.-J. Kim, "Brightness, coherence and propagation characteristics of synchrotron radiation," *Nuclear Instruments and Methods in Physics Research Section A: Accelerators, Spectrometers, Detectors and Associated Equipment*, vol. 246, no. 1, pp. 71–76, 1986.

[11] R. P. Walker, "Undulator radiation brightness and coherence near the diffraction limit," *Phys. Rev. Accel. Beams*, vol. 22, p. 050704, May 2019.

[12] S. Schreiber and DESY, "Soft and Hard X-ray SASE Free Electron Lasers.," *Superconductor science and technology*, vol. 03, pp. 93–120, 2010.

[13] P. F. Tavares, E. Al-Dmour, Å. Andersson, F. Cullinan, B. N. Jensen, D. Olsson, D. K. Olsson, M. Sjöström, H. Tarawneh, S. Thorin, and A. Vorozhtsov, "Commissioning and first-year operational results of the MAXIV 3GeV ring," *Journal of Synchrotron Radiation*, vol. 25, pp. 1291–1316, Sep 2018.

[14] P. Raimondi, N. Carmignani, L. R. Carver, J. Chavanne, L. Farvacque, G. Le Bec, D. Martin, S. M. Liuzzo, T. Perron, and S. White, "Commissioning of the hybrid multibend achromat lattice at the European Synchrotron Radiation Facility," *Phys. Rev. Accel. Beams*, vol. 24, p. 110701, Nov 2021.

[15] E. Peoples-Evans, "Status and first results of the APS-U, the high-brightness upgrade of the Advanced Photon Source at the Argonne National Laboratory." presented at IPAC'24, Nashville, TN, 2024, paper TUZN2, unpublished, 05 2024.

[16] L. Liu, M. Alves, A. Oliveira, X. Resende, and F. de Sá, "Sirius Commissioning Results and Operation Status," in *Proc. IPAC'21*, no. 12 in International Particle Accelerator Conference, pp. 13–18, JACoW Publishing, Geneva, Switzerland, 08 2021. https://doi.org/10.18429/JACoW-IPAC2021-MOXA03.

[17] Y. Jiao, G. Xu, X.-H. Cui, Z. Duan, Y. Guo, P. He, D. Ji, J. Li, X.-Y. Li, C. Meng, Y. Peng, T. Saike, J.-Q. Wang, N. Wang, Y.-Y. Wei, H. Xu, F. Yan, C.-H. Yu, Y.-L. Zhao, and Q. Qin, "The heps project," *Journal of Synchrotron Radiation*, vol. 25, pp. 1611–1618, 09 2018.

[18] A. Streun, M. Aiba, M. Böge, C. Calzolaio, M. Ehrlichman, M. Negrazus, B. Riemann, and V. Vrankovic, "Swiss light source upgrade lattice design," *Phys. Rev. Accel. Beams*, vol. 26, p. 091601, Sep 2023.

[19] C. G. Schroer, R. Roehlsberger, E. Weckert, R. Wanzenberg, I. Agapov, R. Brinkmann, and W. Leemans, eds., *PETRA IV: upgrade of PETRA III to the Ultimate 3D X-ray microscope. Conceptual Design Report*. Hamburg: Deutsches Elektronen-Synchrotron DESY, 2019.

[20] K. Balewski, W. Brefeld, W. Decking, H. Franz, R. Rohlsberger, and E. Weckert, "PETRA III: a low emittance synchrotron radiation source (Technical design report)," Tech. Rep. DESY-04-035, DESY, 2004. ISSN: 0418-9833.

[21] C. G. Schroer, I. Agapov, W. Brefeld, R. Brinkmann, Y.-C. Chae, H.-C. Chao, M. Eriksson, J. Keil, X. Nuel Gavaldà, R. Röhlsberger, O. H. Seeck, M. Sprung, M. Tischer, R. Wanzenberg, and E. Weckert, "PETRA IV: the ultralow-emittance source project at DESY," *Journal of Synchrotron Radiation*, vol. 25, pp. 1277–1290, Sep 2018.

[22] B. Balewski, "Commissioning of PETRA III," in *Proceedings International Particle Accelerator Conference*, vol. 1, 2010.

[23] I. Agapov, S. Antipov, R. Bartolini, R. Brinkmann, Y.-C. Chae, E. C. Cortés García, D. Einfeld, T. Hellert, M. Huening, M. A. Jebramcik, J. Keil, C. Li, L. Malina, and R. Wanzenberg, "Beam dynamics performance of the proposed PETRA IV storage ring," 2024.

[24] E. C. Cortés García, I. V. Agapov, and W. Hillert, "Design of a resonant slow extraction from low-emittance electron booster rings using transverse resonance island buckets," *Phys. Rev. Accel. Beams*, vol. 28, p. 011601, Jan 2025.

[25] E. C. Cortés García and I. Agapov, "Dynamics of off-axis injection near the coupling resonance at petra iv," *Journal of Physics: Conference Series*, vol. 2687, p. 032039, jan 2024.

[26] E. C. Cortés García, R. Singh, P. Niedermayer, R. Taylor, E. Benedetto, E. Feldmeier, M. Hun, and T. Haberer, "Interpretation of the horizontal beam response near the third integer resonance," *Physical review accelerators and beams*, vol. 27, no. 12, p. 124001, 2024.

[27] S. A. Antipov, V. Gubaidulin, I. Agapov, E. C. Cortés García, and A. Gamelin, "Space charge effects in fourth-generation light sources: The PETRA IV and SOLEIL II cases," *Phys. Rev. Accel. Beams*, vol. 28, p. 024401, Feb 2025.

[28] P. J. Niedermayer, R. Singh, G. Franchetti, E. C. Cortés-García, E. Feldmeier, and T. Haberer, "Investigation of micro spill in RF KO extraction using tailored excitation signals," *Journal of Physics: Conference Series*, vol. 2687, p. 052029, jan 2024.

[29] F. Hinterberger, *Physik der Teilchenbeschleuniger und Ionenoptik*. Berlin Heidelberg: Springer-Verlag, 2008.

[30] S. Lee, *Accelerator Physics*. World Scientific, 2012.

[31] H. Wiedemann, *Particle accelerator physics; 3rd ed.* Berlin: Springer, 2007.

[32] A. Wolski, *Beam dynamics in high energy particle accelerators; second edition*. Hackensack: World Scientific, 2023.

[33] R. von Hahn, A. Becker, F. Berg, K. Blaum, C. Breitenfeldt, H. Fadil, F. Fellenberger, M. Froese, S. George, J. Göck, M. Grieser, F. Grussie, E. A. Guerin, O. Heber, P. Herwig, J. Karthein, C. Krantz, H. Kreckel, M. Lange, F. Laux, S. Lohmann, S. Menk, C. Meyer, P. M. Mishra, O. Novotný, A. P. O'Connor, D. A. Orlov, M. L. Rappaport, R. Repnow, S. Saurabh, S. Schippers, C. D. Schröter, D. Schwalm, L. Schweikhard, T. Sieber, A. Shornikov, K. Spruck, S. Sunil Kumar, J. Ullrich, X. Urbain, S. Vogel, P. Wilhelm, A. Wolf, and D. Zajfman, "The cryogenic storage ring CSR," *Review of Scientific Instruments*, vol. 87, p. 063115, 06 2016.

[34] L. Deniau, H. Grote, G. Roy, and F. Schmidt, *The MAD-X Program (Methodical Accelerator Design) Version 5.07.00 User's Reference Manual*. CERN, May 2021.

[35] E. Courant and H. Snyder, "Theory of the alternating-gradient synchrotron," *Annals of Physics*, vol. 3, no. 1, pp. 1–48, 1958.

[36] J. S. Schwinger, "On radiation by electrons in a betatron," tech. rep., Lawrence Berkeley Nat. Lab., Berkeley, CA, 1996.

[37] R. H. Helm, M. J. Lee, P. L. Morton, and M. Sands, "Evaluation of synchrotron radiation integrals," *IEEE Trans. Nucl. Sci.*, vol. 20, pp. 900–901, 1973.

[38] M. Sands, "The Physics of Electron Storage Rings: An Introduction," *Conf. Proc. C*, vol. 6906161, pp. 257–411, 1969.

[39] K. W. Robinson, "Radiation effects in circular electron accelerators," *Phys. Rev.*, vol. 111, pp. 373–380, Jul 1958.

[40] T. O. Raubenheimer, "The Generation and acceleration of low emittance flat beams for future linear colliders," other thesis, Stanford University, 11 1991.

[41] A. J. Lichtenberg and M. A. Lieberman, *Regular and stochastic motion*, vol. 38 of *Applied mathematical sciences*. New York: Springer, 1983.

[42] B. V. Chirikov, "A universal instability of many-dimensional oscillator systems," *Physics Reports*, vol. 52, no. 5, pp. 263–379, 1979.

[43] A. Dragt, *Lie Methods for Nonlinear Dynamics with Applications to Accelerator Physics*. University of Maryland, 06 2018.

[44] A. W. Chao, *Special topics in accelerator physics*. Hackensack: World Scientific, 2022.

[45] R. Cappi and M. Giovannozzi, "Novel method for multiturn extraction: Trapping charged particles in islands of phase space," *Phys. Rev. Lett.*, vol. 88, p. 104801, Feb 2002.

[46] J. Borburgh, S. Damjanovic, S. Gilardoni, M. Giovannozzi, C. Hernalsteens, M. Hourican, A. Huschauer, K. Kahle, G. L. Godec, O. Michels, and G. Sterbini, "First implementation of transversely split proton beams in the cern proton synchrotron for the fixed-target physics programme," *Europhysics Letters*, vol. 113, p. 34001, feb 2016.

[47] M. Ries, J. Feikes, T. Goetsch, P. Goslawski, J. Li, M. Ruprecht, A. Schälicke, G. Wüstefeld, *et al.*, "Transverse resonance island buckets at the MLS and BESSY II," in *Proc. Intern. Part. Accelerator Conf. IPAC*, vol. 15, pp. 138–140, 2015.

[48] P. Goslawski *et al.*, "Two Orbit Operation at Bessy II - During a User Test Week," in *Proc. 10th International Particle Accelerator Conference (IPAC'19), Melbourne, Australia, 19-24 May 2019*, no. 10 in International Particle Accelerator Conference, (Geneva, Switzerland), pp. 3419–3422, JACoW Publishing, Jun. 2019. https://doi.org/10.18429/JACoW-IPAC2019-THYYPLM2.

[49] P. Strolin, "Third-order resonance slow extraction from alternating gradient synchrotrons," tech. rep., CM-P00065556, 1966.

[50] M. Q. Barton, "Beam Extraction from Synchrotons," *eConf*, vol. C710920, p. 85, 1971.

[51] C. Steinbach, H. Stucki, and M. Thivent, "The New slow extraction system of the CERN PS," *Conf. Proc. C*, vol. 930517, pp. 339–341, 1993.

[52] W. Hardt, "Ultraslow extraction out of LEAR," tech. rep., CERN, Geneva, 1981.

[53] K. Holldack, C. Schüssler-Langeheine, P. Goslawski, N. Pontius, T. Kachel, F. Armborst, M. Ries, A. Schälicke, M. Scheer, W. Frentrup, and J. Bahrdt, "Flipping the helicity of x-rays from an undulator at unprecedented speed," *Communications Physics*, vol. 3, p. 61, Apr 2020.

[54] D. D. Caussyn, M. Ball, B. Brabson, J. Collins, S. A. Curtis, V. Derenchuck, D. DuPlantis, G. East, M. Ellison, T. Ellison, D. Friesel, B. Hamilton, W. P. Jones, W. Lamble, S. Y. Lee, D. Li, M. G. Minty, T. Sloan, G. Xu, A. W. Chao, K. Y. Ng, and S. Tepikian, "Experimental studies of nonlinear beam dynamics," *Phys. Rev. A*, vol. 46, pp. 7942–7952, Dec 1992.

[55] N. Carmignani, B. Roche, F. Ewald, L. Carver, S. White, S. Liuzzo, and T. Perron, "Emittance blow-up with a magnetic shaker at different chromaticities," *JACoW*, vol. IPAC2024, p. TUPG26, 2024.

[56] G. Ripken, "Untersuchungen zur Strahlenführung und Stabilität der Teilchenbewegung in Beschleunigern und Storage-Ringen unter strenger Berücksichtigung einer Kopplung der Betatronschwingungen," Tech. Rep. DESY R1-70/4, DESY, 1970.

[57] D. A. Edwards and L. C. Teng, "Parametrization of linear coupled motion in periodic systems," *IEEE Transactions on Nuclear Science*, vol. 20, no. 3, pp. 885–888, 1973.

[58] F. Willeke and G. Ripken, "Methods of Beam Optics," Tech. Rep. DESY-88-114, DESY, 1989.

[59] G. Guignard, "Betatron coupling and related impact of radiation," *Phys. Rev. E*, vol. 51, pp. 6104–6118, June 1995.

[60] R. Lindberg, "Equilibrium emittances of coupled lattices," in *APS Technical Notes*, Accelerator Systems Division, Advanced Photon Source, 01 2014.

[61] M. Minty and F. Zimmermann, *Measurement and Control of Charged Particle Beams*. Springer Verlag, 01 2003.

[62] A. W. Chao, *Physics of collective beam instabilities in high energy accelerators*. Wiley series in beam physics and accelerator technology, New York: Wiley, 1993.

[63] K. Y. Ng, *Physics of intensity dependent beam instabilities*. Hackensack: World Scientific, 2006.

[64] C. Bernardini, G. F. Corazza, G. Di Giugno, G. Ghigo, J. Haissinski, P. Marin, R. Querzoli, and B. Touschek, "Lifetime and beam size in a storage ring," *Phys. Rev. Lett.*, vol. 10, pp. 407–409, May 1963.

[65] A. Piwinski, J. D. Bjorken, and S. K. Mtingwa, "Wilson Prize article: Reflections on our experiences with developing the theory of intrabeam scattering," *Phys. Rev. Accel. Beams*, vol. 21, p. 114801, Nov 2018.

[66] A. Piwinski, "The Touschek effect in strong focusing storage rings," *DESY*, 11 1998.

[67] H. Fu, Z. Duan, and J. Wang, "New analytical formula on the Touschek lifetime of the polarized electron beam in electron storage rings," *Phys. Rev. Accel. Beams*, vol. 27, p. 124401, Dec 2024.

[68] A. Piwinski, "Intra-beam-scattering," *Proceedings of the 9th International Conference on High Energy Accelerators*, 1974.

[69] J. D. Bjorken and S. K. Mtingwa, "Intrabeam Scattering," *Part. Accel.*, vol. 13, pp. 115–143, 1983.

[70] K. L. F. Bane, "A Simplified model of intrabeam scattering," in *8th European Particle Accelerator Conference (EPAC 2002)*, pp. 1443–1445, 6 2002.

[71] S. Nagaitsev, "Intrabeam scattering formulas for fast numerical evaluation," *Phys. Rev. ST Accel. Beams*, vol. 8, p. 064403, Jun 2005.

[72] K. Kubo, S. K. Mtingwa, and A. Wolski, "Intrabeam scattering formulas for high energy beams," *Phys. Rev. ST Accel. Beams*, vol. 8, p. 081001, Aug 2005.

[73] S. K. Mtingwa and A. V. Tollestrup, "Intrabeam Scattering Formulae for Asymptotic Beams with Unequal Horizontal and Vertical Emittances," *FERMILAB-PUB*, 11 1987.

[74] R. Lindberg, "Collective (In)stability Near the Coupling Resonance," *JACoW*, vol. IPAC2021, p. THPAB075, 2021.

[75] G. Franchetti, "Space Charge in Circular Machines," *CERN Yellow Rep. School Proc.*, vol. 3, p. 353, 2017.

[76] J. Keil, I. Agapov, and R. Brinkmann, "A Lattice for PETRA IV Based on the Combination of Different Arc Cell Designs," in *Proc. IPAC'21*, no. 12 in International Particle Accelerator Conference, pp. 399–402, JACoW Publishing, Geneva, Switzerland, 08 2021. https://doi.org/10.18429/JACoW-IPAC2021-MOPAB109.

[77] J. Biasci, J.-F. Bouteille, N. Carmignani, J. Chavanne, D. Coulon, Y. Dabin, F. Ewald, L. Farvacque, L. Goirand, M. Hahn, J. Jacob, G. LeBec, S. Liuzzo, B. Nash, H. Pedroso-Marques, T. Perron, E. Plouviez, P. Raimondi, j.-l. Revol, and V. Serriere, "A low-emittance lattice for the esrf," *Synchrotron Radiation News*, vol. 27, 11 2014.

[78] P. Raimondi, "Hybrid Multi Bend Achromat: from SuperB to EBS," in *8th International Particle Accelerator Conference*, 5 2017.

[79] P. Raimondi, C. Benabderrahmane, P. Berkvens, J. C. Biasci, P. Borowiec, J.-F. Bouteille, T. Brochard, N. B. Brookes, N. Carmignani, L. R. Carver, J.-M. Chaize, J. Chavanne, S. Checchia, Y. Chushkin, F. Cianciosi, M. Di Michiel, R. Dimper, A. D'Elia, D. Einfeld, F. Ewald, L. Farvacque, L. Goirand, L. Hardy, J. Jacob, L. Jolly, M. Krisch, G. Le Bec, I. Leconte, S. M. Liuzzo, C. Maccarrone, T. Marchial, D. Martin, M. Mezouar, C. Nevo, T. Perron, E. Plouviez, H. Reichert, P. Renaud, J.-L. Revol, B. Roche, K.-B. Scheidt, V. Serriere, F. Sette, J. Susini, L. Torino, R. Versteegen, S. White, and F. Zontone, "The extremely brilliant source storage ring of the european synchrotron radiation facility," *Communications Physics*, vol. 6, p. 82, Apr 2023.

[80] H. Ghasem, N. B. Kraljevic, B. Singh, and I. P. S. Martin, "Lattice design for the diamond-ii light source storage ring," *Phys. Rev. Accel. Beams*, vol. 27, p. 110704, Nov 2024.

[81] P. Raimondi, X. Huang, J. Kim, J. Safranek, and T. Rabedeau, "Advanced storage ring lattice options based on hybrid six-bend achromat for Stanford Synchrotron Radiation Lightsource upgrade," *Nucl. Instrum. Meth. A*, vol. 1061, p. 169137, 2024.

[82] P. Raimondi and S. M. Liuzzo, "Toward a diffraction limited light source," *Phys. Rev. Accel. Beams*, vol. 26, no. 2, p. 021601, 2023.

[83] T. Hellert, I. Agapov, S. Antipov, R. Bartolini, R. Brinkmann, Y.-C. Chae, D. Einfeld, M. Jebramcik, and J. Keil, "Error Analysis and Commissioning Simulation for the PETRA-IV Storage Ring," in *Proc. 13th International Particle Accelerator Conference (IPAC'22)*, no. 13 in International Particle Accelerator Conference, pp. 1442–1444, JACoW Publishing, Geneva, Switzerland, 07 2022.

[84] L. Malina, I. Agapov, E. Musa, J. Keil, B. Veglia, N. Carmignani, L. R. Carver, L. Hoummi, S. M. Liuzzo, T. Perron, S. White, and T. Hellert, "Python Library for Simulated Commissioning of Storage-Ring Accelerators," *JACoW*, vol. ICALEPCS2023, p. FR2AO05, 2023.

[85] M. Jebramcik, I. Agapov, S. Antipov, R. Bartolini, R. Brinkmann, D. Einfeld, T. Hellert, J. Keil, G. Loisch, and F. Obier, "Injection Design Options for the Low-Emittance PETRA IV Storage Ring," in *Proc. 13th International Particle Accelerator Conference (IPAC'22)*, no. 13 in International Particle Accelerator Conference, pp. 2689–2692, JACoW Publishing, Geneva, Switzerland, 07 2022.

[86] M. Jebramcik, I. Agapov, S. Antipov, R. Bartolini, R. Brinkmann, D. Einfeld, T. Hellert, and J. Keil, "Collimation Strategy for the Low-Emittance PETRA IV Storage Ring," in *Proc. 13th International Particle Accelerator Conference (IPAC'22)*, no. 13 in International Particle Accelerator Conference, pp. 1445–1448, JACoW Publishing, Geneva, Switzerland, 07 2022.

[87] J. Laskar, "Frequency analysis for multi-dimensional systems. global dynamics and diffusion," *Physica D: Nonlinear Phenomena*, vol. 67, no. 1, pp. 257–281, 1993.

[88] M. Borland, "elegant: A Flexible SDDS-Compliant Code for Accelerator Simulation," in *6th International Computational Accelerator Physics Conference (ICAP 2000)*, 2000.

[89] F. Perez, J. Alvarez, I. Bellafont, B. Bravo, J. Ocampo, A. Salom, P. Solans, M. Ebert, N.-O. Fröhlich, P. Hülsmann, R. Onken, W. Anders, V. Duerr, T. Löwner, A. Matveenko, M. Ries, L. Shi, Y. Tamashevich, A. Tsakanian, H. De Gersem, and W. Müller, "Active harmonic EU cavity: Commissioning and operation with beam," *Nuclear Instruments and Methods in Physics Research Section A: Accelerators, Spectrometers, Detectors and Associated Equipment*, vol. 1072, p. 170195, 2025.

[90] I. Agapov, S. Antipov, R. Brinkmann, A. Ferran Pousa, S. Jalas, M. Kirchen, W. Leemans, A. Maier, A. Martinez de la Ossa, J. Osterhoff, R. Shalloo, M. Thévenet, and P. V. Winkler, *The Plasma Injector for PETRA IV: Enabling Plasma Accelerators for Next-generation Light Sources. Conceptual Design Report*. Hamburg: Deutsches Elektronen-Synchrotron DESY, 2025.

[91] A. Febel and G. Hemmie, "Pia, the positron intensity accumulator for the petra injection," *IEEE Transactions on Nuclear Science*, vol. 26, no. 3, pp. 3244–3245, 1979.

[92] H. Chao, I. Agapov, and S. Antipov, "Design Considerations of a High Intensity Booster for PETRA IV," in *Proc. IPAC'21*, no. 12 in International Particle Accelerator Conference, pp. 1386–1389, JACoW Publishing, Geneva, Switzerland, 08 2021. https://doi.org/10.18429/JACoW-IPAC2021-TUPAB023.

[93] S. A. Antipov, A. F. Pousa, I. Agapov, R. Brinkmann, A. R. Maier, S. Jalas, L. Jeppe, M. Kirchen, W. P. Leemans, A. M. de la Ossa, J. Osterhoff, M. Thévenet, and P. Winkler, "Design of a prototype laser-plasma injector for an electron synchrotron," *Phys. Rev. Accel. Beams*, vol. 24, p. 111301, Nov 2021.

[94] R. Diener, J. Dreyling-Eschweiler, H. Ehrlichmann, I. Gregor, U. Kötz, U. Krämer, N. Meyners, N. Potylitsina-Kube, A. Schütz, P. Schütze, and M. Stanitzki, "The desy ii test beam facility," *Nuclear Instruments and Methods in Physics Research Section A: Accelerators, Spectrometers, Detectors and Associated Equipment*, vol. 922, pp. 265–286, 2019.

[95] J. Breunlin, S. C. Leemann, and A. Andersson, "Improving Touschek lifetime in ultralow-emittance lattices through systematic application of successive closed vertical dispersion bumps," *Phys. Rev. Accel. Beams*, vol. 19, p. 060701, Jun 2016.

[96] T. Hiraiwa, K. Soutome, and H. Tanaka, "Formulation of electron motion in a storage ring with a betatron tune varying with time and a dipole shaker working at a constant frequency," *Phys. Rev. Accel. Beams*, vol. 24, p. 114001, Nov 2021.

[97] A. Bazzani, F. Capoani, and M. Giovannozzi, "Analysis of adiabatic trapping phenomena for quasi-integrable area-preserving maps in the presence of time-dependent exciters," *Phys. Rev. E*, vol. 106, p. 034204, Sep 2022.

[98] P. Niedermayer and R. Singh, "Excitation signal optimization for minimizing fluctuations in knock out slow extraction," *Scientific Reports*, vol. 14, p. 10310, May 2024.

[99] N. C. et al., "Emittance blow-up with a magnetic shaker at different chromaticities," in *Proc. 15th International Particle Accelerator Conference*, no. 15 in IPAC'24 - 15th International Particle Accelerator Conference, pp. 1271–1274, JACoW Publishing, Geneva, Switzerland, 05 2024.

[100] S. Liuzzo, N. Carmignani, S. White, B. Roche, E. Buratin, F. Ewald, K. Scheidt, S. Pfeiffer, G. Kube, E. C. Cortes Garcia, S. H. Mirza, and S. Jablonski, "Technical report on beam diagnostics studies with detailed documentation." `https://www.eurizon-project.eu/work_programme/wp4_synchrotrons`, Jan 2024.

[101] G. Iadarola, A. Abramov, P. Belanger, X. Buffat, R. D. Maria, D. Demetriadou, L. Deniau, D. D. Croce, P. Hermes, P. Kicsiny, P. Kruyt, A. Latina, L. Mether, P. Niedermayer, K. Paraschou, T. Pieloni, M. Seidel, G. Sterbini, F. V. der Veken, L. van Riesen-Haupt, and S. Łopaciuk, "Xsuite: An Integrated Beam Physics Simulation Framework," in *Proc. 68th Adv. Beam Dyn. Workshop High-Intensity High-Brightness Hadron Beams (HB'23)*, no. 68 in ICFA Advanced Beam Dynamics Workshop on High-Intensity and High-Brightness Hadron Beams, pp. 73–80, JACoW Publishing, Geneva, Switzerland, 04 2024.

[102] J. Keil and K. Balewski, "Correction of the Linear Optics at PETRA III," *Conf. Proc. C*, vol. 100523, p. THPD085, 2010.

[103] A. Kling and K. Balewski, "Frequency maps at PETRA III," in *Proc. of IPAC'10*, 2010.

[104] R. Wanzenberg, M. Bieler, J. Keil, G. Sahoo, and M. Schaumann, "PETRA III operation and studies in 2022," *JACoW*, vol. IPAC2023, p. MOPA155, 2023.

[105] T. Zhang and X. Huang, "Off-axis injection for storage rings with full coupling," *Phys. Rev. Accel. Beams*, vol. 21, p. 084002, Aug 2018.

[106] N. Carmignani, L. Carver, S. Liuzzo, T. Perron, and S. White, "Operation of the ESRF Booster with the New EBS Storage Ring," in *12th International Particle Accelerator Conference* , 8 2021.

[107] S. T. Wang, V. Khachatryan, and P. Nishikawa, "Lattice design and experimental studies of nonlinear resonance at the Cornell Electron Storage Ring," *Phys. Rev. Accel. Beams*, vol. 26, p. 104001, Oct 2023.

[108] K. M. Nam, J.-G. Hwang, Y. D. Yoon, and Y. W. Parc, "Revised Hamiltonian near third-integer resonance and implications for an electron storage ring," *Phys. Rev. Accel. Beams*, vol. 27, p. 044001, Apr 2024.

[109] K. Symon, "Beam Extraction at a Third Integral Resonance I-IV," *extraction*, vol. 1000, p. 3, 1968.

[110] "Pyat documentation." `https://atcollab.github.io/at/p/index.html`. Accessed: 2025-02-21.

[111] G. Russo, G. Franchetti, M. Giovannozzi, and E. H. Maclean, "Harmonic analysis of nonstationary signals with application to lhc beam measurements," *Phys. Rev. Accel. Beams*, vol. 27, p. 094001, Sep 2024.

[112] N. Carmignani, L. Carver, L. Hoummi, S. Liuzzo, T. Perron, and S. White, "Nonlinear Dynamics Measurements at the EBS Storage Ring," *JACoW*, vol. FLS2023, p. TU4P18, 2024.

[113] Y. Kobayashi and H. Takahashi, "Improvement of the emittance in the resonant ejection," in *Proc. VIth Int. Conf. High Energy Accelerators*, (Massachusetts), pp. 347–351, 1967.

[114] H. Tsujii, S. Minohara, and K. Noda, "Heavy-Particle Radiotherapy: System Design and Application," *Reviews of Accelerator Science and Technology.*, vol. Volume 2: Medical Applications of Accelerators, pp. 93–110, 2009.

[115] M. Pullia, "Synchrotrons for hadrontherapy," *Reviews of Accelerator Science and Technology.*, vol. Volume 2: Medical Applications of Accelerators, pp. 157–178, 2009.

[116] M. Tomizawa, M. Yoshizawa, K. Chida, J. Yoshizawa, Y. Arakaki, R. Nagai, A. Mizobuchi, A. Noda, K. Noda, M. Kanazawa, A. Ando, H. Muto, and T. Hattori, "Slow beam extraction at TARN II," *Nuclear Instruments and Methods in Physics Research Section A: Accelerators, Spectrometers, Detectors and Associated Equipment*, vol. 326, no. 3, pp. 399–406, 1993.

[117] K. Noda, M. Kanazawa, A. Itano, E. Takada, M. Torikoshi, N. Araki, J. Yoshizawa, K. Sato, S. Yamada, H. Ogawa, H. Itoh, A. Noda, M. Tomizawa, and M. Yoshizawa, "Slow beam extraction by a transverse RF field with AM and FM," *Nuclear Instruments and Methods in Physics Research Section A: Accelerators, Spectrometers, Detectors and Associated Equipment*, vol. 374, no. 2, pp. 269–277, 1996.

[118] K. Noda, T. Furukawa, S. Shibuya, T. Uesugi, M. Muramatsu, M. Kanazawa, E. Takada, and S. Yamada, "Advanced RF-KO slow-extraction method for the reduction of spill

ripple," *Nuclear Instruments and Methods in Physics Research Section A: Accelerators, Spectrometers, Detectors and Associated Equipment*, vol. 492, no. 1, pp. 253–263, 2002.

[119] K. Noda, T. Furukawa, S. Shibuya, M. Muramatsu, T. Uesugi, M. Kanazawa, M. Torikoshi, E. Takada, and S. Yamada, "Source of spill ripple in the RF-KO slow-extraction method with FM and AM," *Nuclear Instruments and Methods in Physics Research Section A: Accelerators, Spectrometers, Detectors and Associated Equipment*, vol. 492, no. 1, pp. 241–252, 2002.

[120] T. Furukawa and K. Noda, "Contribution of synchrotron oscillation to spill ripple in RF-knockout slow-extraction," *Nuclear Instruments and Methods in Physics Research Section A: Accelerators, Spectrometers, Detectors and Associated Equipment*, vol. 539, no. 1, pp. 44–53, 2005.

[121] T. Nakanishi, "Dependence of a frequency bandwidth on a spill structure in the RF-knockout extraction," *Nuclear Instruments and Methods in Physics Research Section A: Accelerators, Spectrometers, Detectors and Associated Equipment*, vol. 621, no. 1, pp. 62–67, 2010.

[122] T. Yamaguchi, Y. Okugawa, T. Shiokawa, T. Kurita, and T. Nakanishi, "Slow beam extraction from a synchrotron using a radio frequency knockout system with a broadband colored noise signal," *Nuclear Instruments and Methods in Physics Research Section B: Beam Interactions with Materials and Atoms*, vol. 462, pp. 177–181, 2020.

[123] C. Schoemers, E. Feldmeier, J. Naumann, R. Panse, A. Peters, and T. Haberer, "The intensity feedback system at Heidelberg Ion-Beam Therapy Centre," *Nuclear Instruments and Methods in Physics Research Section A: Accelerators, Spectrometers, Detectors and Associated Equipment*, vol. 795, pp. 92–99, 2015.

[124] T. Furukawa, K. Noda, M. Muramatsu, T. Uesugi, S. Shibuya, H. Kawai, E. Takada, and S. Yamada, "Global spill control in RF-knockout slow-extraction," *Nuclear Instruments and Methods in Physics Research Section A: Accelerators, Spectrometers, Detectors and Associated Equipment*, vol. 522, no. 3, pp. 196–204, 2004.

[125] M. Gentner, *Präparation von Teilchenstrahlen für Experimente der Hadronenphysik: langsame Extraktion an ELFE@DESY und ELSA, sowie Strahlkühlung an HERA*. PhD thesis, Universität Bonn, 1999.

[126] M. Benedikt, *Optical design of a synchrotron with optimisation of the slow extraction for hadron therapy*. PhD thesis, Technische Universität Wien, 1997.

[127] M. Pullia, *Detailed dynamics of slow extraction and its influence on transfer line design*. PhD thesis, Université Claude Bernard, 1999.

[128] L. Badano, M. Benedikt, P. J. Bryant, M. Crescenti, P. Holy, A. T. Maier, M. Pullia, S. Rossi, and P. Knaus, *Proton-Ion Medical Machine Study (PIMMS), 1*. CERN, 2000.

[129] P. J. Bryant, "Resonant extraction," *CERN Yellow Rep. School Proc.*, vol. 5, p. 315, 2018.

[130] D. E. Veres, M. Giovannozzi, and G. Franchetti, "Exploring the potential of resonance islands and bent crystals for a slow extraction from circular hadron accelerators," *Phys. Rev. Res.*, vol. 6, p. L042018, Oct 2024.

[131] D. E. Veres, M. Giovannozzi, and G. Franchetti, "An innovative method for slow extraction in circular hadron accelerators with resonance islands and bent crystals," *Nuclear Instruments and Methods in Physics Research Section A: Accelerators, Spectrometers, Detectors and Associated Equipment*, vol. 1073, p. 170286, 2025.

[132] S. Wang and V. Khachatryan, "Practical aspects of transverse resonance island buckets at the cornell electron storage ring: design, control and application," 2024.

[133] M. A. Fraser, B. Goddard, V. Kain, M. Pari, F. M. Velotti, L. S. Stoel, and M. Benedikt, "Demonstration of slow extraction loss reduction with the application of octupoles at the cern super proton synchrotron," *Phys. Rev. Accel. Beams*, vol. 22, p. 123501, Dec 2019.

[134] V. Nagaslaev, K. A. Brown, and M. Tomizawa, "Third integer resonance extraction with presence of higher multipoles," *Phys. Rev. Accel. Beams*, vol. 22, p. 043501, Apr 2019.

[135] K. M. Nam, J.-G. Hwang, Y. D. Yoon, and Y. W. Parc, "Revised hamiltonian near third-integer resonance and implications for an electron storage ring," *Phys. Rev. Accel. Beams*, vol. 27, p. 044001, Apr 2024.

[136] B. Holzer, ed., *CERN Yellow Reports: School Proceedings. Beam Injection, Extraction and Transfer*. CERN, 2018.

[137] R. Muto, T. Kimura, A. Matsumura, S. Murasugi, K. Numai, K. Okamura, Y. Shirakabe, M. Tomizawa, and E. Yanaoka, "Devices for High-Efficiency Slow Extraction at J-PARC Main Ring," in *Proc. 68th Adv. Beam Dyn. Workshop High-Intensity High-Brightness Hadron Beams (HB'23)*, no. 68 in ICFA Advanced Beam Dynamics Workshop on High-Intensity and High-Brightness Hadron Beams, pp. 656–661, JACoW Publishing, Geneva, Switzerland, 04 2024.

[138] D. K. Olsson and Åke Andersson, "Studies on transverse resonance island buckets in third and fourth generation synchrotron light sources," *Nuclear Instruments and Methods in Physics Research Section A: Accelerators, Spectrometers, Detectors and Associated Equipment*, vol. 1017, p. 165802, 2021.

[139] M. Alvarez and K. Laureto, "Electrostatic Septa Development at FNAL." 5th Slow Extraction Workshop at MedAustron in Wiener Neustadt, Austria, 2024.

[140] M. D'Andrea, O. Aberle, R. Bruce, M. Butcher, M. Di Castro, R. Cai, I. Lamas, A. Masi, D. Mirarchi, S. Redaelli, R. Rossi, and W. Scandale, "Operational performance of crystal collimation with 6.37 Z TeV Pb ion beams at the LHC," *Phys. Rev. Accel. Beams*, vol. 27, p. 011002, Jan 2024.

[141] M. Garattini, D. Annucci, P. Gianotti, A. Liedl, E. Long, M. Mancini, T. Napolitano, M. Raggi, and P. Valente, "Steering of sub-gev positrons by ultrathin bent silicon crystal for ultraslow extraction applications," *Phys. Rev. Accel. Beams*, vol. 28, p. 023501, Feb 2025.

List of Figures

List of Tables

Eidesstattliche Versicherung

Hiermit versichere ich an Eides statt, die vorliegende Dissertationsschrift selbst verfasst und keine anderen als die angegebenen Hilfsmittel und Quellen benutzt zu haben. Sofern im Zuge der Erstellung der vorliegenden Dissertationsschrift generative Künstliche Intelligenz (gKI) basierte elektronische Hilfsmittel verwendet wurden, versichere ich, dass meine eigene Leistung im Vordergrund stand und dass eine vollständige Dokumentation aller verwendeten Hilfsmittel gemäß der Guten wissenschaftlichen Praxis vorliegt. Ich trage die Verantwortung für eventuell durch die gKI generierte fehlerhafte oder verzerrte Inhalte, fehlerhafte Referenzen, Verstöße gegen das Datenschutz- und Urheberrecht oder Plagiate.

Hamburg, den 03.04.2025 Unterschrift: 

Acknowledgement

I would like to express my deepest gratitude to Ilya for his outstanding supervision and leadership. He is an exceptional scholar and mentor, and I have learned immensely under his guidance. I am also grateful to the members of the PETRA IV beam physics group—Yong-Chul, Chao, Sergey, Rainer, and Joachim—as well as former member Lukas. Thank you for your valuable discussions and guidance throughout my PhD.

My sincere appreciation extends to Wolfgang for giving me the opportunity to be part of your extended team of PhD students. Your support, insightful conversations, and guidance have been truly invaluable.

I would like to thank Simon and Nicola for the interesting conversations and support during our experiments in Grenoble. Thanks again for hosting me and teaching me. A warm thanks goes to the colleagues at ESRF: Lee, Simone, Antonin, Kees, Friederike and Benoit.

A special thanks to my former office mates, François and Karel, for the engaging conversations and stimulating discussions. I will certainly miss them. I am also thankful to Klaus, Bianca, Sergey Tomin, Stuart, and Dmitri for the shared lunches and coffee breaks, which provided both intellectual exchange and much-needed moments of relaxation.

I would also like to extend my gratitude to Eike, Philipp, Rahul, Taylor, and Thomas for our fruitful collaboration and the many insightful discussions we had.

Finally, my deepest appreciation goes to my wife, Sofia, for her unwavering and unconditional support, as well as to my family—my mother Cristina, my father Hernán, and my brother Aarón. This journey has spanned ten years, and none of it would have been possible without you. I am equally grateful to my second family—Larisa, Vladimir, and Mark—whose kindness and support have meant the world to me.